Synthesis and characterization of novel cathode material with improved specific capacity and safety for lithium ion batteries

Dissertation

zur Erlangung des akademischen Grades

Doktoringenieur (Dr.-Ing.)

vorgelegt der
Fakultät für Elektrotechnik und Informationstechnik der
Technischen Universität Ilmenau

von

Frau M. Sc. Wassima El Mofid

geboren am 20.12.1987 in Marrakech/Marokko

vorgelegt am: 01.07.2016

Gutachter:

1. Univ.-Prof. Dr. rer. nat. habil. Dr. h. c. Andreas Bund
2. Univ.-Prof. Dr.-Ing. habil. Edda Rädlein
3. Prof. Dr. Ismael Saadoune

Verteidigung am: 19.09.2016

Verf.-Nr.: EI 393

urn:nbn:de:gbv:ilm1-2016000524

Abstract

The increasing requirements for high power and energy lithium ion batteries have led to the development of several classes of materials for the positive electrode. Some of those are the promising $LiNi_xMn_yCo_{1-x-y}O_2$ (NMC) materials.

In this context, the subject of this thesis is related to the extensive study of the electrochemical and structural properties of the pristine material NMC (3:1:1) ($LiNi_{0.6}Mn_{0.2}Co_{0.2}O_2$) and the three novel materials obtained either by mono-substitution of Co with Al or Fe: NMCA ($LiNi_{0.6}Mn_{0.2}Co_{0.15}Al_{0.05}O_2$) and NMCF ($LiNi_{0.6}Mn_{0.2}Co_{0.15}Fe_{0.05}O_2$) or by double substitution of Co with Al and Fe NMCAF ($LiNi_{0.6}Mn_{0.2}Co_{0.15}Al_{0.025}Fe_{0.025}O_2$).

As a first step, an optimization of the synthesis conditions was carried out using various methods (e.g. X-ray diffraction, scanning electron microscopy) in order to obtain homogeneous phases with well-ordered structures.
Structural, morphological and electrochemical properties of the four materials were then investigated. A more detailed study was devoted to NMCAF which showed better electrochemical properties compared to the pristine and the mono-substituted materials. The aim was to understand the phenomena behind the improvement of the electrochemical behavior of the double substituted material. The safety aspect of NMCAF was also discussed through a detailed study of the thermal stability during the lithium ion de-intercalation process.

Kurzzusammenfassung

Die steigenden Anforderungen an Lithium-Ionen-Batterien mit hoher spezifischer Leistung und Energie haben zur Entwicklung von mehreren Klassen von Materialien für die positive Elektrode geführt. Darunter sind unter anderem die vielversprechenden $LiNi_xMn_yCo_{1-x-y}O_2$ (NMC) Materialien.

In diesem Zusammenhang ist das Thema dieser Arbeit eine umfangreichen Studie der elektrochemischen und strukturellen Eigenschaften des ursprünglichen Materials NMC (3:1:1) ($LiNi_{0.6}Mn_{0.2}Co_{0.2}O_2$) und der drei neuen Materialien, die entweder durch Mono-Substitution von Co mit Al oder Fe: NMCA ($LiNi_{0.6}Mn_{0.2}Co_{0.15}Al_{0.05}O_2$) und NMCF ($LiNi_{0.6}Mn_{0.2}Co_{0.15}Fe_{0.05}O_2$) oder durch doppelte Substitution von Co mit Al und Fe NMCAF ($LiNi_{0.6}Mn_{0.2}Co_{0.15}Al_{0.025}\ Fe_{0.025}O_2$) hergestellt wurden.

Im ersten Schritt wurde eine Optimierung der Synthesebedingungen durchgeführt. Dazu wurden verschiedene Verfahren (z.B. Röntgenbeugung, Rasterelektronenmikroskopie) verwendet, um homogene Phasen mit gut geordneter Struktur zu erhalten.

Im zweiten Schritt wurden Struktur, morphologische und elektrochemische Eigenschaften der vier Materialien untersucht. Eine detailliertere Untersuchung wurde NMCAF gewidmet. Dieses Material zeigte die besten elektrochemischen Eigenschaften im Vergleich zu den ursprünglichen und den mono-substituierten Materialien. Ziel ist eszu verstehen, was die Mechanismen hinter der Verbesserung des elektrochemischen Verhaltens des doppelsubstituierten Materials sind.

Schließlich wurde der Sicherheitsaspekt von NMCAF auf Basis einer detaillierten Untersuchung der thermischen Stabilität während der Lithium-Ionen-Deinterkalation diskutiert.

Contents

Preface

At this prominent position, I have the pleasure to thank all the people who contributed to the achievement of this thesis.

First of all, it is my pleasure to express my highly gratitude and appreciation to Prof. Andreas Bund who gave me the opportunity to pursue my PhD in his group. I appreciated during the period of my PhD his broad skills, critical thinking and wise advice. I am equally thankful to his guidance in my research work, his continuous support, his availability, and generosity. Additionally, I am indebted to him for giving me the opportunity to participate in several highly ranked national and international conferences.

At the same time, I would like to thank Prof. Edda Rädlein and Prof. Ismael Saadoune for accepting to review my PhD thesis and be members of the thesis commission. I am likewise thankful to Prof. Peter Schaaf to accept being the chair of my defense.

Additionally, I am very grateful to Dr. Svetlozar Ivanov for his appreciable help and support, for his enthusiasm and friendly advice and for his valuable and critical comments. I am also grateful for our scientific discussions.

This thesis would not be achieved without supports by many persons. I would like to thank:

- Dr. Adriana Ispas for her help with the SEM measurements and for our interesting discussions,
- Dr. Alexander Konkin for the EPR measurements,
- Dr. Rolf Grieseler for his assistance and help with SEM and XRD measurements,
- Dr. Yong Yan and Diana Roßberg for their help with the thermal treatment of my samples,
- Dr. Dagmar Raab for her help with DTA-TG measurements and for her kindness,
- Dr. Bernd Halbedel for his assistance with ball milling process,
- Dr. Kerstin Pfeifer for her help especially with the preparation of my samples for SEM.

Special thanks are addressed to Prof. Sreedevi Upadhyayula and her working group from the Indian Institute of Technology in New Delhi who gladly accepted to welcome me for one month and to perform meanwhile BET and FTIR measurements.

Also, I would like to thank Prof. Lee Jong Min from Nanyang Technological University in Singapore and his PhD students Anjali Jayakumar and Tim Huang for the Raman measurements and for their pleasant and friendly welcome in NTU Singapore.

Further thanks go to all my colleagues from the ECG group: Dr. Udo Schmidt, Dr. Cornel Constantin Lalau, Dr. Violeta Tincuta Gruia, Dr. Codruta Aurelia Vlaic, Dr .Ralf Peipmann, Magali Camargo Leon, Sri Mulyaningsih, Sanaz Khajeh Hesamedini, Marianne Lerp, Mathias Fritz, Michael Stich, Denny Schmidt, Mario Kurniawan, Martin Leimbach, Florina Cuibus …

who accompanied me on my journey. I will not forget our lively discussions, our celebrations and trips.

I would like to express my gratitude to Frau Karin Keller and Frau Anneliese Täglich who assisted me in the lab.

Many thanks to our secretaries Maren Lange, Gaby Böhme, Susan Mämpel who helped me all the time with all the administration issues.

The financial support by Thüringen Landesgratuiertenförderung, by Li-Tec Battery GmbH, by LiMTech Helmholtz Alliance, by the DFG funded program WeNDeLIB, by Gleichstellungsrat der TU Ilmenau and by AGEF e.V. is gratefully acknowledged.

Last but not least, I am extremely grateful to my parents El Batoul Lokrifa and Abdeljalil El Mofid who raised me with unquestioned love. (Maman et Papa je vous aime énormèment et je ne parviendrai jamais à vous remercier suffisamment).

Great thanks go to my husband Mohamed Bichra who was my pillar of strength during the last five years. Thank you for your great help, support and affection. I will never be able to express my deep gratitude to him.

Thanks to my sisters, brother and all my family and family in law.

Nomenclature

1. Abbreviations

BET	Brunauer Emmett and Teller
CV	Cyclic voltammetry
DMC	Dimethyl carbonate
DTA-TG	Differential thermal analysis coupled with thermogravimetry
EC	Ethylene carbonate
EDX	Energy dispersive X-ray
EIS	Electrochemical impedance spectroscopy
EMC	Ethyl methyl carbonate
EPR	Electron paramagnetic resonance
EV	Electric Vehicle
FWHM	Full width at half maximum
GC	Galvanostatic cycling
GITT	Galvanostatic intermittent titration technique
HEV	Hybrid Electric Vehicle
hfs	Hyperfine structure
IL	Ionic liquid
LIB	Lithium ion battery
NMC	$LiNi_xMn_yCo_{1-x-y}O_2$
NMC (1:1:1)	$LiNi_{1/3}Mn_{1/3}Co_{1/3}O_2$
NMC (3:1:1)	$LiNi_{0.6}Mn_{0.2}Co_{0.2}O_2$
NMCA	$LiNi_{0.6}Mn_{0.2}Co_{0.15}Al_{0.05}O_2$
NMCAF	$LiNi_{0.6}Mn_{0.2}Co_{0.15}Al_{0.025}Fe_{0.025}O_2$
NMCF	$LiNi_{0.6}Mn_{0.2}Co_{0.15}Fe_{0.05}O_2$
NMP	N-methyl-2 pyrrolidone
PC	Propylene carbonate
PE	Polyethylene
PEO	Poly(ethylene oxide)

PHEV	Plug-in Hybrid Electric Vehicle
PMC	Propyl methyl carbonate
PP	Polypropylene
PVDF	Poly(vinylidenefluoride)
$PYR_{1R}TFSI$	N-alkyl-N-methylpyrrolidinium bis(trifluoromethanesulfonyl)imide
SEI	Solid Electrolyte Interphase
SEM	Scanning electron microscopy
SG	Space group
SHE	Standard hydrogen electrode
VC	Vinylene carbonate
XRD	X-ray diffraction

2. Symbols

A	Area
B_{iso}	Isotropic atomic displacement parameter
C	Concentration
C_{dl}	Double-layer capacitance
C/n	Cycling rate
dt	Duration of current flow in the cell
D_{Li+}	Lithium diffusion coefficient
E_{OCP}	Cell potential at open circuit
F	Faraday constant (96485 C/mol)
H	Linewidth
I	Current
I_c	Current contribution from the surface pseudo-capacitive effect
I_d	Current contribution from the bulk lithium insertion process
I_p	Peak discharge current
M	Molar mass of the active material
m	Active mass
n	Number of electrons per molecule
P	Power
Q	Capacity
R	Gas constant 8.314 $J\,K^{-1}\,mol^{-1}$
r	Ionic radius
R_B	Bragg factor
R_{ct}	Charge transfer resistance
R_e	Electrolyte resistance
R_{wp}	Weighted profile factor
R-3m	Rhombus-like unit cell with one mirror plane and triple rotary reflections
T	Absolute temperature
Tc	Curie point
U, V and W	Caglioti coefficients

V_M	Molar volume
W	Energy
x	Lithium composition
Z_w	Warburg impedance
Δx	Number of electrons inserted per mole of active material
η	Form factor
σ	Warburg factor
τ	Pulse duration
ν	Scan rate

List of figures

List of tables

I. Introduction and motivation

Nowadays, given the extreme dependence on portable electronic devices as well as the increasing demand for electric cars, the development of new rechargeable energy storage systems has become increasingly important.

Over the last decades, different electrochemical energy storage systems have been developed ranging from primary systems to rechargeable cells that have finally allowed a greater autonomy at reduced mass and volume.
Among all the rechargeable systems, lithium ion batteries show higher energy density, stability and improved lifetime compared to lead acid, Ni-Cd and Ni-MH accumulators [1-4].

In the early 1970s, M. Stanley Whittingham suggested the first rechargeable batteries consisting of titanium disulfide as positive electrode and metallic lithium as negative electrode [5,6]. However, problems related to changes at the lithium electrode during cycling due to the consumption of the lithium as well as the formation of dendrites lead to severe safety issues. Thus, came the idea of developing lithium intercalation materials for both negative and positive electrodes. In 1980, Rachid Yazami was the first to discover the graphite-based lithium reversible intercalation material. This discovery has led to the lithium-graphite anode used so far in the commercial lithium-ion batteries [7].
The first lithium ion battery using the positive electrode material $LiCoO_2$ and the graphite based negative electrode was commercialized by Sony in 1991 [8] exhibiting operating voltages of up to 4 volts and fairly large energy density and specific energy values of the order of 200-300Wh/L and 100-130Wh/kg respectively [9].
This new rechargeable battery was at that time a turning point and a key factor for the development of portable electronic devices. Since then, active research has been conducted in a way to improve the performance of each battery component [9].

$LiCoO_2$ as the positive electrode material was for a long time widely used [10-12] due to its high capacity and good cycling stability even at high rates [13]. However, the toxicity and the high costs of cobalt are considered disadvantages of this positive electrode material. Therefore, other lithium-containing transition metal oxides have been proposed to replace $LiCoO_2$ such as spinel phase $LiMn_2O_4$, layered oxides $LiNiO_2$, mixed layered oxides $Li\ (Ni_xMn_yCo_{1-x-y})\ O_2$ called NMC and olivine phase $LiFePO_4$.

Among these materials, $LiNiO_2$ seemed first to present good potential to replace $LiCoO_2$ due to its lower cost and its great discharge capacity. However, studies on this lamellar oxide suggested an excess of Ni in the structure, more precisely in the interlayer space. This disorder results in a capacity fade and a decrease of the lithium diffusion coefficient [14].

For cost reasons as well as improved toxicity and thermal stability issues compared to nickel and cobalt oxides [15], the $LiMn_2O_4$ spinel phase was also considered as a good candidate to replace $LiCoO_2$. However, the disproportionation reaction of Mn induces a rapid capacity loss. On the other hand, the structural instability of the compound in the intercalated state [16] limits the use of this system especially for electric and hybrid vehicles applications.

Among the most studied compounds of the olivine group, $LiFePO_4$ proves to be an attractive one given its low cost, low toxicity and especially its high thermal stability in the charged state even better than those obtained for the $LiNiO_2$, $LiCoO_2$ and $LiMn_2O_4$ cathode materials. [17].

However, due to its low electronic and ionic conductivities [18], it was necessary to conduct more studies on $LiFePO_4$ compound [19-22].
An established approach to obtain novel materials with improved reversible capacity and cycling stability, lower cost, less toxicity and better thermal stability is to combine the advantages of the three materials $LiNiO_2$, $LiCoO_2$ and $LiMn_2O_4$ and at the same time limit their drawbacks. This class of positive electrode materials called ($LiNi_xMn_yCo_{1-x-y}O_2$ NMC type materials) is currently in the focus of research [23-35].

Since Ohzuku's early work on $Li[Ni_{1/3}Co_{1/3}Mn_{1/3}]O_2$ in 2001 [34] several studies have been conducted on NMC type materials. Contrary to $LiCoO_2$, NMC shows a flexible stoichiometry which allows an adjustment of the electrochemical properties of the material.

The most widely researched NMC composition $LiNi_{1/3}Mn_{1/3}Co_{1/3}O_2$ was seen as one of the most promising materials in this class [34]. However, more compositions exist, among which some have not been extensively investigated, including $LiNi_{0.6}Mn_{0.2}Co_{0.2}O_2$ that is currently in our focus. There has been interest in studying this composition because it represents a compromise between the good electrochemical performance due to the presence of a high amount of nickel, the increased thermal stability induced by manganese ions Mn^{4+} and the minimization of the cost and toxicity by decreasing the cobalt content.
Nevertheless, it has been shown in a considerable number of studies that the exchange between Li and Ni ions within the NMC lattice plays a negative role for the structural stability and further deteriorates the electrochemical performance of layered oxides [36]. The physical reason for this phenomenon is related to similarity between the ionic radii of Li^+ and Ni^{2+}. The ionic radius of Li^+ (0.76 Å) is close to that of Ni^{2+} (0.69 Å), hence a partial occupation of Ni^{2+} sites by Li^+ (by exchange between a Li^+ and a nearest neighbor Ni^{2+}) induces a cation mixing in the structure, which hinders the efficient Li ion transport in the solid state [36]. Taking into account this problem, cationic substitution to a transition metal is considered, as for $LiNiO_2$ and $LiMn_2O_4$ [37-57], a promising approach for the cathode materials of NMC type. Such an approach has been an effective strategy to adjust the electrochemical performance or the structural/thermal stability of the material due to the decrease of the cation mixing between Li and Ni ions in the NMC lattice. The changes in the cationic distribution within these transition metal oxides can have a noticeable impact on the reversible capacities and on lithium diffusion during the intercalation/deintercalation process.

Many scientists worldwide have reported important theoretical studies on substituted NMC-type materials to Al, Mg, Cr, Fe, Be, Ga etc. [58-64]. This idea has been applied in the current study through cationic substitution of Co with Al and/or Fe. This idea was investigated for several reasons. First, a simultaneous double substitution has led to a novel composition that has not been studied so far. Second, earlier studies about cationic substitution for other systems have been conducted and showed that metal substitution in layered materials generally brings an improved performance for a number of cathode compositions, but the effect of simultaneous cationic substitution has not been extensively approached. Third, the pristine cathode material $LiNi_{0.6}Mn_{0.2}Co_{0.2}O_2$, which already exhibits good electrochemical behavior, will be used as a promising compound for further substitution. For this, the main motivation in this thesis arises from the will to achieve a lower cost and environmentally benign, less cobalt containing structure while retaining a high safety and electrochemical performance.

The present work is divided into six chapters:

First a bibliographical recall on lithium ion batteries including their components as well as their operating principle will be presented in chapter 2 followed by the different experimental techniques used to characterize the materials studied throughout this work (chapter 3).

Chapter 4 concerns studies performed to optimize the synthesis conditions such as synthesis method, annealing temperatures, synthesis atmosphere etc ... This enabled the preparation of phases with well-ordered structures exhibiting improved electrochemical performance.

The 5th chapter is devoted to structural, morphological and electrochemical properties of four materials: the pristine material NMC (3:1:1), two aluminum or iron mono-substituted materials NMCA ($LiNi_{0.6}Mn_{0.2}Co_{0.15}Al_{0.05}O_2$), NMCF ($LiNi_{0.6}Mn_{0.2}Co_{0.15}Fe_{0.05}O_2$) respectively, and the double substituted material NMCAF ($LiNi_{0.6}Mn_{0.2}Co_{0.15}Al_{0.025}Fe_{0.025}O_2$).

Finally, a more detailed comparison between NMC and NMCAF which presented the best properties will be compiled in the 6th chapter in such a way that a better understanding of the phenomena behind the improvement of the electrochemical behavior of the double substituted cathode can be achieved. That chapter also discusses the safety aspect of the two materials through a detailed study of their thermal stability during the lithium ion de-intercalation process.

II. State of the art

1. Industry of lithium ion batteries

Lithium-ion batteries are power batteries used for energy storage in numerous electronic devices available on the market such as mobile phones, cameras and many others. Moreover, the demand for this kind of batteries in the automotive industry is expected to increase due to the growing demand for battery electric vehicles. The reason behind this constantly growing demand comes from the fact that they are capable of storing a significant amount of energy for relatively small volume and weight, in addition to the ongoing improvement of many of their technology aspects such as the cycling stability, energy density, safety, costs, and more.

Then, in order to cover this huge demand of energy storage, it was crucial to take full advantage of lithium mines worldwide. Overall distinguished reserves of lithium in 2008 were evaluated by the US Geological Survey as 13 million tons [65]. However it is amazingly hard to precisely assess the world's lithium reserves [66].

Figure 1 represents the nations with the biggest mine production of lithium worldwide between 2010 and 2014. The top 3 producers according to the statistic are Australia, Chile and China respectively. However, Chile´s lithium mine production reached the highest amount in 2012, about 13200 metric tons coming then at the lead position.

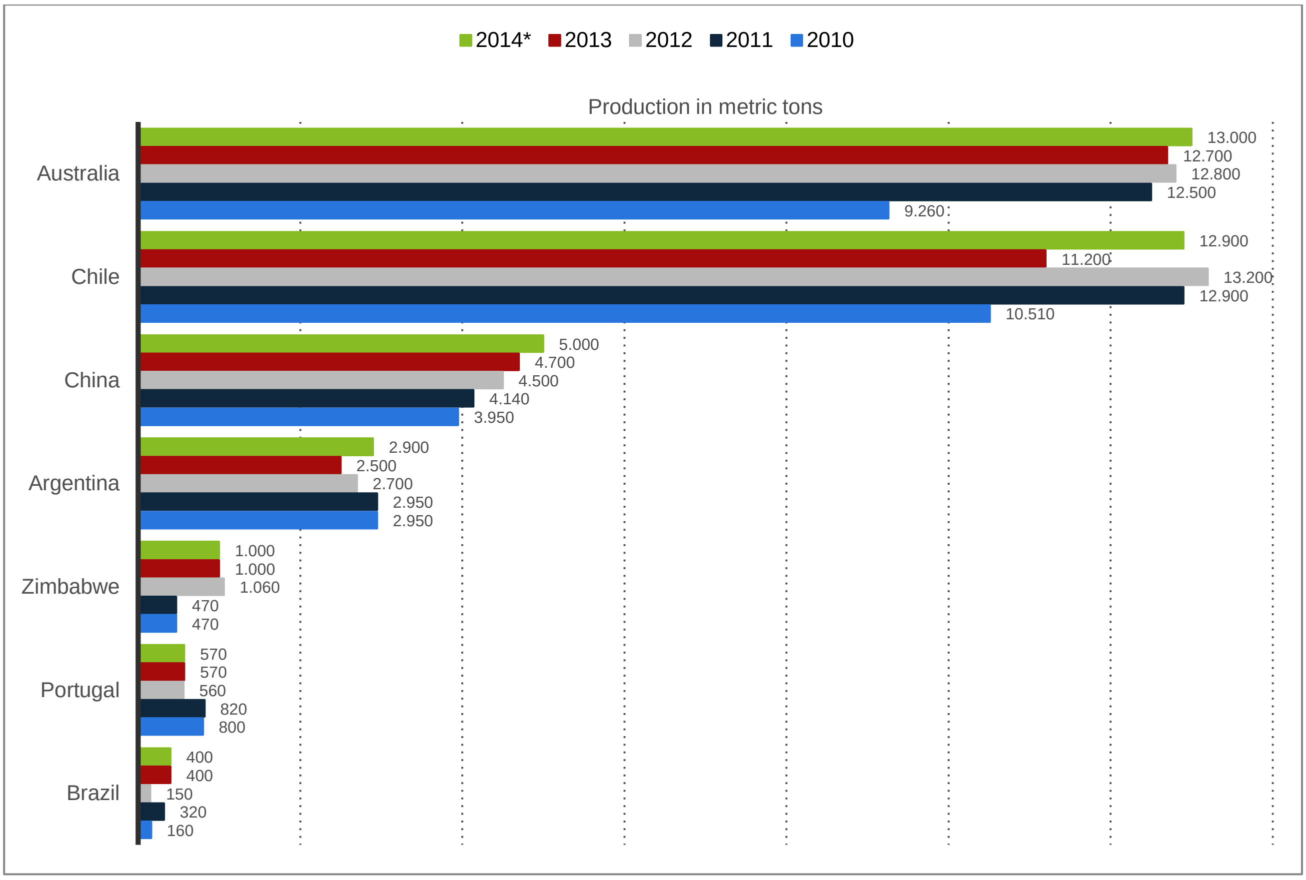

Fig. 1: Major countries lithium mine production between 2010 and 2014 (in metric tons) [67]

The Chilean company SQM considered as one of the largest lithium producers in the world estimates that global demand for lithium has increased with an average of 7 to 8% per year during the last decade. About half of this growth was due to the increase in demand for lithium traditional uses in the fabrication of manufactured products and the other half would be attributable to manufacturing batteries, including lithium-ion battery used in cell phones and laptops [68]. The overall consumption of lithium used in the battery manufacturing has increased more than 20% annually over the past years as the demand for lithium-ion and lithium polymer batteries is growing strongly. Other lithium uses are also increasing but at a lower rate [68].

From the production side, China, Japan and South Korea account for nearly 85% to 90% of the global production worldwide among the major market players (figure 2). The Japanese giants Panasonic and AESC (Automotive Energy Supply Corporation) are the leaders. In addition to the Korean Samsung SDI and LG Chem, all are considered the major manufacturers of lithium-ion batteries worldwide. On the other hand, China has the highest concentration, with over 200 producers [69]. In Europe, the German company Li-Tec Battery GmbH which is a wholly owned Daimler subsidiary [70], contributed to a significant extent in the market in 2015 standing at around four percent. Until the end of 2015, the company developed, produced and sold under the brand name CERIO large-scale lithium-ion batteries for automotive applications and battery systems for industrial and stationary applications [71].

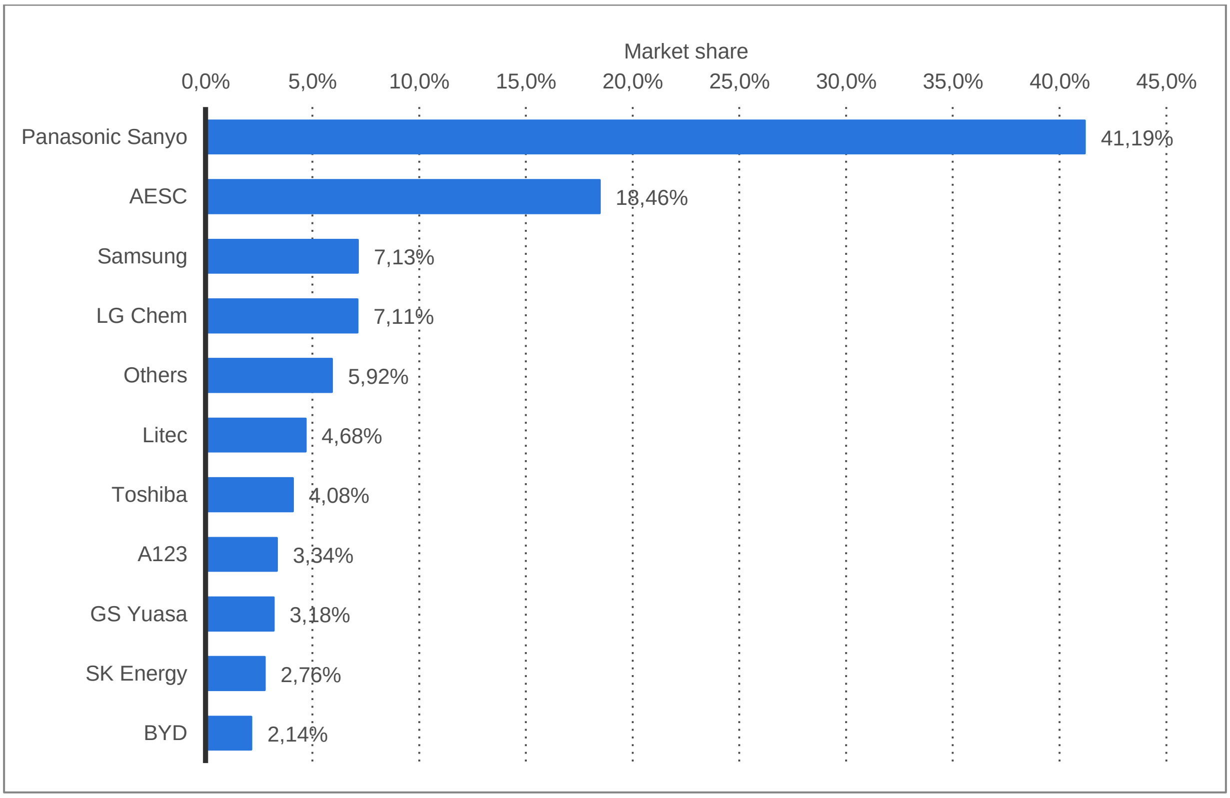

Fig. 2: Global market share of lithium battery makers in 2015 [72]

II. State of the art

Lithium-ion batteries have represented in 2011 a market of 1.5 billion dollars, which is expected to reach 9.8 billion dollars in 2015 and could even exceed 15.6 billion in 2020 (Fig. 3). The consumer electronics market is taking up the majority of this growth (Fig. 4).

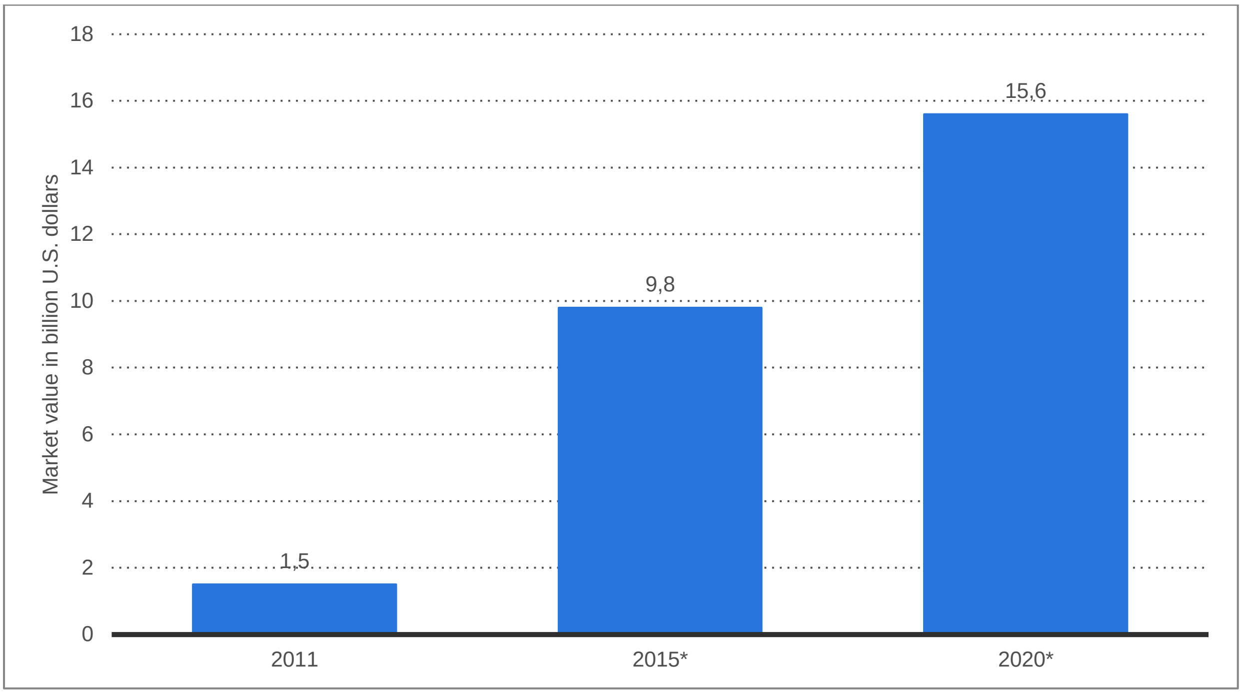

Fig. 3: Projected global lithium battery market size from 2011 to 2020 [73]

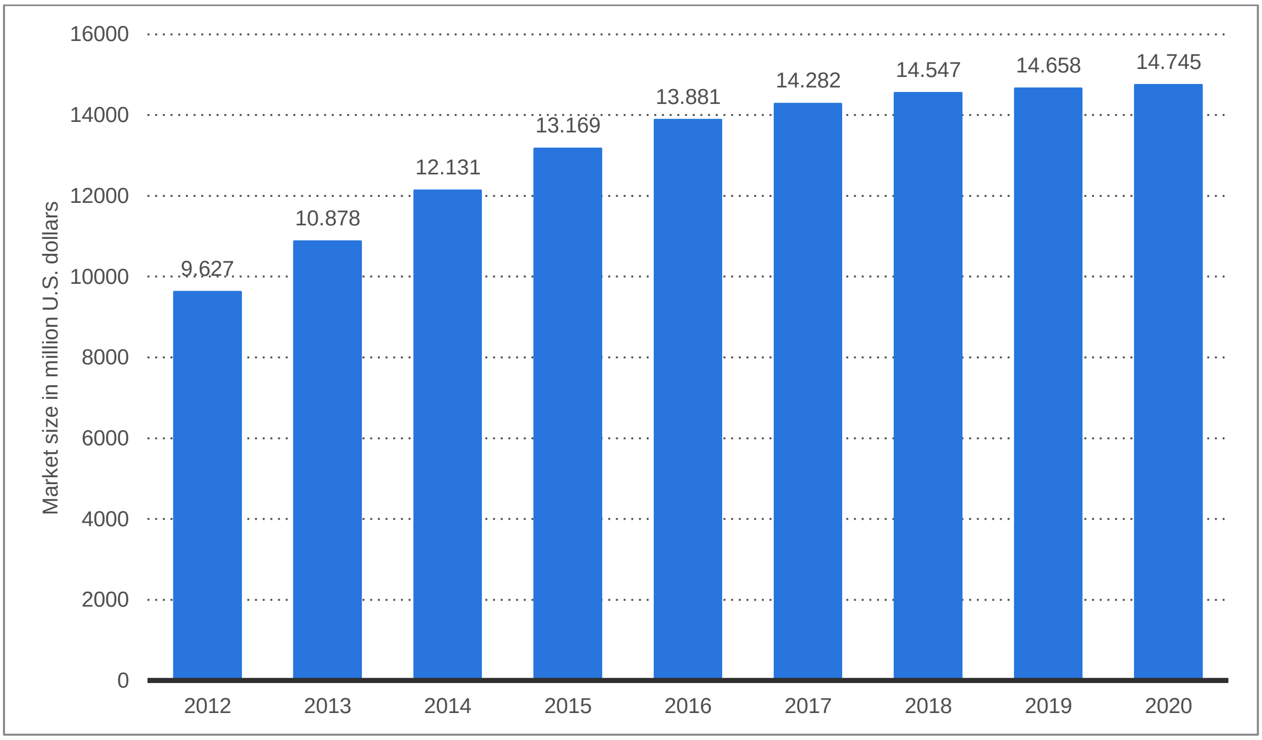

Fig. 4: Projected market for lithium-ion batteries used in consumer electronics from 2012 to 2020 (in million U.S. dollars) [74]

The statistic in figure 4 shows the consumer electronics lithium-ion battery business sector between 2012 and 2020. It was evaluated that this business sector will attain 13.2 million U.S. dollars by 2015. The utilization of lithium-ion batteries in consumer electronics, for example, cell phones, power tools and handsets is intended to expand as market for these products.

Li-ion battery market for mobile phones has a bigger piece of the overall consumer electronics industry. The predominance of this section is a result of the high infiltration of low cost smartphones in developing countries. The mobile phones fragment is trailed by the laptops due to the continually growing interest from the education sector. Therefore, numerous organizations are contributing intensely to improve the quality of education and learning. For example, Intel has put more than 1 billion US dollars in 70 nations in the last decade to change the traditional education framework. For this, laptop manufacturers are expected to present new and propelled features that enhance the transportability and accessibility of laptops [75].

Although lithium-based batteries are the most well-known propelled batteries for use in compact portable consumer electronics and battery electric vehicles, they were not the first choice for use in hybrid electric vehicles for quite a long while due to the high cost connected with this sort of battery contrasted with Ni-MH batteries. With the falling costs of lithium-based batteries after 2005, auto makers started to utilize lithium batteries in hybrid electric vehicles expanding the market size fundamentally [76]. The statistic in figure 5 shows the evaluated car lithium-ion battery business sector between 2012 and 2020. It was expected that this business sector will reach about 4.4 million U.S. dollars by 2015. The business sector is marked by electric vehicle production growth. On the vehicle production side, it is expected to produce about 4 million electric and hybrid vehicles per year. Light vehicles represent more than 85% of the total market for lithium-ion batteries in 2015 [77].

The projection of lithium-ion batteries costs for electric vehicles in 2012 and 2016, by vehicle type is presented in figure 6. The difference in costs between EVs (Electric Vehicles) and PHEVs (Plug-in Hybrid Electric Vehicles) is mostly because a PHEV uses both an IC (Internal Combustion) engine and an electric motor for propulsion. Thereby, the utilization of twofold fuel system makes PHEVs costly. In 2012, lithium-ion batteries costed about 814 U.S. dollars per kilowatt hour in PHEVs and about 633 U.S. dollars per kilowatt hour in EVs. The decrease in lithium-ion batteries costs will be intensely persuasive on the achievement of plug-in hybrid electric vehicles with lower costs. Furthermore, the diminishment in expenses of cobalt, metal, wiring, and plastic have brought down battery costs [78]. This can only be a fundamental and compelling reason for the battery market growth in both portable consumer electronics (fig. 4) and electric vehicles (fig. 5) sectors.

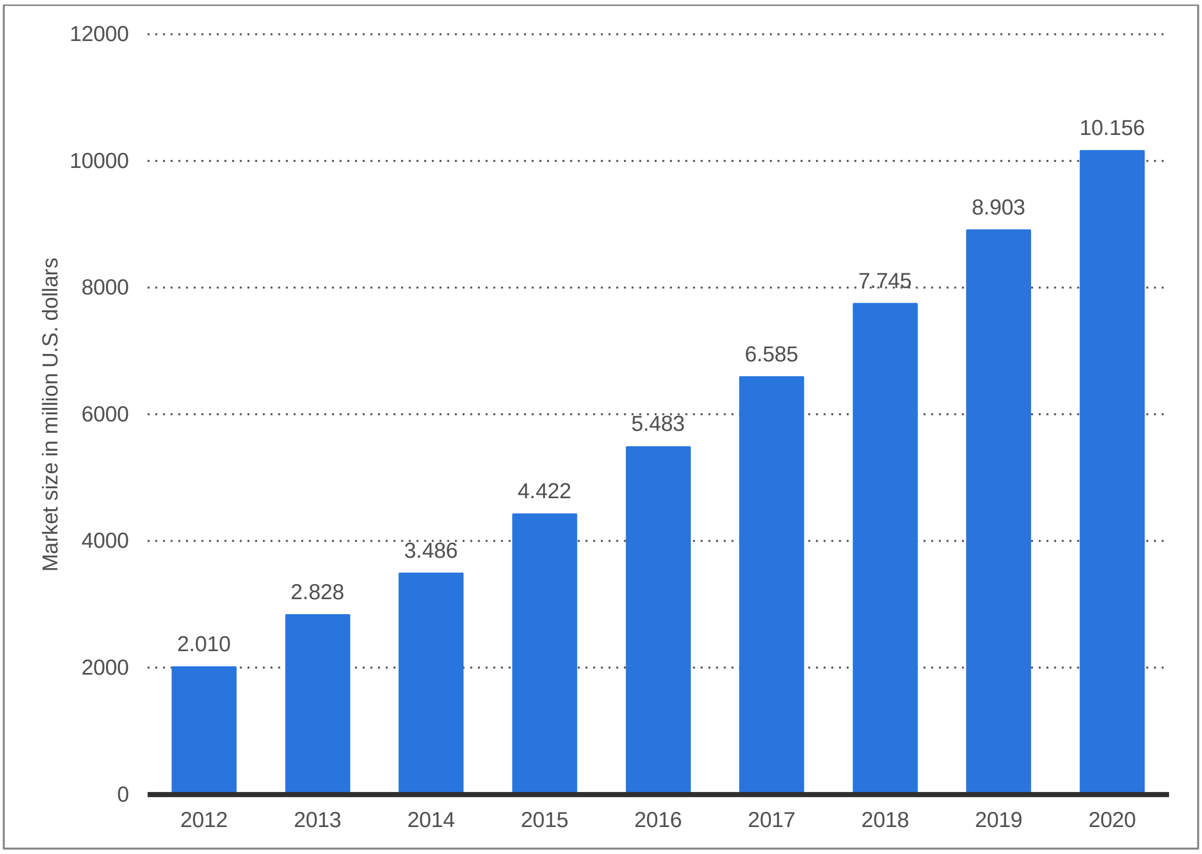

Fig. 5: Projected market for lithium-ion batteries used in automobiles from 2012 to 2020 (in million U.S. dollars) [79]

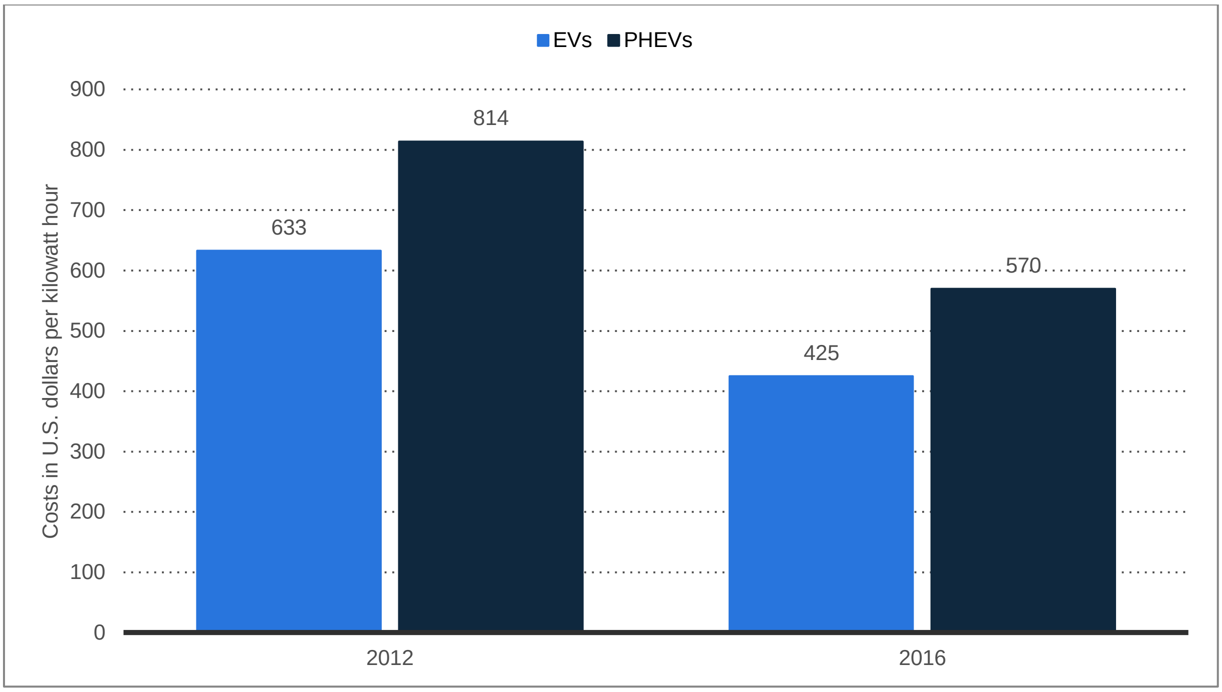

Fig. 6: Typical cost of lithium ion batteries for electric vehicles in 2012 and 2016, by vehicle type (in U.S. dollars per kilowatt hour) [80]

2. Lithium ion battery components

A lithium ion battery (LIB) consists of two electrodes, one positive (cathode) and one negative (anode) separated by an electrolyte impregnated in a separator. Both electrodes are connected to the external electric circuit through current collectors (Fig. 7). The term "battery" is itself reserved for systems consisting of several cells, connected in parallel or in series.

In this work, and as it is common, the term battery will be used to designate a cell.

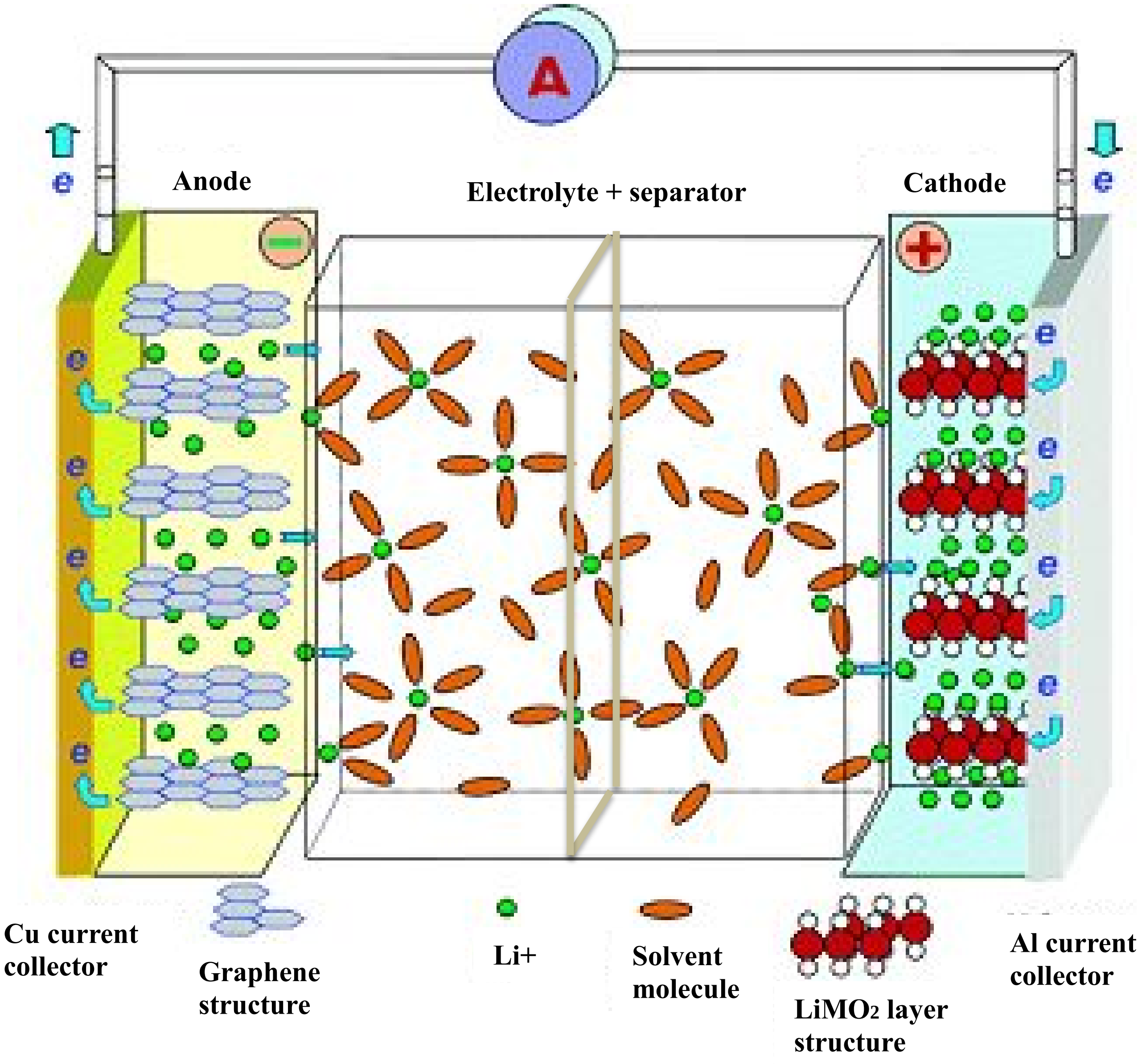

Fig. 7: Schematic representation of LIB components [81]

The first LIBs consisted of graphite and $LiCoO_2$ at the anode and cathode sides respectively. Their energy storage ability was more than double that of nickel or lead batteries for the same size and mass.

Nevertheless, the reversible intercalation of lithium ions is for the most part constrained by the modifications in the host material´s structure which influences the energy density. Thus, advancements will only be achieved by discovering through continuous advanced research novel electrode materials with improved performance in terms of cyclability, safety, energy density, power, price and environmental impact. Some of the cathode and anode materials that have been developed and tested since the establishment of the LIB technology more than 20 years ago are reported in table 1.

Table 1: Cathode and anode materials for lithium-ion batteries and their characteristics [82-84]

Type	**Chemistry**	**Specific Capacity in mAh/g (theoretical/ observed)**	**Potential vs. Li+/Li**	**Note**
Cathode	$LiCoO_2$	273/160	3.9	First cathode, expensive
	$LiNiO_2$	274/180	3.6	Cheaper than $LiCoO_2$, unstable
	$LiNi_xCo_yMn_zO_2$	~270/150–180	3.8	Cheap and stable
	$LiNi_xCo_yAl_zO_2$	~250/180	3.7	Stable
	$LiMn_2O_4$	148/130	4.1	Unstable cycling
	$LiMn_{1.5}Ni_{0.5}O_4$	146/130	4.7	High voltage, cheap
	$LiFePO_4$	170/160	3.45	Low voltage, safe, cheap, stable
	$LiMnPO_4$	171/80–150	4.1	Slow kinetics, cheap, high voltage
	$LiNiPO_4$	166/-	5.1	No suitable high voltage electrolyte
	$LiCoPO_4$	166/60–130	4.8	Expensive
Anode	Graphite	372/330	0.1–0.2	LiC_6, vol. change: ~11%
	$Li_4Ti_5O_{12}$	175/170	1.55	High voltage, no vol. change
	TiO_2 (anatase/rutile)	168/168	1.85	Cheap, vol. change: ~4%
	SnO_2	782/780	<0.5	Large initial irreversible loss
	Sn	993/990	<0.5	Poor cycling, vol. change: 257%
	Si	4198/<3500	0.5–1	Poor cycling, vol. change: 297%
	Al	2235	<0.3	Poor cycling, vol. change: 238%

II. State of the art

2.1. Negative electrode materials

This paragraph is committed to anode materials available on the market or being investigated in order to replace graphite, the most prominent material as commercial negative electrode. Candidates for the negative electrode material must meet the following criteria:

- Good chemical stability towards electrolytes to prevent degradation of the electrolyte or of the material during cycling. Such degradation phenomena are leading to side reactions that affect the electrochemical performance of the battery;
- High ionic and electronic conductivity;
- Large amount of inserted lithium in order to achieve a maximum specific capacity;
- Good electrochemical stability and reversibility of the insertion / extraction process.

Contrary to cathode materials, the composition of anode materials for LIBs is more various and might involve transition metals, post-transition metals as well as nonmetallic elements using different stoichiometries.

2.1.1. Metallic lithium

The electrochemical couple Li^+/Li has a low standard potential of -3.04 V vs. the standard hydrogen electrode (SHE). Another metallic lithium feature is its low molecular weight: 6.94 g mol^{-1} which allows a considerable gain in terms of mass, energy, power and specific capacity (theoretical capacity of lithium is 3200 $mAh.g^{-1}$).

Nevertheless, the use of lithium as the negative electrode material was abandoned especially for safety reasons such as the thermodynamic instability of lithium in most electrolytes. Yet, its corrosion is stopped by the formation of a passivation layer on the surface called SEI (Solid Electrolyte Interphase) especially in solvents containing a carbonate group. A conceivable arrangement is the utilization of a less reactive with the lithium electrolyte, to be specific, a solid polymer electrolyte. However, solid electrolytes have shown so far limitations in their use due to their low ionic conductivities and hindered ion transport.

Another safety issue that was highlighted is the formation of dendrites on the lithium electrode during cycling. The growth of these dendrites can cause their contact with the cathode leading to a short circuit of the battery which can induce explosion especially when unfavorable conditions related to the battery thermal stability are met. For all those reasons, the lifetime of the batteries using a lithium negative electrode is limited.

2.1.2. Graphite

To overcome the problems encountered in lithium metal batteries, replacing lithium by an insertion material is a standout amongst the most considered solutions. Carbonaceous materials have been proposed as negative electrode materials in the LIB commercialized by Sony in 1991 [85-88].

Among the numerous types of carbon electrodes, graphite is the most prevalent material due to its low cost, safety, better cycling stability and its Nernst potential close to that of lithium [89]. It is used to insert in the vacant space between its sheets a large amount of lithium (theoretical capacity 372 mAh.g^{-1}). The lithium storage mechanism into the carbonaceous material unequivocally relies on its morphology and structure. The intercalation of lithium ions into rhombohedral and hexagonal graphite takes place through the consecutive n-stages and the consequent expansion of the intersheet distance from 0.335 to 0.372 nm [90]. In the potential versus capacity plot, the staging phenomena are visible as plateaus.

Similar to what is observed on the lithium anode, the electrolyte is reduced at the carbon electrode at its operating potential (approximately 0.2 V versus Li^+/Li), resulting in the formation of a passivation layer (SEI). Part of the lithium electrolyte is then consumed permanently. This type of anode therefore has an irreversible capacity in the first cycle of the battery.

2.1.3. Transition metal oxides

Recently, various transition metal oxides of MO type (M = Co, Cu, Ni, Fe, etc.) have been investigated for use as a negative electrode [91,92]. These oxides are characterized by a very good cycling performance with specific capacities up to 600 mAh/g for tin oxide.

It has been found that tin oxide is a potential candidate for use as a negative electrode for LIBs. This material delivers reversible capacity in the order of 500-600 mAh / g at an average potential of 0.5 V vs. Li+/Li. The reaction of tin oxide with lithium takes place mainly in two stages: firstly, there is a reduction of tin to the metallic state Sn_0 and the formation of Li_2O. The second step concerns the formation of an alloy between lithium and tin Li_xSn. The Li_2O-forming reaction is irreversible and only the second process is reversible. The more tin nanoparticles are well distributed in the matrix of Li_2O, the more cycling stability of the electrode is improved.

At the following charging process, the metal nanoparticles are reoxidized, that step is accompanied by the decomposition of the Li_2O matrix. It is noteworthy that this new lithium storage mechanism is not limited to divalent oxides. Indeed, Co_3O_4 is a transition metal oxide storing lithium with the same cited mechanism. It has the highest specific capacity during the first discharge of about 1100 mAh g^{-1} vs Li^+/Li. [93]. Fe_2O_3 [94,95] and Cu_2O materials also exhibit high capacity values around 900 mAh g^{-1}.

2.1.4. Lithium alloys

A new family of negative electrodes based on the materials forming alloys with lithium is likewise used. Such anodes are the subject of numerous investigations.

Li alloys have several advantages as negative electrode such as being environmentally benign and presenting very high theoretical specific capacity values, up to 4200 mAh/g for silicon, much greater than that of graphite (372 mAh/g).

Many studies are also devoted to other alloys formed by lithium with elements such as aluminum [96], tin [97], or antimony [97] in addition to silicon [98]. They operate at potentials between 0.15 and 0.9 V vs. Li+/Li and deliver specific capacities between 300 and 4000 mAh/g. However, these compounds exhibit a very poor performance in cycling during discharge especially when at hight depths of discharge. The volume expansion undergone by this class of materials during the alloying reaction with lithium can vary according to the working conditions, between 97% [99] and 238% [100] in the case of LiAl and even 260% [101] and 358% [102] for $Li_{4,4}Sn$. Therefore, volume expansion is the major problem faced when using Li alloys as negative electrodes. It leads to high mechanical stress resulting in surface cracking and consequently a capacity fading after few cycles.

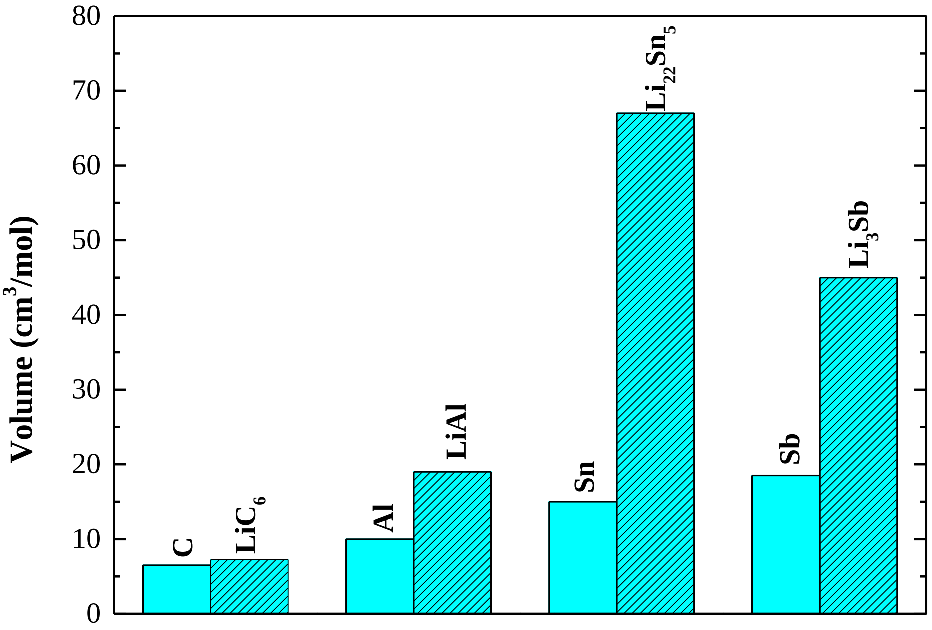

Fig. 8: Comparison of the volume expansion during Li insertion in graphite and metal matrices [103]

.

In order to increase the structural stability of these electrodes and thus to improve the cycling performance, two solutions have been proposed: first, the use of nanoparticles [104]. However, this strategy has not effectively led to the development of metallic materials that provide good electrochemical cyclability since the nanoparticles are able to aggregate, forming dense and inactive blocks after ten cycles [105, 106]. Another proposed method to reduce the volume expansion of the electrodes during the lithiation / delithiation is the use of an electrochemically inactive matrix, such as Sn_2Fe, $SnFe_3C$, SiNi [103] and Si / SnSb [107] with a stable capacity of about 700-1000 mAh/g.

2.1.5. Titanium intercalation oxides

Due mainly to their low manufacturing costs in addition to many more advantages, research on titanium mixed oxides ($Li_4Ti_5O_{12}$ [108] $Li_2Ti_3O_7$ [109] and $LiTi_2O_4$ [110], Table 2) as negative electrodes is experiencing considerable growth.

Table 2: Advantages and drawbacks of titanium intercalation oxides

Advantages	**Drawbacks**
- No hazard to the environment. - Higher operating potential than that of graphite (~ 1.5V vs Li^+/Li). This prevents the formation of passivation layers. - good cycling performance even at high charge/discharge currents used mainly for power applications - Low polarization due to the ease of lithium ions intercalation process especially in the 3D spinel structure. - No structural changes through cycling, making it a stable material with low mechanical stresses	- Weak theoretical specific capacities (175 [111] 200 [112] and 335 [113] mAh/g for $Li_4Ti_5O_{12}$, $Li_2Ti_3O_7$ and TiO_2 respectively) because of their higher molecular weights. - Low electronic conductivity [114].

Several researches have been done to improve the electrochemical performance of titanium based electrodes. Therefore, many approaches have been established such as nanostructuring of these materials or coating with a conductive material. This allowed obtaining materials with outstanding performance [115].

2.1.6. Tin based anode materials

It is known that the lithium-tin binary system forms seven different phases: Li_2Sn_5, LiSn, Li_7Sn_3, Li_5Sn_2, $Li_{13}Sn_5$, Li_7Sn_2 and $Li_{22}Sn_5$. It seemed difficult to achieve the latter composition $Li_{22}Sn_5$ [116, 117]. Courtney et al. (1998) [118] calculated the total energies of the lithium tin phase diagram using mathematical simulation studies by the ab initio method "pseudopotential plane-wave method". From these results, they assessed the theoretical electrochemical voltage profile, which showed an excellent agreement with the experimental curve. The successive appearance of new phases has been confirmed by the voltage reduction and the obtaining of several plateaus allocated to numerous lithiated phases Li_xSn.

Various intermetallic compounds based on tin have also been studied as alternatives to the commercial negative electrode for lithium-ion batteries such as $FeSn_2$ [119], Ni_3Sn_4, $CoSn_2$ [120] $CoSn_3$ [121], Cu_6Sn_5 [122], $CrSn_2$ [123] $LaSn_3$ [124]. In general, these compounds showed a long-term increase in cycling stability.

2.1.7. Nitrides and phosphides

The investigation of new anodic materials has likewise been extended to nitrides and phosphides. The lithium reaction mechanism for this material family is mainly based on lithium insertion and conversion.

2.1.7.1. Nitrides

Another relatively new scientific orientation is the study of mixed nitrides with lithium and other metals. Their electroactivity was demonstrated for the first time by Nishijima et al. with Li_3FeN_2 [125] and Li_7MnN_4 [126] in 1994. The specific capacities of these materials reached 150 and 250 mAh/g respectively.

Nishijima et al. [127] and Shodai et al. [128] have then put their focus on mixed lithium metal nitrides $Li_{3-x}M_xN$ type (M= Co, Cu, Ni). The most interesting material in terms of electrochemical performance is $Li_{2.6}Co_{0.4}N$. Indeed, the specific capacities delivered by this material are rather high ranging from 480 to 900 mAh/g [127,128]. When the metal used is copper or nickel, the specific capacities are lower (ca. 100 mAh/g) [128,129].

2.1.7.2. Phosphides

In numerous phosphides, the lithium intercalation causes an adjustment of P bonds and considerable structural changes.

Some of the transition metal phosphides are MnP_4 [130] CoP_3 [131] FeP_2 [132], Li_2CuP [133] and InP [134]. Their operating potential is around 0.7 V vs Li^+/Li. For Li_7TiP_4 and Li_9TiP_4 compounds, initial specific capacities are 971 mAh/g and 700 mAh/g respectively at C/20 rate [135].

Different mechanisms between lithium and phosphide have been established according to the studied phase.

2.1.8. Vanadium mixed oxides

Several studies have reported the good electrochemical behavior of mixed vanadium oxides. Vanadate compounds containing transition metals such as Li_xMVO_4 (M = Ni, Co, Zn, Cd) [136] and presenting different structures, can intercalate reversibly between 5.6 and 7.2 Li atoms per formula unit giving a specific capacity of 600 mAh/g for M = Ni or Zn. Likewise, MVO_4 (M = In, Cr, Al, Fe, Y), [137] $M_2V_2O_7$ (M = Co, Ni, Zn, Cd) [138] and $MV_2O_{6+\delta}$ (M = Mn, Fe or Co) [139] materials have the advantage of reacting with a large number of lithium ions at low potential, which provides good specific capacities. Some of the most promising candidates within mixed vanadium oxides family are $MnV_2O_{6,96}$, $InVO_4$, $FeVO_4$ and $LiNiVO_4$.

According to studies conducted on wide range of anode materials for LIB, a selection of promising materials could be envisaged. Among the most attractive materials, carbon is no doubt hard to be replaced.

Concerning promising materials that are close to a real application or already in prototype or used in recent commercial products, silicon is probably the most attractive.

2.2. Electrolytes

The role of the electrolyte in a lithium battery is to ensure lithium ion transport between the negative and the positive electrodes.

Some of the most important criteria to decide on the choice of any electrolyte are the safety, the cost and the environmental compatibility. Then, in order to improve the battery cycle life, the accurate formulation of the electrolyte is imperative [140].

Furthermore, the right candidate to be chosen as an electrolyte for a LIB must meet the following criteria:

- High ionic conductivity to ensure a good ionic transport, conversely no electronic conductivity to limit self-discharge,
- High chemical inertness towards the battery components and particularly the electrodes and separators,
- Wide electrochemical stability in the used potential range to avoid decomposition of the electrolyte during the battery use,
- Efficient passivation of the negative electrode surface
- Large thermal stability window allowing the use of the battery at various temperatures.

The electrochemical stability of the electrolyte is a key to its application in a lithium battery within a wide potential range since the negative electrode materials are strong reducing and those of the positive electrode are strong oxidizing agents.

In the case of a liquid electrolyte, SEI layer formation has been demonstrated in particular for metallic lithium [141] and carbon based compounds [142]. The activation energies at the graphite interface reflect the energies for the lithium ion desolvation from the solvent molecule (Fig. 9).

Once the SEI protective passivation layer formed, no further decomposition of the electrolyte is expected.

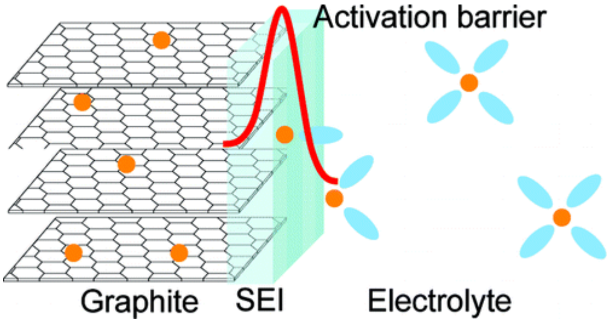

Fig. 9: Schematic illustration of the SEI layer on graphite [143]

Among the most used electrolytes in Li-ion batteries, can be cited organic solvent based liquid electrolytes, polymer electrolytes and ionic liquids.

2.2.1. Organic solvent based liquid electrolytes

Nowadays, in most of the commercial LIBs, organic solvent based liquid electrolytes are used. These are for the most part composed of a lithium salt dissolved in one or more organic solvents. The most utilized organic solvents are carbonates, for instance ethylene carbonate (EC), dimethyl carbonate (DMC), propylene carbonate (PC), ethylmethyl carbonate (EMC) and methyl propyl carbonate (PMC). The commonly used lithium salt is $LiPF_6$ since it offers advantages such as high conductivity in the organic solvents. Furthermore, $LiPF_6$ is able to form a passivating layer at the aluminum positive electrode current collector, which is considered an efficient way to avoid the aluminum corrosion. However, the thermal instability of $LiPF_6$ with delithiated layered transition metal oxides on the cathode side and lithiated graphite on the anode side in addition to the generation of hydrofluoric acid (HF) with water represent some of $LiPF_6$ drawbacks. Hence, as currently there is still no lithium salt which shows better performance, the utilization of $LiPF_6$ is a trade-off.

Alternative salts have been discussed such as $LiBF_4$, $LiAsF_6$ or $LiClO_4$. However, their explosivity, toxicity and low conductivity limit their use, which is why numerous studies have been carried out lately to find a good alternative to $LiPF_6$ [144]. Some of these are lithium cheloatophosphates,[145,146] lithium fluoroalkyl phosphates, [147-149] lithium chelatoborates,[150-152] and lithium salts based on heterocyclic anions such as imidazolates [153] and imidazolides [154].

One approach to enhance the performance of Li-ion battery systems, in terms of SEI layer formation, safety and flammability of the electrolyte systems, is the amendment of liquid electrolytes by using additives [155]. The most investigated is vinylene carbonate (VC) [156] [157-163], it has the advantages of reducing the irreversible capacity of graphite and improving the cycleability especially at high temperature [157,164,165].

The SEI formation mechanism for VC consists of an electrochemically induced polymerization process based on VC reduction on the graphite electrode forming then a polymeric layer (Fig. 10).

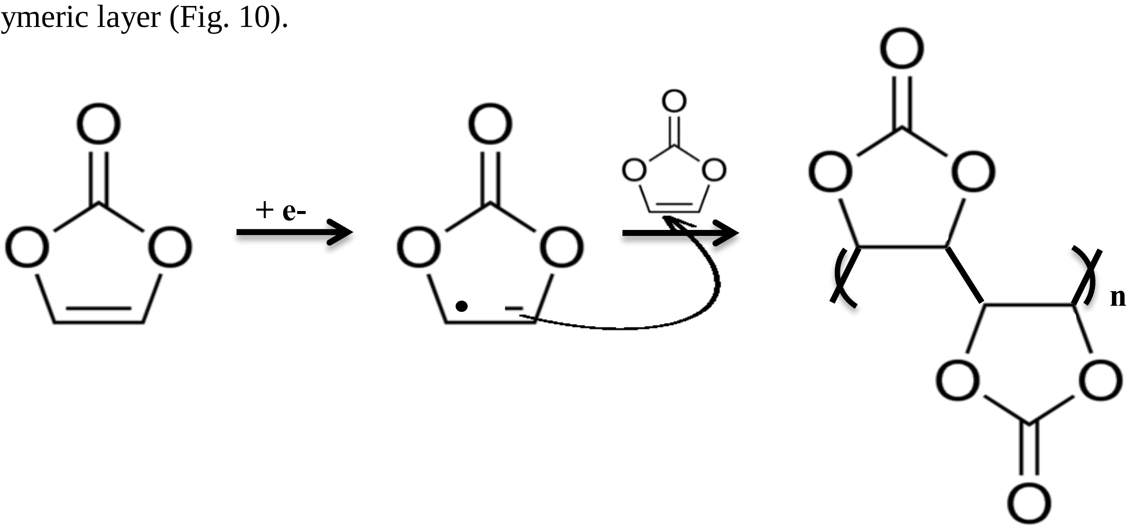

Fig. 10: Electrochemically induced polymerization of vinylene carbonate

2.2.2. Polymer electrolytes

Subsequent to the initiation of poly(ethylene oxide) (PEO)–LiX electrolytes in 1979, great efforts have been devoted to enhance the mechanical properties as well as the low ionic conductivity of polymer electrolytes. For practical applications the conductivity should be at least 10^{-3} S·cm^{-1}.
The development of polymer electrolytes took three directions: solid polymer electrolytes, gelled polymer electrolytes, and plasma polymer electrolytes.

- Solid polymer electrolytes like PEO-based systems consist of a polymer framework in which a lithium salt is dissolved and are used as a thin layer. However, the elevated degree of crystallinity of the formed PEO/salt complexes leads to a low conductivity at room temperature of the order of 10^{-4} S·cm^{-1} [166] caused by the limitation of ion mobility.

- Gelled polymer electrolytes are composed of a solid polymer matrix that traps the conductive organic solvent based liquid electrolyte. They have both the characteristics of solids (cohesive properties) and liquids (diffusion properties) [167]. The most frequently used solid polymer matrices are poly(vinylidenefluoride) (PVDF) [168,169] and copolymerized PVDF with hexafluoropropylene (HFP) [170-176] in order to decrease the polymer crystallinity. For further reduction of the crystallinity and stabilization of the lithium interfacial properties, nano-sized fillers like $BaTiO_3$ [170], Al_2O_3 [169,170], SiO_2 [169,170,172] and TiO_2 [171,173] might be added. Likewise, polymer blends consisting of PVDF or PVDF-HFP and a second polymer have been researched [177-179]. The conductivities of these systems vary between 0.98 and 4.36 mS·cm^{-1} at 20°C [180],

- The plasma polymer electrolytes were studied primarily by Ogumi et al. [181]. These polymers are often synthesized from a mixture of organosilicon compounds and lithium salts using plasma polymerization technique. An ionic conductivity of 10^{-6} - 10^{-5} S cm^{-1} is obtained for the polymer 2- [2- (2-ethoxyethoxy) ethoxy] ethoxydimethylvinylsilane (EDVS) -$LiCF_3SO_3$ at room temperature [181].

2.2.3. Ionic liquids

Noteworthy interest has been shown in terms of using ionic liquids (ILs) as substitutes for the organic solvents utilized as LIB electrolytes. ILs have promising features including high conductivity, very low volatility, negligible flammability and outstanding electrochemical stability. ILs are salts or salts mixtures that are liquid at room temperature [182-184]. They consist mainly from an organic or inorganic anion and an organic cation (Fig. 11). Accordingly, IL based electrolytes are obtained by mixing an IL with the suitable lithium salt (LiX). The most broadly utilized IL electrolytes for LIBs are those based on N-alkyl-N-methylpyrrolidinium bis(trifluoromethanesulfonyl)imide ($PYR_{1R}TFSI$) salts [185].

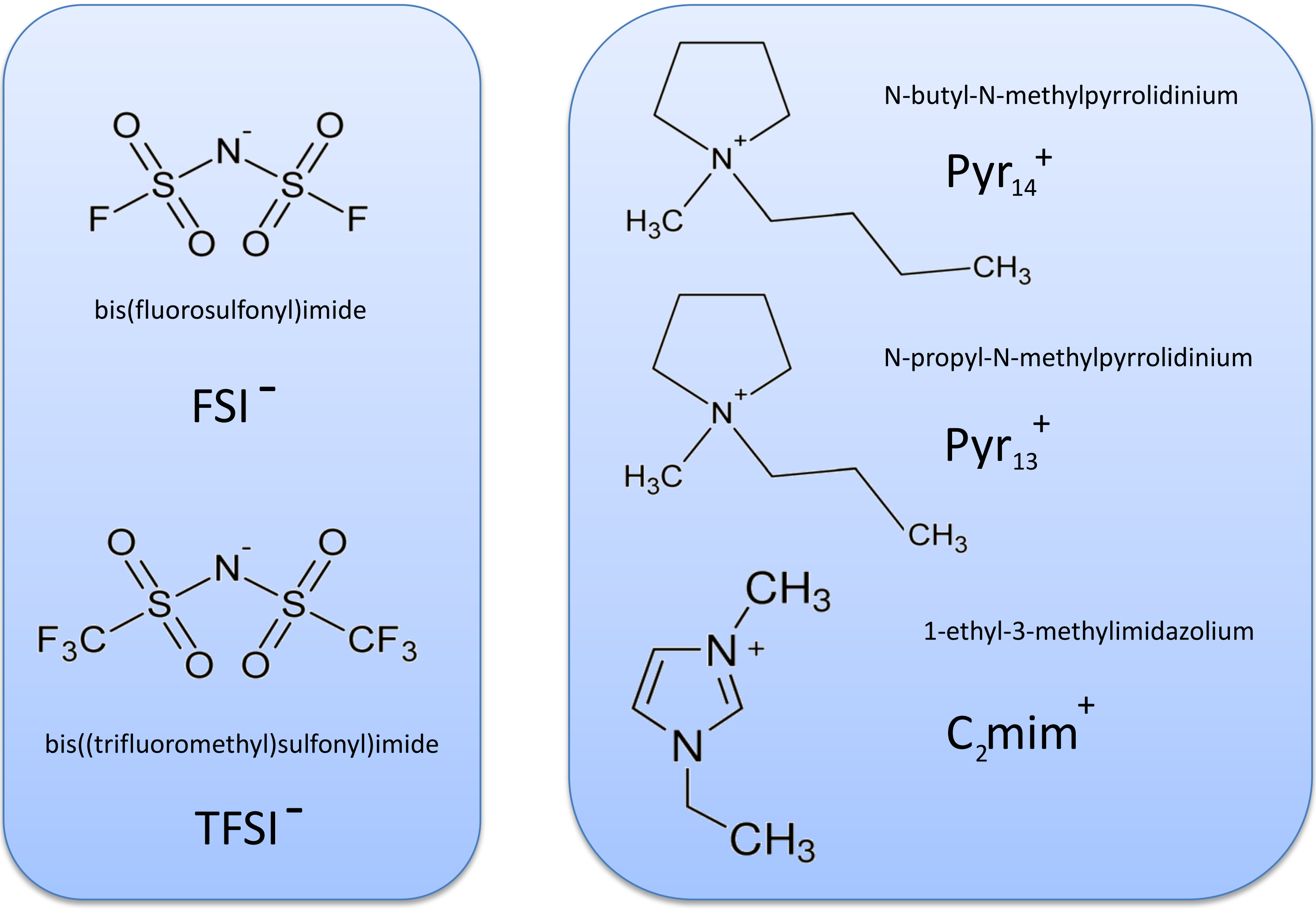

Fig. 11: Ions typically used for LIB ionic liquid electrolytes

.

Zheng et al. [186] investigated the electrochemical temperature reliance of $LiCoO_2$ with a quaternary ammonium IL–LiTFSI electrolyte (with $N_{1116}TFSI$).
Cyclic voltammetry was used to study the Li^+ extraction/insertion from the $LiCoO_2$ cathode. The poor electrochemical performance was credited to the high viscosity and low wettability of the electrolyte with the active material at room temperature, which resulted in a considerable hysteresis for the Li^+ extraction/insertion process

2.3. Separators

Separators are porous membranes set between positive and negative electrodes to allow the ionic flux between the electrodes while being good electronic insulators [187,189].
Very little consideration has been given to separators even in publications surveying batteries [187-195]. The number of reviews on separators [196-206] is small in comparison with those on electrodes and electrolytes.

2.3.1. Separators and batteries

Numerous properties are required for the separators utilized as a part of LIB. Some of the considerations that are imperative and impact the selection of the separator are the following:

- Negligible electrolyte (ionic) resistance
- Good electronic insulation
- Considerable dimensional stability
- Adequate mechanical strength to permit easy manipulation
- Chemical resistance to degradation
- Efficiency in hindering particle migration between the electrodes
- Good wettability by electrolyte
- Uniformity in properties, for instance thickness, resistance, etc...

The typical properties such as thickness, Gurley number (air permeability), ionic resistivity, porosity and melt temperature of some commercial separators are reported in Table 3. Celgard 2730 (used in the framework of this PhD work) and Celgard 2400 are respectively PE and PP single layer separators, while Celgard 2320 is a trilayer separator with a thickness of 20 µm.

Table 3: Typical properties of some commercial separators [207]

Separator/ Properties	**Celgard 2730**	**Celgard 2400**	**Celgard 2320**
Structure	Single layer	Single layer	Trilayer
Composition	PE	PP	PP/PE/PP
Thickness (µm)	20	25	20
Gurley (s)	22	24	20
Ionic resistivity (Ω.cm) [a]	2.23	2.55	1.36
Porosity (%)	43	40	46
Melt temperature (°C)	135	165	135/165

a: 1 M of $LiPF_6$ in (EC:EMC) solvent of 30:70 volume ratio.

Celgard's separators are by far the most studied battery separators in literature in terms of physical and chemical properties [207] as well as their use as a part of LIBs [208, 209]. They have been characterized using different characterization techniques such as SEM, air permeability, mercury porosimetry, electrical resistivity analysis … [210-213].

2.3.2. Separator requirements

In LIBs, one crucial function of the separator is to block any electronic contact while allowing ionic transport between the electrodes.

The main requirements [214] for a LIB separator are the following:

- Thickness— LIBs used as a part of portable electronic devices utilize thin microporous separators with a thickness less than 25 μm. Such thin separators help bringing down the resistance which increase both rate capability and capacity. For EV and HEV applications, thicker separators of about 40 μm are required, which brings higher mechanical strength.

- Gurley — Air permeability and electrical resistivity are proportional. For a good electric performance, the separator ought to have small gurley values.

- Porosity— Regularly, LIB separators have porosity in the order of 40%. The control of porosity is vital for battery separators.

- Wettability— The separators must wet out rapidly and totally in battery electrolytes. The deficiency of wetting causes spots on the surface with high resistance.

- Electrolyte absorption and retention— A separator has to be capable of absorbing and retaining the electrolyte to ensure a good ion transport.

- Chemical stability— The separator ought to be stable inside the battery and stand the strong oxidizing and reducing conditions without degrading or reacting then producing impurities. The more prominent the oxidation resistance, the longer the separator will subsist in a battery.

- Dimensional stability— The separator should not twist at the edges when unrolled as this can complicate the cell assembly. The separator ought to additionally not shrink when exposed to the electrolyte.

- Pore measure— A key requirement of LIBs separators is that their pores be sufficiently small to avoid dendritic lithium infiltration through them. LIBs require membranes with submicron pore sizes

All of the aforementioned properties must be optimized in order to qualify a membrane as separator for a LIB. Some of the most important requirements for a separator are reported in table 4.

Table 4: Main requirements for a LIB separator [215]

Parameter	**Goal**
Thickness (µm)[216,217]	<25
Gurley (s)[218]	~25/mil
Pore size (µm)[219]	<1
Porosity (%)	~40
Shrinkage (%)[220]	<5%
High temperature melt integrity (°C)	>150
Wettability	Complete wet out in typical battery electrolytes
Chemical stability	Good stability in battery for long period
Dimensional stability	Necessity of keeping flat and stable in electrolytes

2.4. Positive electrode materials

With the aim of improving the electrochemical performance or to suggest new positive electrode materials with low cost and high intrinsic safety, numerous research work were carried out on the positive electrode in order to improve the properties of commercial $LiCoO_2$ positive electrode material or to find new material families capable of providing better performance than $LiCoO_2$.

The positive electrode materials that represent the source of lithium inside the battery must meet several criteria:

- The materials must contain a readily reducible/oxidizable ion,
- They must react with lithium reversibly and without any major structural change that can destroy its electrochemical performance,
- They should react with lithium very rapidly to give high power,
- They should ideally be good electronic and ionic conductors,
- They should be chemically stable towards electrolytes throughout cycling,
- They must be low cost and environmentally friendly.

2.4.1. Lamellar transition metal oxides

Lithiated transition metal oxides with a lamellar structure rapidly became potential candidates for the positive electrodes as they allow reversible lithium ion insertion at high potentials. Furthermore, they present a high electronic conductivity. For these characteristics, layered transition metal oxides have been used for several years.

The structure of these compounds is composed of a succession of lithium ions and transition metal (Co, Ni, Mn …) ions layers in an oxygenated environment (Fig. 12).

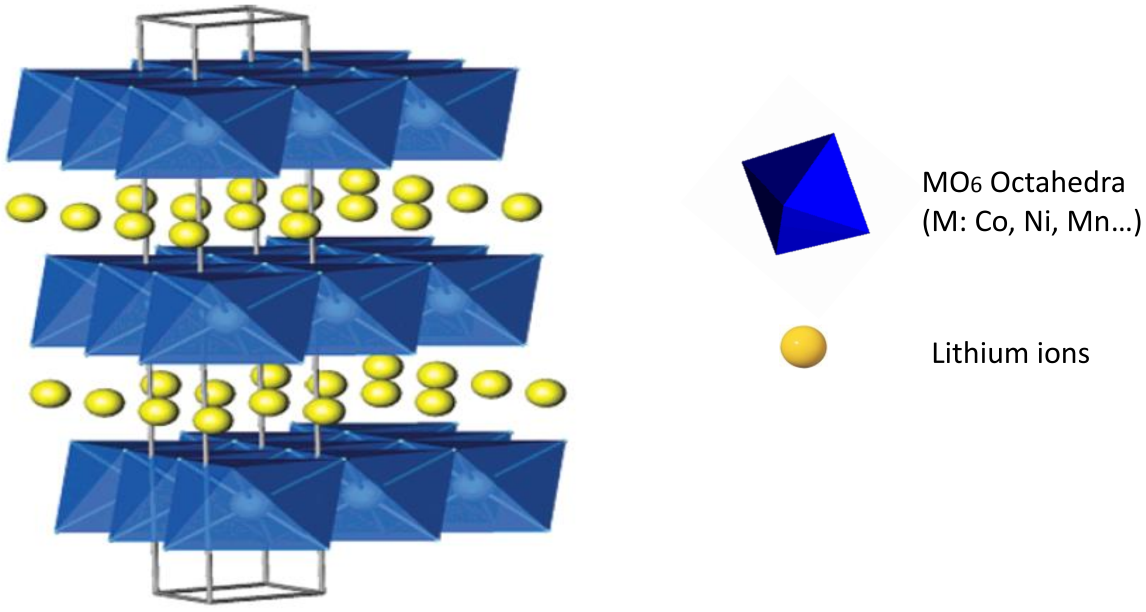

Fig. 12: Schematic representation of $LiMO_2$ cationic distribution [221]

2.4.1.1. $LiCoO_2$

$LiCoO_2$ is the most popular cathode material for commercial LIBs. However, this material has several drawbacks, for instance toxicity, high cost and the deterioration of its structure when more than half lithium ions are extracted at high potentials (greater than 4.5 V). The structural instability of $LiCoO_2$ might create serious problems related to the battery safety. The use of this material is therefore providing limited reversible capacity values between 130 and 140 mAh g^{-1} [222] while the theoretical capacity is 274 mAh g^{-1}.

The aging phenomenon of the $LiCoO_2$ positive electrode can occur either from the material degradation at high voltages around 4.5 V, or because of the significant variations in the lattice parameters induced during the de-intercalation of high amounts of lithium [223] which can lead to micro-cracks at the particles [224].

2.4.1.2. $LiNiO_2$

To replace $LiCoO_2$, various works were carried out on $LiNiO_2$ thanks to its low toxicity and cost compared to $LiCoO_2$. However, the systematic nickel over-stoichiometry induces the presence of divalent nickel ions in the lithium ions sites, therefore the decrease of the electrochemical properties of $LiNiO_2$ [225, 226].

Besides, $LiNiO_2$ suffers from thermal instability at the charged state (deintercalated). These inescapable drawbacks have discarded $LiNiO_2$ [227, 228].

- Ideal structure

$LiNiO_2$ phase crystallizes in the trigonal system and belongs to α-$NaFeO_2$ type structure. The space group is R-3m [229] in Hermann-Mauguin notation, meaning a rhombus-like unit cell with one mirror plane and triple rotary reflections. $LiNiO_2$ structure can more simply be described from a face-centered cubic NaCl type formed by oxygen atoms. The slight difference in ionic radii between lithium and nickel ions (r (Li^+) = 0.76 Å; r (Ni^{2+}) = 0.69 Å) causes ordering of these cations in the oxygen octahedral sites in [111] cubic direction. A rhombohedral lattice distortion is then induced (Fig. 13).

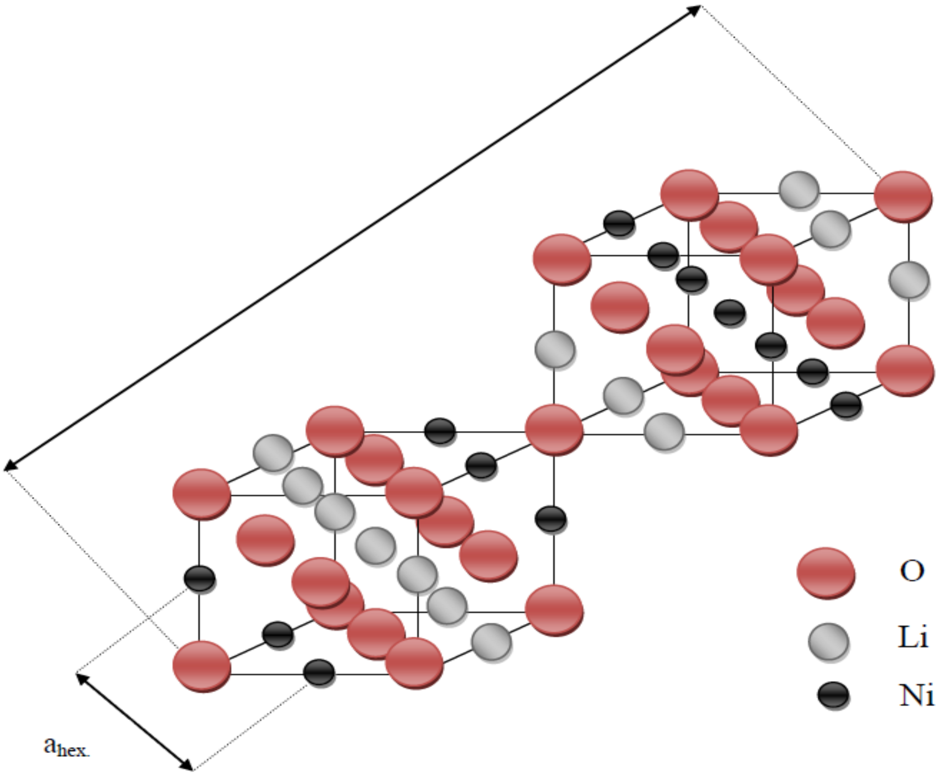

Fig. 13: Schematic representation of the ideal $LiNiO_2$ structure [230]

.

As the rhombohedral unit cell does not allow a simple description of the structure, the hexagonal cell is generally used instead. In the hexagonal cell, the lithium, nickel and oxygen ions occupy the sites 3b (0, 0, 1/2), 3a (0, 0, 0) and 6c (0, 0, $z_{ox.}$) of the R-3m space group respectively (Fig. 14). This structure is characterized by its lattice parameters $a_{hex.}$ and $c_{hex.}$, characteristics of the intrasheet distance Ni-Ni and the interlayer distance ($c_{hex.}/3$) [230].

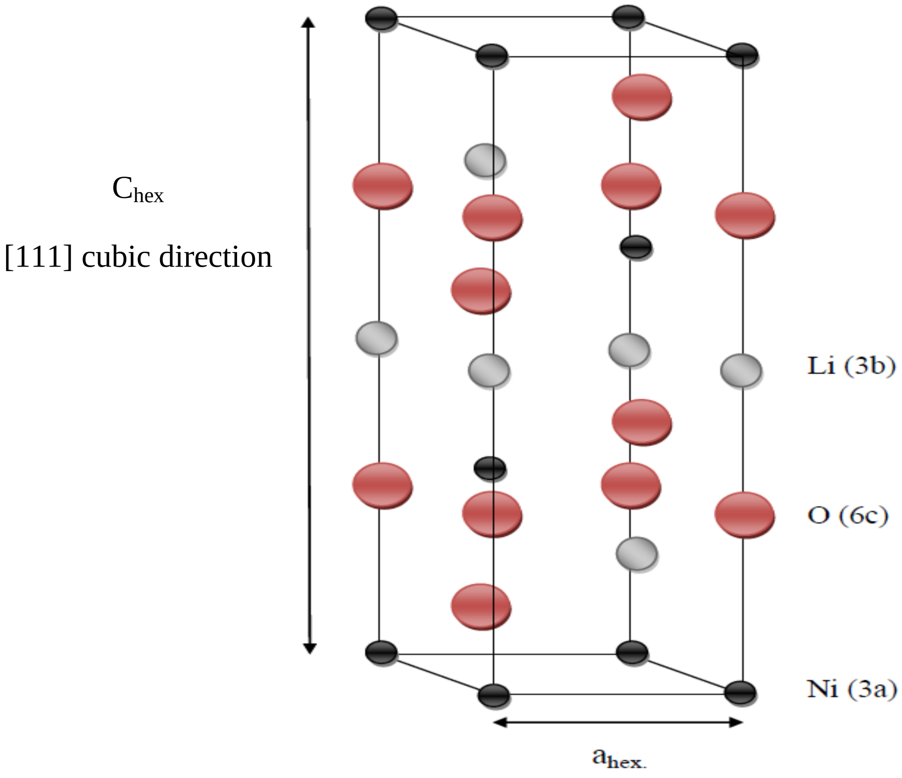

Fig. 14: Schematic representation of an ideal LiNiO2 hexagonal lattice [230]

.

Due to its pronounced two-dimensional character, the structure can also be described as a stack of NiO_2 sheets consisting of NiO_6 octahedra with common edges. Lithium ions can occupy the octahedral sites between the sheets forming the interlayer space [231] (Fig. 15a). This structure is of O3 type, meaning that three sheets are required for describing the hexagonal lattice, and the lithium ions are located in octahedral sites.
NiO_2 sheets are characterized by strong Ni-O bonds, since they have a strong covalent character, which is why they form a rigid host structure. In contrast, Li-O bonds are weak as they have more ionic character and allow then the intercalation and de-intercalation of lithium ions without structural modification of the host network. This configuration and the anisotropic nature of the structure give this class of materials interesting properties and motivates their use as electrode materials for battery applications [232].

- Real structure

Many studies have shown the difficulty of obtaining stoichiometric $LiNiO_2$ [232]. In general, the Li/Ni ratio is less than 1 and the real formula of the lithium nickelate is $Li_{1-z}Ni_{1+z}O_2$ (z> 0) [233,234]. The 3b sites of the interlayer space are jointly occupied by lithium and excess nickel ions (Fig. 15b). This deviation from stoichiometry is mainly caused by the relative instability of Ni^{3+} ions compared to Ni^{2+} ions [235], resulting in a charge compensation of z Ni^{2+} on the lithium sites. The real cationic distribution is then: $[Li_{1-Z}Ni^{2+}_{z}]_{3b}\,[Ni^{2+}_{z}Ni^{3+}_{1-z}]_{3a}O_2$.

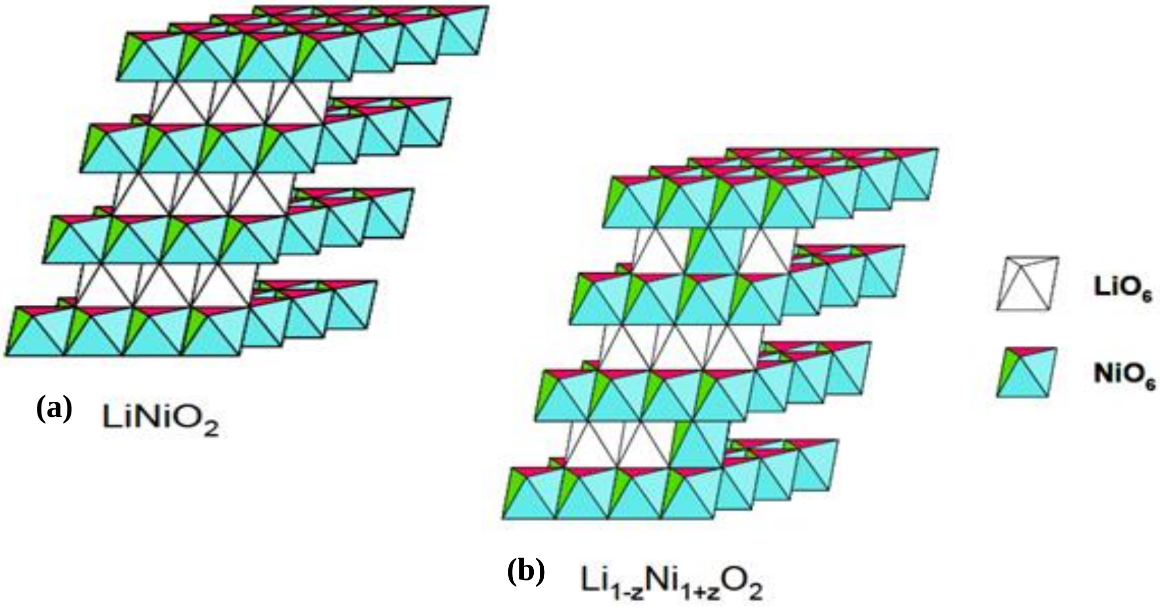

Fig. 15: Schematic representation of cationic distribution in $LiNiO_2$ in the case of an ideal structure (a) and a real structure (b) [230]

.

2.4.1.3. $LiNi_xMn_yCo_{1-x-y}O_2$

Research has later been oriented towards the substitution of nickel by cobalt and / or manganese to increase the structural and thermal stability of the positive electrode and therefore to produce a battery with a longer life span. Several papers have been devoted mainly to the study of the electrochemical properties of materials belonging to the $LiNi_xMn_yCo_{1-x-y}O_2$ materials given their interesting properties.

Indeed, several NMC phases have been studied as positive electrode materials such as $LiNi_{0.1}Mn_{0.1}Co_{0.8}O_2$ [236], $LiNi_{0.3}Mn_{0.3}Co_{0.4}O_2$ [237], $LiNi_{0.4}Mn_{0.4}Co_{0.2}O_2$ [238], $LiNi_{0.5}Mn_{0.3}Co_{0.2}O_2$ [239], $LiNi_{0.7}Mn_{0.2}Co_{0.1}O_2$ [240], $LiNi_{0.6}Mn_{0.1}Co_{0.1}O_2$ [241]. The motivation was to investigate the influence of the partial substitution of cobalt with manganese and nickel and consequently the determination of the material that has the best structural, morphological and electrochemical properties.

In this thesis work, pristine $LiNi_{0.6}Mn_{0.2}Co_{0.2}O_2$ and Al and/or Fe substituted NMC(3:1:1) phases has been investigated.

The structural and morphological properties of $LiNi_{0.6}Mn_{0.2}Co_{0.2}O_2$ synthesized by self-combustion method will be presented as well as a detailed study of the optimization of the electrochemical properties of the prepared NMC phase (Ch. IV and Ch. V).

Since the electrochemical performance of cathode materials for rechargeable LIBs are strongly related to their crystalline structure and their structural changes during cycling, a study of the material reaction mechanism during charge has been conducted to assess the structural stability of NMC(3:1:1) in the charged state.

At high temperatures and in the charged state, the layered transition metal oxides decompose and release oxygen. This degassing can contribute to an increase in the internal pressure, which may lead in extreme cases to a thermal runaway [242]. For this purpose, study of the thermal stability in the charged state of the pristine and double-substituted NMC (3:1:1) materials was interesting to carry out (Ch. VI).

2.4.2. Spinel transition metal oxides

$LiMn_2O_4$ is an intensively studied material with a spinel type structure. The latter consists of manganese occupying the octahedral sites and lithium mainly filling the tetrahedral sites (Fig. 16). The anionic network consists of oxygen octahedra, the paths for lithiation and delithiation form a three dimensional network.

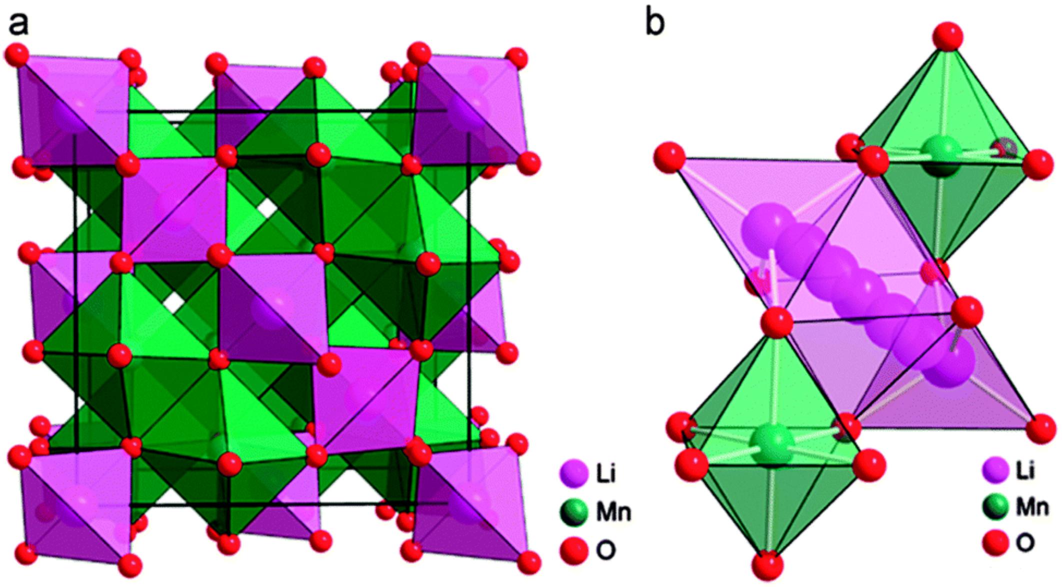

Fig. 16: Schematic representation of the atomic distribution of LiMn2O4 (a) and lithium diffusion pathways (b) [243]

$LiMn_2O_4$ has been widely studied as a cathode for LIBs thanks to its low cost and toxicity. However, this material presents a high capacity loss during cycling. In fact, the main problem regarding the use of $LiMn_2O_4$ as commercial cathode material is related to the phase changes that can occur during cycling [244,245].

The substitution of manganese with other metals and in particular iron [246], cobalt [247-249] and chromium [250] allows a considerable stabilization of the structure during cycling and therefore a significant improvement of the electrochemical performance. The substitution of manganese by nickel resulting in the composition $LiMn_{1.5}Ni_{0.5}O_4$ remains a widely studied phase in this material family [251, 252].

2.4.3. Olivines

The phospho-olivine compounds combine several interesting properties that offer them a wide field of applications.

$LiFePO_4$ shows excellent structural stability in the charged state ($FePO_4$) and low volume changes (Fig. 17). It is very safe and secure material in addition to its low cost and its specific energy which is comparable to that of $LiCoO_2$.

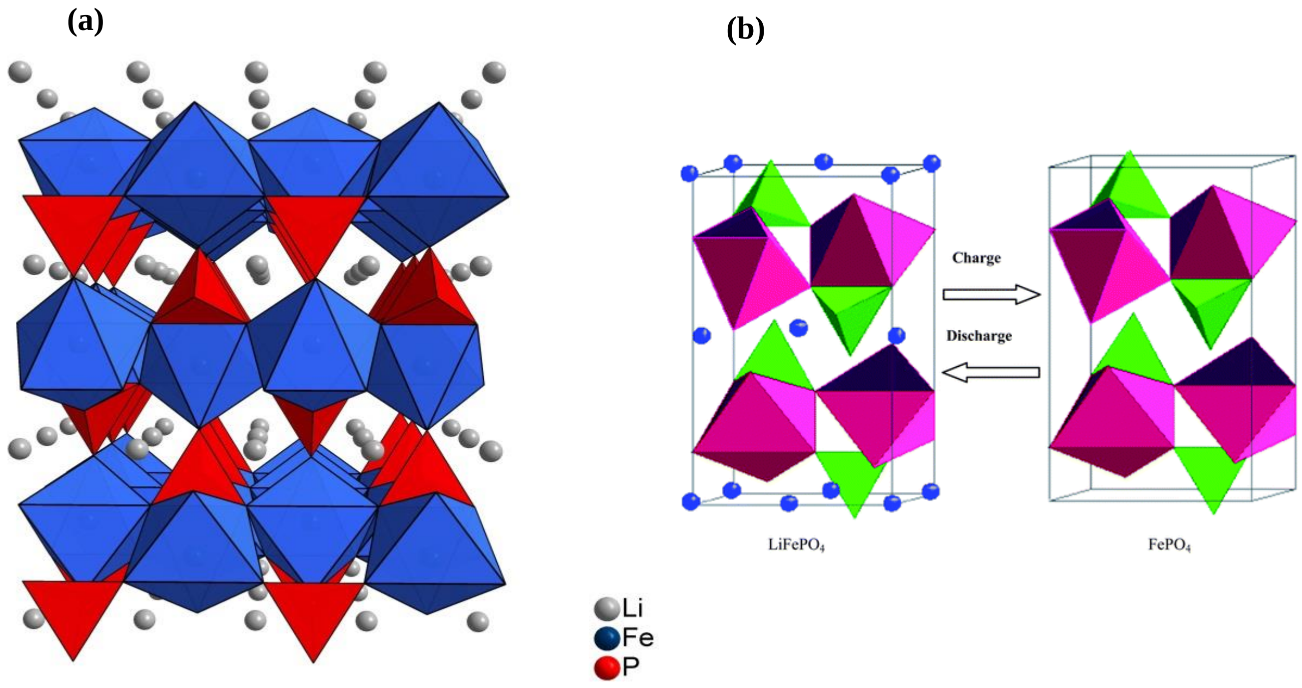

Fig. 17: Schematic representation of the atomic distribution of (a) LiFePO4 (b) and FePO4 [253,254]

.

$LiFePO_4$ operating potential is located in the electrolytes electrochemical stability range, which allows avoiding any possible reaction with the electrolytes organic compounds. In addition, $LiFePO_4$ does not release oxygen which is responsible for batteries explosions and fires.

All of $LiFePO_4$ material strengths (high reversible capacity, excellent cyclability, low cost, reduced environmental harm, high thermal stability, safety) motivate its use in commercial LIBs.

Nevertheless, the low electronic conductivity of this material remains a major drawback. Decreasing the particle size of $LiFePO_4$ is one approach that helped improving the contact between the particles and decreasing the average distance traveled by lithium [255-258]. The addition of a conductive agent is another approach that may improve its conductivity [259-263].

In fact, more compositions belonging to the phosphor-olivine materials family exist and have been topics of numerous research works. The main properties for some of these materials are summarized in table 5.

Table 5: Characteristics of some phospho-olivine cathode materials

	$LiFePO_4$ [264]	**$LiMnPO_4$ [265]**	**$LiCoPO_4$ [266]**	**$LiNiPO_4$ [267]**
Advantages	- High thermal stability - Elevated theoretical capacity	- High operating potential : 4.1V vs Li^+/Li - High theoretical capacity	- High potential ~ 4.8V vs Li^+/Li - High theoretical capacity - Low volume change of the lattice	- Elevated redox potential: 5.1V vs Li^+/Li - High theoretical capacity - Low volume change of the lattice
Drawbacks	- Low redox potential: 3.4V vs Li^+/Li - Low electronic conductivity	- High volume change during cycling - Low electronic conductivity	- Low electronic conductivity	- Low electronic conductivity

2.5. Current collectors

Great interest and effort have been dedicated to the development of novel and high performance cathode and anode materials as well as electrolyte [268-279]. In contrast, far less consideration has been given to the current collectors.

Current collectors for LIBs are fabricated using metal foils. Most often copper foil is used for the negative electrode and aluminum foil is used for the positive electrode, the thickness of these sheets range from 10 to 50 micrometers [280]. During the LIB manufacturing process, anode and cathode active materials slurries are coated onto the appropriate metallic foils that serve as electrical conductors and mechanical supports [281].

Enhanced cyclability, energy and power densities of the Li ion batteries under operation conditions involve not only great performance electrode materials, but also good adhesion properties of the electrode composite at its current collector interface throughout the operation period.

Therefore, to preserve the mechanical durability of the electrodes and improve the adhesion properties of the current collectors, many approaches such as roll pressing, surface roughing and addition of binders are applied. Such mechanical improvements have demonstrated better electrochemical performance of batteries [282-284].

Moreover, commercial current collectors might not be 100% pure in terms of metal content. Impurities can lead to corrosion which can result in an increase of the battery´s internal resistance then to a capacity fade during cycling [285]. On the other hand, some metals, when they are in contact with the electrolyte, may passivate and develop an anti-corrosion ability such as the formation of a protective film [286-291].

3. Lithium ion battery operating principle

The operating principle of a lithium-ion battery is based on the conversion of chemical energy into electrical energy through two redox reactions taking place at both negative and positive electrodes (Fig. 18)

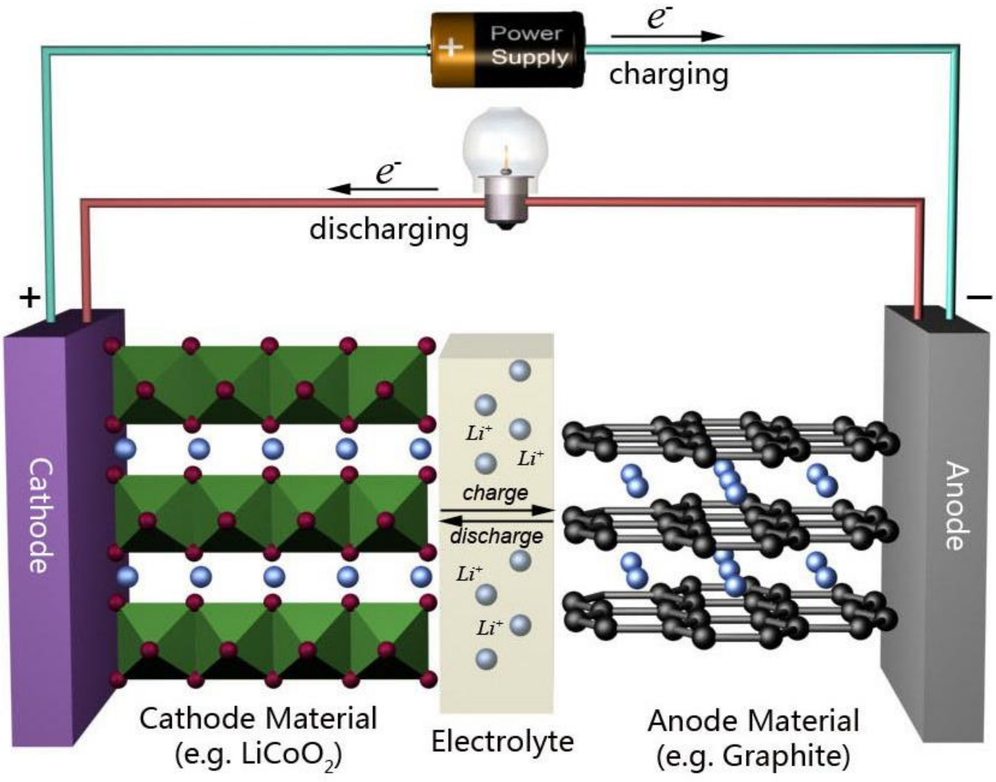

Fig. 18: Operating principle of a LIB [292]

During charging, electron flow is imposed by the external circuit, and an equivalent molar amount of lithium ions is migrating through the electrolyte which should be ionically conductive and electronically insulating. This allows the insertion of lithium ions in the negative electrode and their reduction.

Reverse phenomena take place spontaneously during the discharge of the battery. The advantage of such a system is related to the possibility of storing electrical energy in chemical form during the charge, which can be restored at any time in electrical form during the discharge of the accumulator.

In the case of cells used in the laboratory, the negative electrode consists of metallic lithium. Although the reversibility of the Li^+/Li couple is poor in terms of long-term cycling, the fixed value of the Li^+/Li couple potential during cycling allows observing directly the potential variation of the studied positive electrode material.

The performance of a battery is quantified by several variables [293] including:

Capacity (Q): The capacity of a battery is the amount of supplied electricity; it is given by the Faraday equation (2.1):

$$Q = \int_0^t I.dt \qquad (2.1)$$

I (A): is the current passing through the battery,t (h) is the duration of current flow.

The capacity unit is Ah, but it can also be expressed as a mass, surface or volume capacity.

From the Faraday equation, it is possible to calculate the number of electrons per unit formula inserted into the host material (2.2). It is often equated to the number of Li^+ ions inserted per mole of active material:

$$Q = \frac{I.t}{m} = \frac{\Delta x.F}{3600.\mathrm{M}} \leftrightarrow \Delta x = \frac{3600.M.Q}{F} \qquad (2.2)$$

m (g) is the active mass of the host material, M (g / mol) is the molar mass of the active material, Δx: is the number of electrons inserted per mole of active material, F: is the Faraday constant (96485 C/mol)

Energy (W): The energy of an electrochemical cell is given by the equation (2.3):

$$W = \int_0^t U.I.dt \qquad (2.3)$$

U (V) is the voltage, I (A): is the current passing through the cell, t (h) is the duration of current flow.

The energy of the cell is expressed in Wh.

Power (P): The power of a battery is defined as the delivered energy per unit time and is expressed by the equation (2.4):

$$P = \frac{W}{t} \qquad (2.4)$$

Capacity retention: the number of times the battery is charged and discharged without losing more than half of its initial capacity. This variable is related to the reversibility of electrochemical processes and is very important from the applications point of view.

Efficiency: it corresponds to the fraction of electrical energy stored in the Li-ion battery during charging which is recoverable during discharge. It can also refer to the percentage of electric charge stored in the battery during charging, which is recoverable during discharge, the used term in this case is the Coulomb efficiency.

Cycling rate (C/n): this variable means that the theoretical capacity Q_{max} will be obtained by charging the battery for n hours.

III. Characterization methods

In order to analyze the NMC cathode materials that were studied throughout this PhD work structurally, morphologically, electrochemically… several characterization techniques were used such as X-Ray diffraction, scanning electron microscopy, thermogravimetry coupled with differential thermal analysis, galvanostatic cycling, cyclic voltammetry… In the following chapter, a short overview on the experimental conditions of the utilized characterization methods will be presented. Thereafter, in chapters IV, V and VI, there will be only a discussion of the results without mentioning the experimental conditions.

1. Structural characterization

1.1. Characterization by X-ray diffraction (XRD)

The X-ray diffraction characterization method can provide important information related to the structure, such as the purity of the phases, the crystallographic structures... The X-ray diffraction patterns were recorded by a Siemens D5000 diffractometer in reflection mode with Cu Ka radiation under the following conditions: (2θ between 10 ° and 80 °, steps of 0.02 ° with a rest time of 1 second per step. To accurately characterize the materials structure, it is necessary to perform a refinement of the diffraction data by the Rietveld method (Ch. III.1.2). The experimental diffraction patterns must then be of good quality. In this case, the rest time per step was set to 3 seconds instead of 1 s.

1.2. Structural refinement by Rietveld method

The structure of the different samples studied in the framework of this thesis was determined through XRD refinement by Rietveld refinement method using Fullprof software [294]. This method is based on the minimization of the difference between the observed and calculated intensities $y = f(2\theta)$, by a least squares approach. The refinement is performed in two steps: full pattern matching then Rietveld.

1.2.1. Full pattern matching (or Le Bail method)

The refined parameters are:

- The continuous background estimated by a linear interpolation between points for which no peak contribution exists,
- The lattice parameters,
- The profile parameters of the diffraction lines: $\eta 0$, X, U, V, W. The diffraction lines profile is described by a pseudo-Voigt function (3.1) which is a linear combination of Gaussian (G) and Lorentzian (L) functions:

$$PV = \eta L + (1-\eta) G \qquad (3.1)$$

The form factor η, which defines the form of the peaks between the Gaussian ($\eta = 0$) and Lorentzian ($\eta = 1$) limits, varies with the diffraction angle 2θ according to the equation (3.2):

$$\eta = \eta_0 + X\,(2\theta) \qquad (3.2)$$

where X takes into account the evolution of the form factor depending on the angle 2θ. The linewidth (H) varies with 2θ according to Caglioti formula (3.3):

$$H^2 = U\tan^2\theta + V\tan\theta + W \qquad (3.3)$$

where U, V and W are the Caglioti coefficients.

1.2.2. Rietveld method

For further refinement, we proceed by Rietveld method. The lattice and profile parameters are set initially to the obtained values in Full Pattern Matching. The structural model considered to describe all phases reported in this thesis is isotypic to that of α-$NaFeO_2$ and described by the space group R-3m. Lithium ions mainly occupy the 3b crystallographic site (0, 0, ½), the transition metal ions the 3a site (0, 0, 0) and the oxygen ions the 6c sites (0, 0, z~0.25). The parameters successively refined are the scale factor, the ion occupancy in the different crystallographic sites and the isotropic atomic displacement factors (identical for ions occupying the same site). Finally, the lattice parameters and profile are again refined.

In order to quantify the agreement between the experimental and calculated diffraction patterns for a given structural hypothesis, we use the R_{wp} (3.4) and R_{Bragg} (3.5) reliability factors:

- The weighted profile factor:

$$R_{wp} = \sqrt{\frac{\sum_i w_i.[y_{i(obs)} - y_{i(calc)}]^2}{\sum_i wi.y_{i(obs)}{}^2}} \qquad (3.4)$$

yi (obs) is the observed intensity for a 2θi angle, yi (calc) is the calculated intensity for the 2θi angle, wi is the statistical weight of each intensity.

- Bragg factor:

$$R_{Bragg} = \frac{\sum_i |I_{i(obs)} - I_{i(calc)}|}{\sum_i I_{i(obs)}} \qquad (3.5)$$

I_i is the integrated intensity of the i reflection.

R_{Bragg} is very sensitive to intensity variations of the diffraction line, thus to changes in the structural parameters. Direct observation of the difference curve between the experimental and calculated profiles provides an effective and quick way to judge the quality of the refinement.

Note that the standard deviations, given in the refinement output file are calculated by considering that the counting statistics is the only source of error. Systematic errors caused by background noise or by the use of an inadequate model are not considered. Several methods to take into consideration the standard deviations exist, including one that involves their multiplication by S_{cor} factor (if it is greater than 3) provided in the refinement resulting file [295].

1.3. Electron paramagnetic resonance

Electron Paramagnetic Resonance (EPR) is a non-destructive technique that refers to the ability of some electrons to absorb and re-emit the energy of an electromagnetic radiation when placed in a magnetic field. Only unpaired electrons that are present eg, in radical chemical species and transition metal complexes, exhibit this property.

As the majority of the stable chemical species are having pairs of paired electrons, this technique allows bringing out the chemical species having unpaired electrons.
Furthermore, because of the importance of the magnetic moment of the electron spin, this technique is likewise very sensitive.
The classical EPR parameters are the linewidth, the peak-to-peak amplitude and the g factor [296].

EPR spectra were recorded using a continuous wave Bruker X-band spectrometer ELEXYS E500 with a field modulation of the order of 100 kHz in the temperature range [77-295K]. For exact g-factor determination, a standard consisting of a hyperfine structure (hfs) line of the $Cu^{2+}(dtc)_2$ complex in benzene (noted by $Cu^{2+}L_2$) was utilized. The positions of the studied samples and the used $Cu^{2+}L_2$ standard in the resonator are independent. Recording takes place at room temperature. In all the experiments conducted in this work, $Cu^{2+}L_2$ hfs (m= - 1/2) has been utilized as reference line with an amplitude peak of g-factor equal to 2.025.

2. Physico-chemical characterization

2.1. Morphological characterization by scanning electron microscopy (SEM)

The micrographs of the studied materials were recorded by a high-resolution scanning electron microscope (Hitachi S-4800 II).

For the SEM the samples were fixed on a carbon adhesive disk and sputtered with an ultra-thin gold layer (~10nm) to prevent any possible charge accumulation on the surface.

SEM images were taken on several positions of the powder with the same magnifications to improve the statistics.

2.2. Specific surface measurement by Brunauer Emmett and Teller (BET)

The specific surface area measurements were conducted by the Brunauer , Emmet and Teller (BET) method at the Indian institute of technology Delhi, using Gemini 2360 Surface Area Analyser.

BET measurements consist of measuring the adsorbed nitrogen volume at the sample surface at liquid nitrogen temperature (77 K). The studied samples were dried at 120°C overnight under a nitrogen purge. During the measurement, the U-tube containing the sample is cooled in liquid nitrogen. Nitrogen molecules are adsorbed on the sample surface. Returning to room temperature, the gas molecules are desorbed. The BET theory assumes that the adsorbed gas molecules form, in dynamic equilibrium with nitrogen, a monolayer at the sample surface allowing then connecting the accessible surface of the sample to the volume of the adsorbed gas. The measured area is divided by the sample mass to obtain a specific surface value [297].

3. Thermal analysis by thermogravimetry coupled with differential thermal analysis (DTA-TG)

Thermogravimetric analysis (TGA) is an analytical technique that involves measuring the mass change of a sample as a function of temperature. Such analysis requires good accuracy on three parameters: mass, temperature and temperature variation. Thermogravimetric and differential thermal analysis were carried out simultaneously using Netzsch STA 409 device in the temperature range between 20 and 1020°C with a scan rate of 5°C/min

The inert reference used is alumina Al_2O_3 and the amount of the sample taken for each measurement is 20 mg ± 1mg.

4. Electrochemical characterization

The prepared LIBs consist of metallic lithium as negative electrode, organic based liquid electrolyte composed of $LiPF_6$ salt (1 mol/L) dissolved in a mixture of ethylene carbonate (EC) and dimethyl carbonate (DMC) in volume proportions (1: 1). The positive and negative electrodes are separated by Celgard polyethylene separator (Ch. II.2.3.1). The ideal slurry composition for the cathode material was proven in this work to be 75 wt. % active material, 10 wt. % carbon black serving as conductive agent and 15 wt. % polyvinylidene fluoride (PVDF) in N-methyl-2 pyrrolidone (NMP) utilized as binder.

The slurry is then coated on Al current collectors. An extensive study concerning the slurry composition was carried out by varying the weight percentage of each component then testing the morphology of the obtained coatings. This study was not reported in this work.

Cathodes are then cut to a size compatible for a standard CR2016 coin cell, dried at 120°C for 12 h and weighed. The coin cells were then assembled in a glove box under a dry and high purity argon atmosphere using MSK-110 Hydraulic Crimping Machine, MTI Co.

The charge/discharge process was characterized galvanostatically over a potential range of 2.5 to 4.4 V versus Li/Li^+ for slow rates and from 2.8 to 4.6 V versus Li/Li^+ for fast rates using a VMP BioLogic multichannel potentiostat/galvanostat .

The battery cycling curve corresponds to the evolution of the positive electrode potential with time and will directly describe the electrochemical behavior of the positive electrode material.

IV. Optimization of the synthesis conditions

1. Introduction

Even though NMC materials lead to batteries that deliver high voltages and very good energy densities, there is a high expectation that the properties of these materials can be adjusted in order to improve the structural stability as well as the performance. Two ways were selected throughout this PhD work:

- Optimization of the synthesis conditions since the cycling behavior of NMC cathode materials significantly depends on the preparation conditions such as synthetic route and annealing conditions [298,299]. It was established that the annealing temperature and plateau of the as-prepared NMC materials influence strongly the material´s morphology including particle size as well as the electrochemical performance.

- Cationic substitution to a transition metal. This can allow structural stability improvement and reduces the capacity loss during cycling.

In the present chapter, the preparation by two synthesis methods and different annealing conditions of NMC cathode materials with the compositions $LiNi_{0.6}Mn_{0.2}Co_{0.2}O_2$ (NMC 3:1:1) and $LiNi_{1/3}Mn_{1/3}Co_{1/3}O_2$ (NMC 1:1:1) and their characterization will be discussed. The aim is to demonstrate that the structural, morphological and electrochemical properties of the obtained materials can be fine-tuned via the preparation conditions such as annealing temperature and plateau, annealing atmosphere, time between synthesis and annealing and the effect of pre-annealing.

In the following all potential values refer to Li^+/Li if not otherwise stated.

2. Synthesis methods

2.1. Co-precipitation

The NMC materials (NMC 3:1:1) and (NMC 1:1:1) were prepared using the co-precipitation synthesis method. The latter involves the co-precipitation of a mixed hydroxide in aqueous solution, using a method described by Caurant et al. [300].
An aqueous solution (1 mol/L) of $Ni(NO_3)_2.6H_2O$, $Mn(NO_3)_2.xH_2O$ and $Co(NO_3)_2.6H_2O$, with the molar ratios (Ni : Mn : Co) = (0.6 : 0.2 : 0.2) and (Ni : Mn : Co) = (1/3 : 1/3 : 1/3) for (NMC 3:1:1) and (NMC 1:1:1) respectively, is added drop by drop using a burette in a basic solution (LiOH (1M) / NH_4OH (3M)) under magnetic stirring. The initial ratio Li / (Ni + Co + Mn) is adjusted to 1 to prevent the formation of overlithiated phases $Li_{1+x}(Ni_{0.6}Mn_{0.2}Co_{0.2})_{1-x}O_2$ and $Li_{1+x}(Ni_{1/3}Mn_{1/3}Co_{1/3})_{1-x}O_2$ [301].

A green precipitate with blue supernatant was formed immediately especially for NMC (3:1:1) (Fig. 19). It corresponds to the presence of nickel ions complexed with ammonia. On the other hand, the precipitate takes rather a brown color, characteristic of the oxidation in air of Mn^{2+} to Mn^{4+} ions, for NMC (1:1:1) (Fig. 19), which must be due to the higher amount of manganese in this material composition. Solvents (water, ammonia) are then evaporated under vacuum at 80°C for 3 h by means of a rotary evaporator. Afterwards, the coprecipitate was dried for 12h at 105°C and pre-annealed at 500°C for 5 h in air. Prior to annealing, the pre-annealed residue is milled mechanically using an agate mortar.

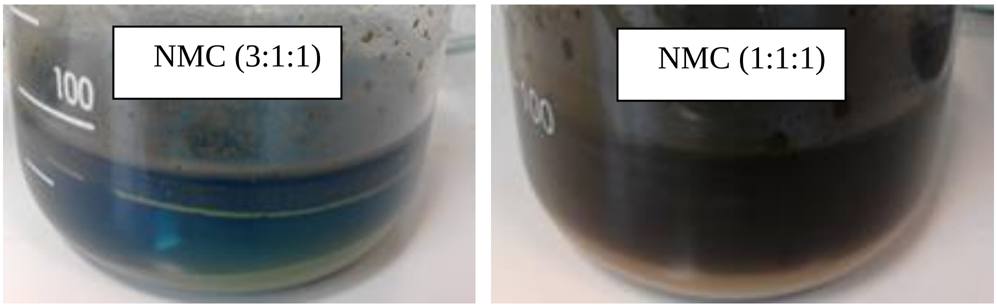

Fig. 19: $LiNi_{0.6}Mn_{0.2}Co_{0.2}O_2$: NMC (3:1:1) and $LiNi_{1/3}Mn_{1/3}Co_{1/3}O_2$: NMC (1:1:1) precipitates during synthesis by co-precipitation

2.2. Self-combustion

The self-combustion method has been used for the synthesis of the two positive electrode materials NMC (3:1:1) and NMC (1:1:1). This synthetic route has several advantages:

- it is a fast and inexpensive process,
- it can be done with simple equipment,
- it allows a good homogenization of the starting materials and therefore their excellent reactivity, which provides phases with high purity even by using moderate temperatures and short duration thermal treatments.

Self-combustion synthesis method is widely used for the preparation of materials characterized by very good homogeneity and formed by small size particles. Several studies have shown that the materials prepared by self-combustion method present better properties than those synthesized by conventional methods [302-304].

The synthesis is carried out in aqueous phase according to the reaction equation (4.1):

$$1.05\ LiNO_3 + x\ Ni(NO_3)_2 + y\ Mn(NO_3)_2 + 1\text{-}x\text{-}y\ Co(NO_3)_2 + 2/3\ C_{12}H_{22}O_{11}$$

$$\Downarrow$$

$$Li\,Ni_x\,Mn_y\,Co_{1-x-y}\,O_2 + NO_x + N_2 + CO_2 + H_2O \qquad (4.1)$$

The procedure consists of preparing aqueous solutions (1M) of $LiNO_3$ (99 %, Alfa Aesar), $Ni(NO_3)_2.6H_2O$ (98 %, Alfa Aesar), $Co(NO_3)_2.6H_2O$ (98 %, Alfa Aesar) and $Mn(NO_3)_2.xH_2O$

(99.98 %, Alfa Aesar). Lithium is used in excess in order to compensate its loss by evaporation during annealing and to limit the lithium deficiency in the prepared phase. Stoichiometric amounts of reactants are mixed under magnetic stirring with an aqueous solution of sucrose used as a combustion agent. The molar ratio of sucrose has been optimized through several works in the literature in order to avoid the possibility of explosion that might be due to an excess of sucrose in the solution [302-309]. The solution is heated in a sand bath at 120°C for 2 hours. This gives rise to a foamy mass after total evaporation of water. Combustion is triggered spontaneously and spreads over the entire surface

The different steps of the self-combustion synthesis method are illustrated in figure 20.

The obtained powder is grinded mechanically, by an agate mortar, before undergoing the heat treatment.

Fig. 20: Steps of self-combustion synthesis method. From left to right, the first picture presents a crystallizer with the mixed solution of transition metal nitrates and sucrose heated by means of a sand bath, then in the second picture the solution becomes foamy after evaporation of water. The last picture presents the self-combustion product

.

3. Annealing plateau

The annealing involves heating the samples to 900°C with a temperature rate equal to 5°C/min, then maintaining that temperature (900°C) for 12 h and 24 h for the samples prepared by co-precipitation synthesis method and for 1 h, 12 h and 24 h for the samples synthesized by self-combustion method.The X-ray diffraction patterns of $LiNi_{0.6}Mn_{0.2}Co_{0.2}O_2$ and $LiNi_{1/3}Mn_{1/3}Co_{1/3}O_2$ prepared by the two different synthesis methods and having undergone different heat treatments are shown in Figures 21 and 22.

For all the phases, a structure α- $NaFeO_2$ type is obtained according to the X-ray diffraction patterns. All the peaks can be indexed in the space group R-3m.

The intensity ratio of the diffraction lines (003)/(104) is an important parameter to evaluate the cation distribution as well as the lattice crystallinity [310]. It was found that the increase of this ratio (>1) is related to the formation of a well ordered phase.

Accordingly, in our case, the highest values for the (003)/(104) ratio were obtained for the phase $LiNi_{0.6}Mn_{0.2}Co_{0.2}O_2$ prepared by self-combustion and annealed at 900°C for 1h (table 6) and for the phase $LiNi_{1/3}Mn_{1/3}Co_{1/3}O_2$ prepared by co-precipitation method and annealed at 900°C during 12h (table 7).

From the XRD analysis, it is then obvious that reduced annealing plateaus are generally ideal to achieve well-ordered crystalline phases.

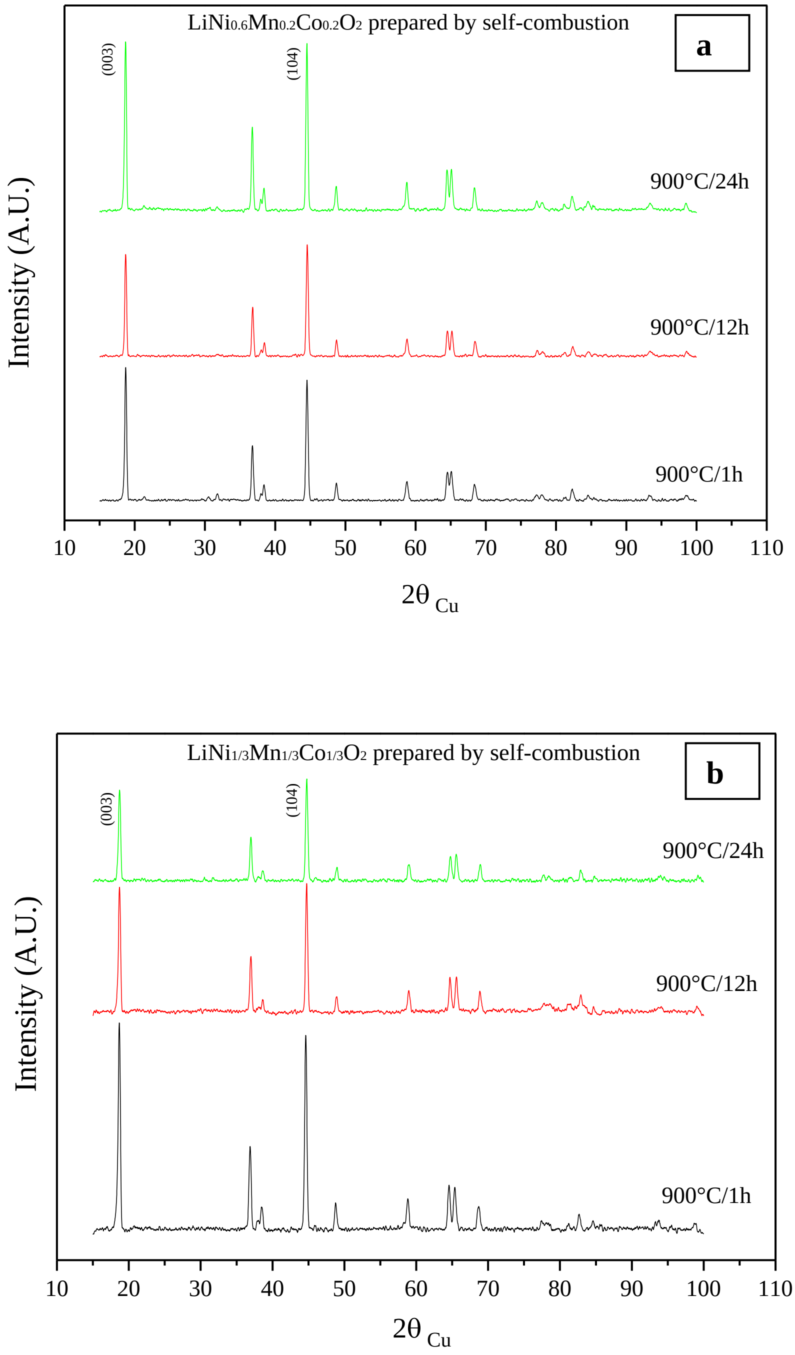

Fig. 21: Comparison between X-ray diffraction patterns of the materials $LiNi_{0.6}Mn_{0.2}Co_{0.2}O_2$ (a) and $LiNi_{1/3}Mn_{1/3}Co_{1/3}O_2$ (b) synthesized by self-combustion method

Table 6: Intensity ratios of the diffraction lines (003)/(104) for the phases prepared by self-combustion synthesis method

(003) / (104) **Phases**	**1h**	**12h**	**24h**
$LiNi_{0.6}Mn_{0.2}Co_{0.2}O_2$	1.10	0.96	1.01
$LiNi_{1/3}Mn_{1/3}Co_{1/3}O_2$	1.06	0.99	0.97

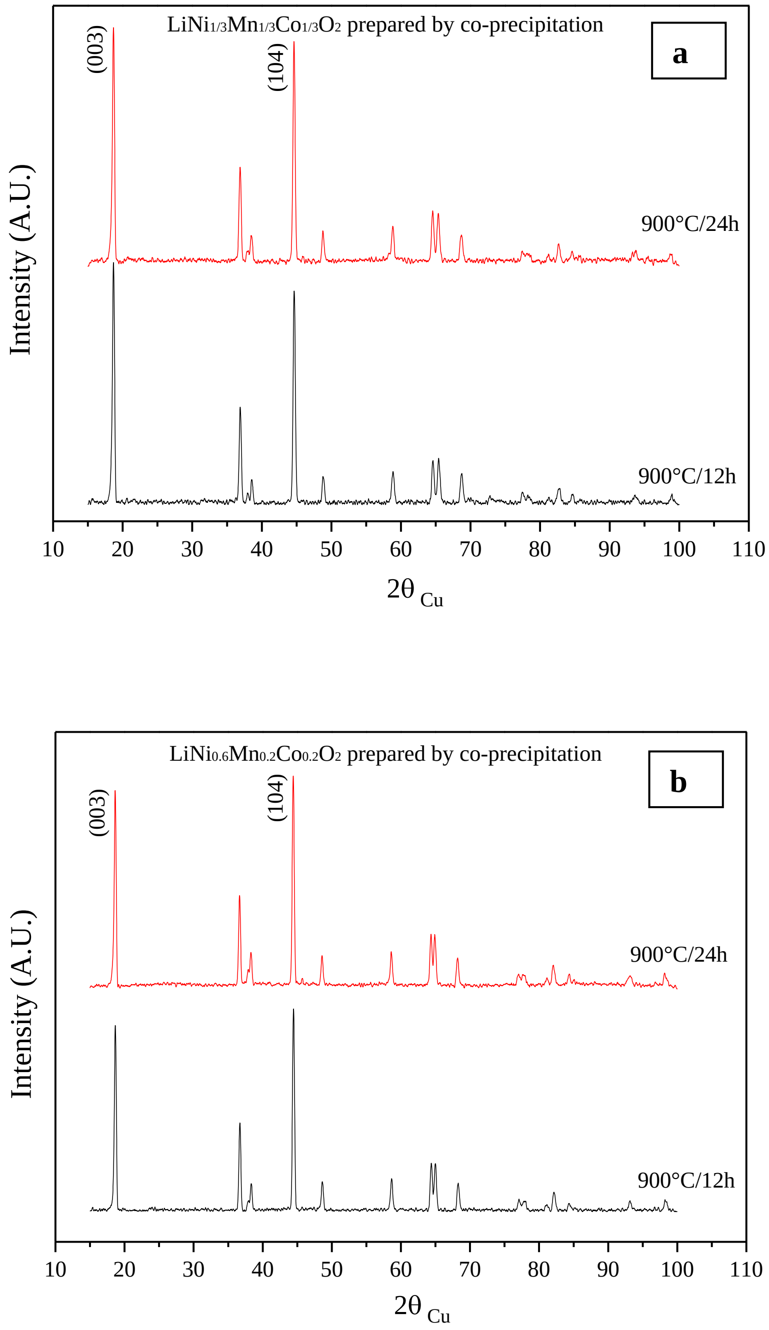

Fig. 22: Comparison between X-ray diffraction patterns of the materials $LiNi_{0.6}Mn_{0.2}Co_{0.2}O_2$ (a) and $LiNi_{1/3}Mn_{1/3}Co_{1/3}O_2$ (b) synthesized by co-precipitation method

Table 7: Intensity ratio of the diffraction lines (003) / (104) for the phases prepared by co-precipitation synthesis method

(003) / (104) Phases	12h	24h
$LiNi_{0.6}Mn_{0.2}Co_{0.2}O_2$	0.91	0.97
$LiNi_{1/3}Mn_{1/3}Co_{1/3}O_2$	1.14	1.03

The particle size and morphology of the prepared phases were analyzed by SEM (Figs. 23 and 24).

For the two phases NMC (3:1:1) and NMC (1:1:1) prepared by self-combustion method, when increasing the annealing plateau, an evolution of the morphology from small and well defined to less defined particles is observed especially for the composition (3:1:1). Larger aggregates of primary particles are also observed for the longer annealing periods.

In terms of the co-precipitation method, there is no remarkable dependence on annealing. The particles in this case are relatively well defined however with bigger size especially for the compound (3:1:1).

It should be noted then that with the co-precipitation synthesis method, it is necessary for the phases to undergo longer annealing periods, unlike the combustion method that has shown the possibility to obtain crystalline phases with a morphology consisting of small particle size even at 1 h annealing plateau. This reduces energy consumption.

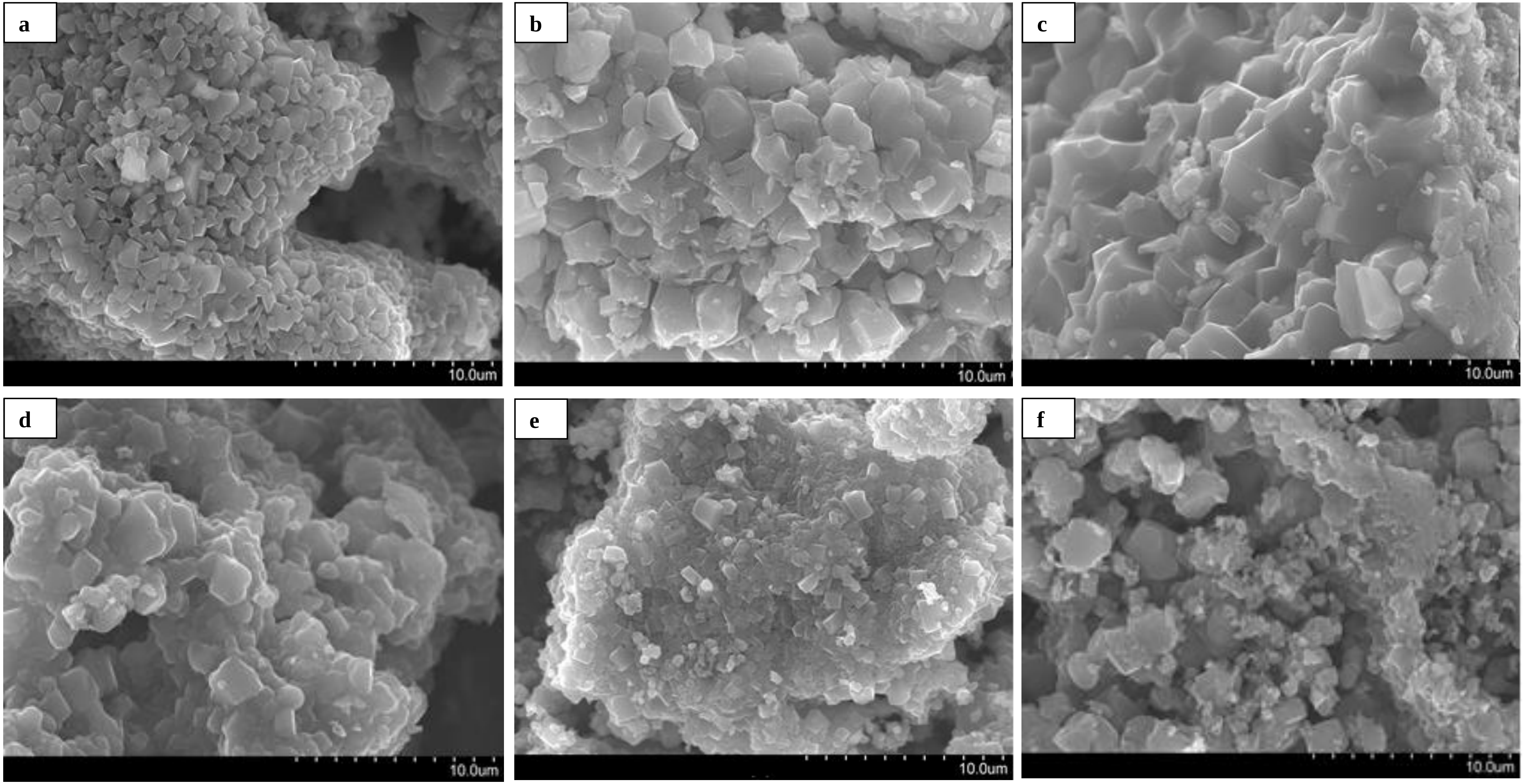

Fig. 23: SEM images of $LiNi_{0.6}Mn_{0.2}Co_{0.2}O_2$ annealed at 900°C/1h (a) 900°C/12h (b) 900°C/24h (c) and $LiNi_{1/3}Mn_{1/3}Co_{1/3}O_2$ annealed at 900°C/1h (d) 900°C/12h (e) 900°C/24h (f) prepared by self-combustion

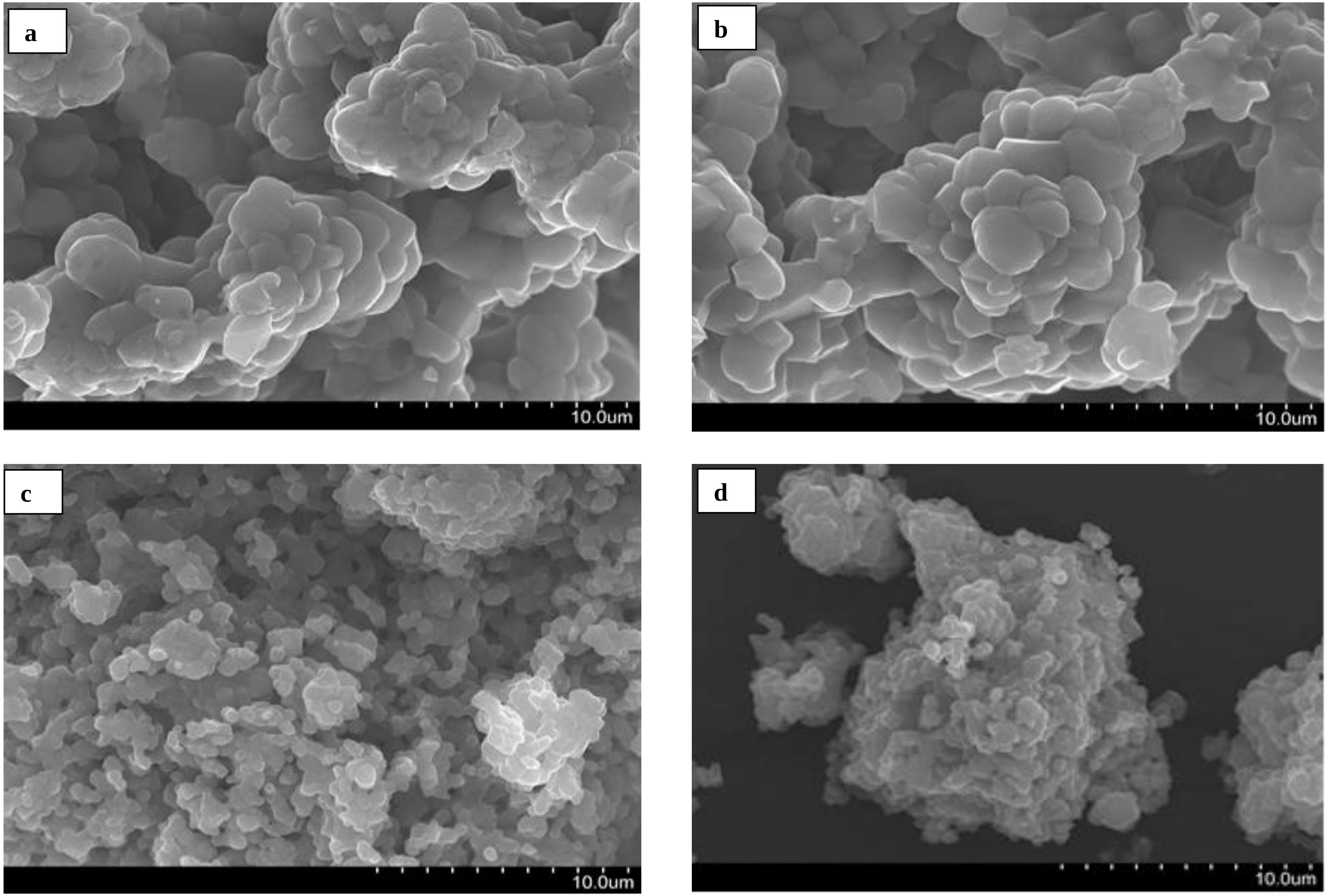

Fig. 24: SEM images of $LiNi_{0.6}Mn_{0.2}Co_{0.2}O_2$ annealed at 900°C/12h (a) 900°C/24h (b) and $LiNi_{1/3}Mn_{1/3}Co_{1/3}O_2$ annealed at 900°C/12h (c) 900°C/24h (d) prepared by co-precipitation

4. Annealing temperature

In order to demonstrate how the annealing temperature affects the structural and morphological properties we studied by XRD and SEM three NMC materials with the composition (3:1:1) prepared by self-combustion method. They were annealed for 1 h at 700°C, 800°C and 900°C. As shown in the diffractograms (figure 25) the phases crystallize in the rhombohedral system and all diffraction peaks can be indexed in the α-$NaFeO_2$ type structure (space group: $R\bar{3}m$). Also, the shape of the diffraction lines as well as their narrowness especially for the third compound indicates good crystallinity and homogenous distribution of the cations in the structure.

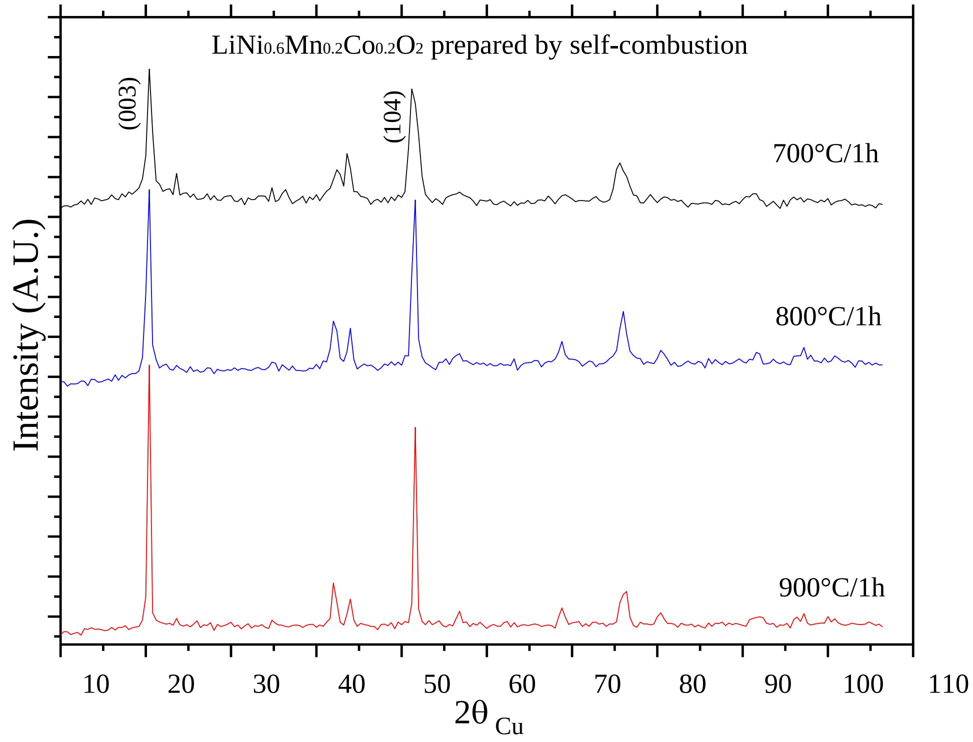

Fig. 25: Comparison between X-ray diffraction patterns of the material $LiNi_{0.6}Mn_{0.2}Co_{0.2}O_2$ annealed at 900°C, 800°C and 700°C during 1 h

.

The morphological characterization was conducted by SEM (figure 26). The sample annealed at 900°C consists of small aggregates of elementary particles with a size distribution in the range of 500-600 nm. While the two samples annealed at 700°C and 800°C respectively are characterized by aggregates of larger size in the order of 20 µm. The primary particles in this case are also in the micrometer range. The small size of the particles obtained by annealing at 900°C allows a rapid diffusion of lithium ions and leads to a large amount of lithium ions exchanged.

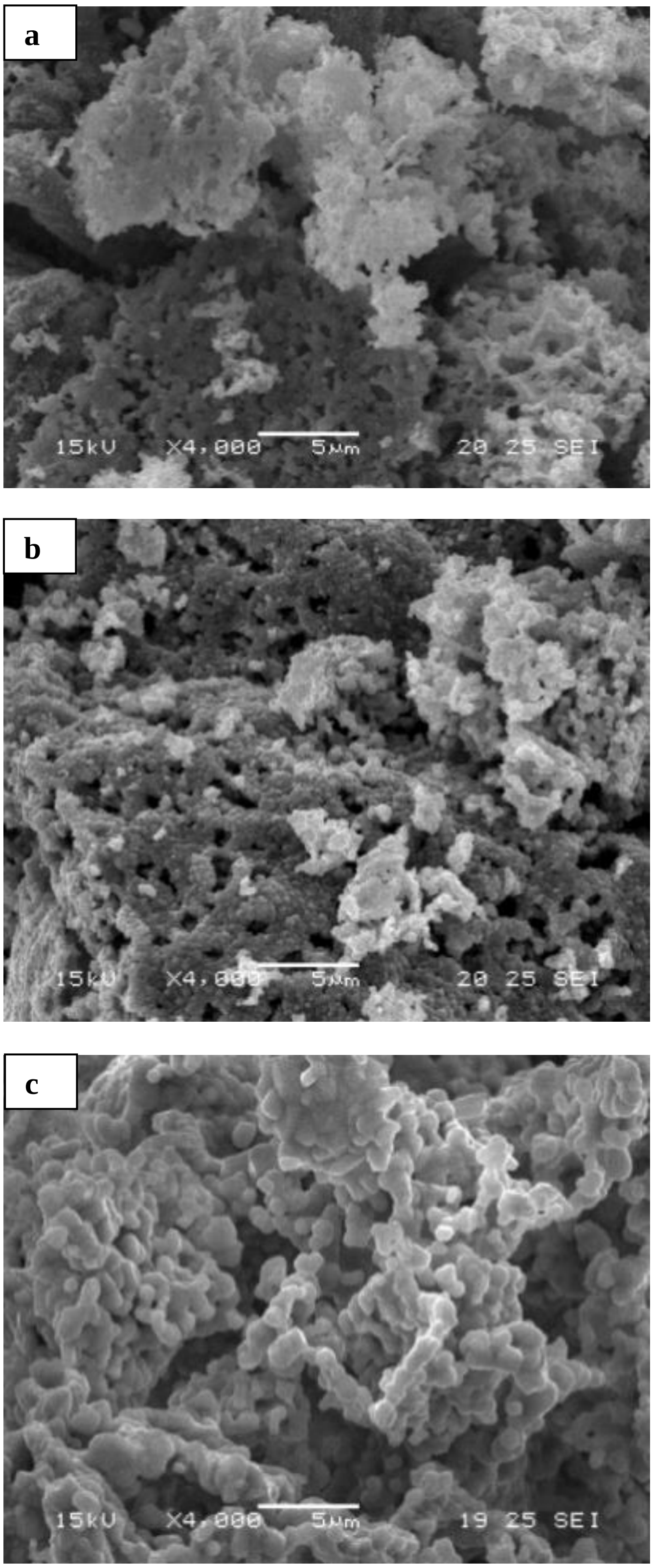

Fig. 26: SEM images of the material $LiNi_{0.6}Mn_{0.2}Co_{0.2}O_2$ annealed at 700°C/1h (a) 800°C/1h (b) and 900°C/1h (c)

5. Annealing atmosphere

In order to demonstrate the importance of the annealing atmosphere and assess how much air is needed to obtain NMC phases with crystalline structure, two NMC samples with the composition $LiNi_{0.6}Mn_{0.2}Co_{0.2}O_2$ prepared by self-combustion method were annealed during 12 h in air and argon, respectively. Structural and morphological analyses for both compounds were carried out by means of XRD and SEM.

From the XRD patterns (figure 27), it can be seen that the sample annealed under argon cannot be indexed in the space group R-3m as the most characteristic diffraction peaks of α-$NaFeO_2$ type structure are missing. Further analysis of the diffraction lines showed that the sample consists mainly of Li_2CO_3 that crystallizes in the monoclinic system and presents diffraction peaks in the 2θ region 21°-35°. Li_2CO_3 is in fact the result of reaction between lithium and carbon coming from sucrose used as fuel. In addition, diffraction peaks related to Ni, Co and Mn oxides are present.

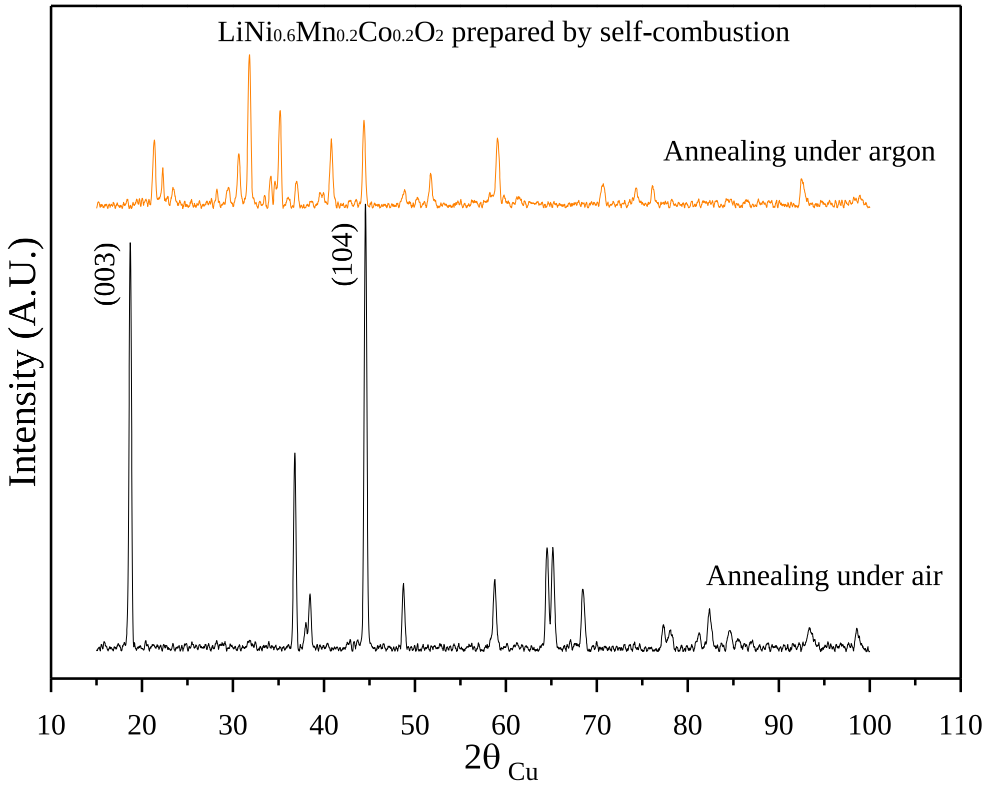

Fig. 27: X-ray diffraction patterns of the NMC (3:1:1) positive electrode materials annealed under air (black) and under argon (orange)

SEM was performed to check the morphology and particle sizes of the two phases (figure 28). We notice an evolution of the morphology from individual particles for the sample annealed under air to more non-uniform and undefined shape particles with bigger size for the phase annealed under argon.

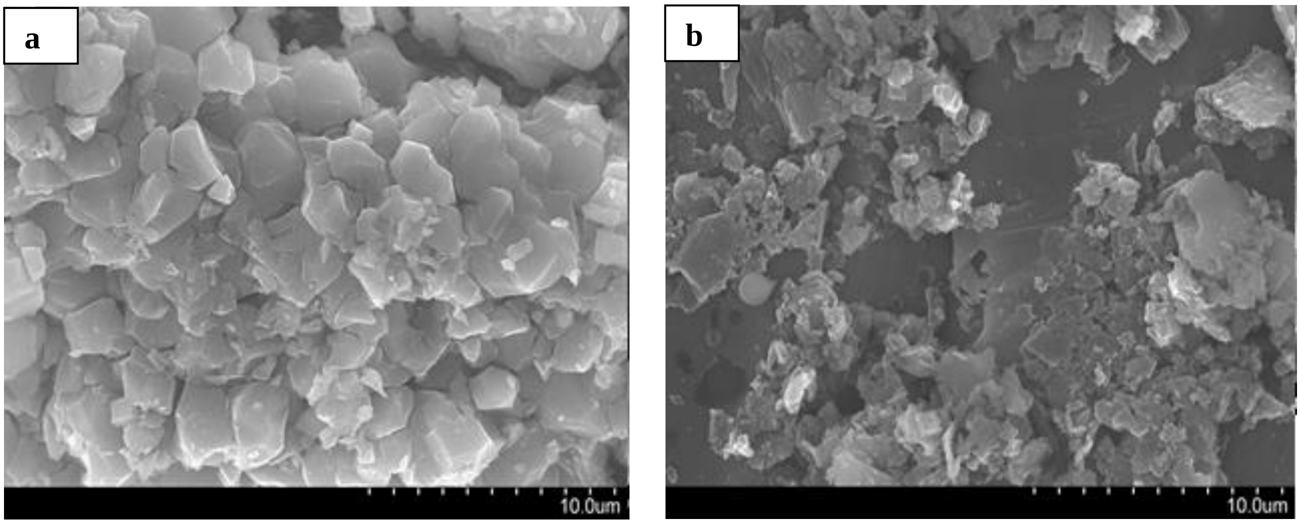

Fig. 28: SEM images of the sample NMC (3:1:1) annealed for 12h under air (a) and the one annealed for 12h under argon (b)

From the previous results, we were able to demonstrate the necessity of carrying out the annealing under air according to the reaction equation:

$$1.05\ LiNO_3 + 0.6\ Ni(NO_3)_2 + 0.2\ Co(NO_3)_2 + 0.2\ Mn(NO_3)_2 + 2/3\ C_{12}H_{22}O_{11} + \boxed{\mathbf{O_2}}$$

$$\Downarrow$$

$$Li\,Ni_{0.6}Mn_{0.2}Co_{0.2}O_2 + N_2 + NO_x + CO_2 + H_2O$$

6. Aging effect

In order to better understand how the time between synthesis and annealing affects the structural and morphological properties, we studied by XRD two NMC (3:1:1) samples. The first was annealed immediately after synthesis and the second was aged 6 months before annealing in air atmosphere (figure 29). From the XRD patterns, all diffraction peaks for both phases can be indexed in the α-$NaFeO_2$ type structure (space group: $R\bar{3}m$). The shape and narrowness of the diffraction lines show a good crystallinity. However, for the aged sample, we notice the presence of peaks related to Li_2CO_3.

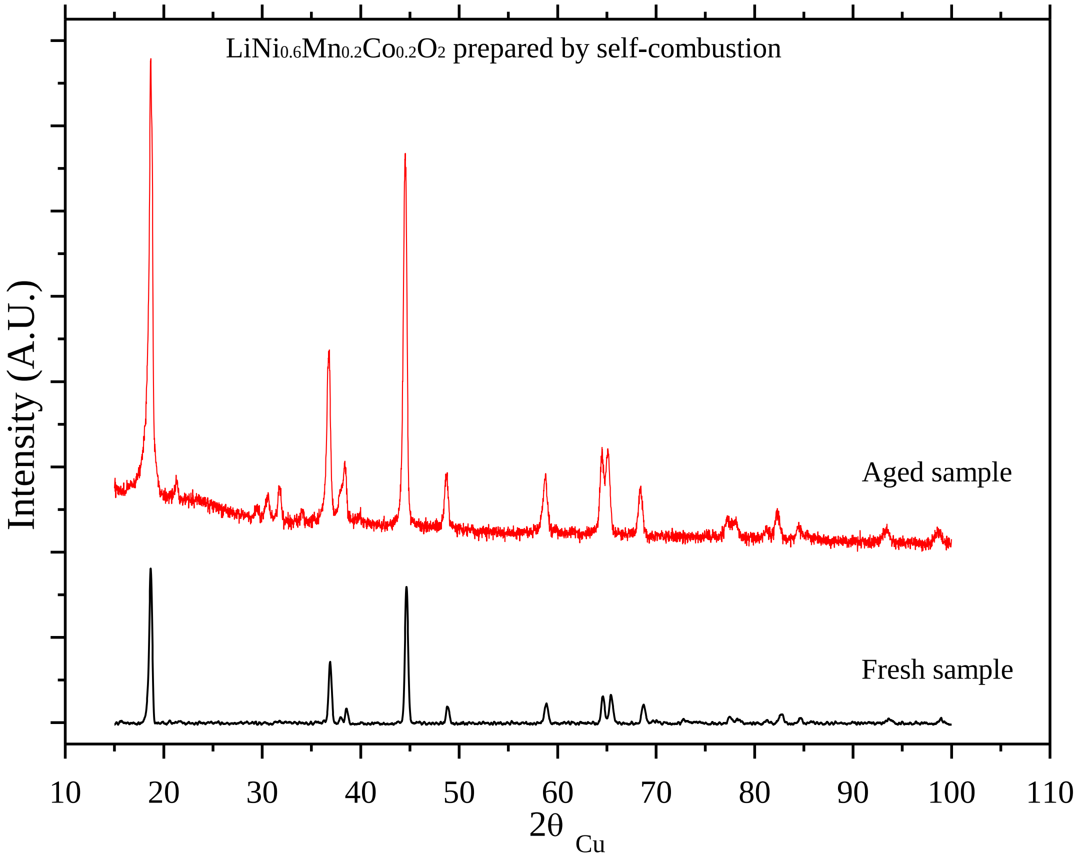

Fig. 29: X-ray diffraction patterns of the aged (red) and fresh NMC (3:1:1) positive electrode materials (black)

In order to evaluate in detail the deviation of the NMC lattice parameters between the fresh and aged samples, the XRD diffractograms were further analyzed by Rietveld refinement method. A good minimization function was obtained even for the aged material (figure 30).

Furthermore, the lattice parameter a, representing the metal–metal intra-sheet distance, slightly increased from 2.8608 Å for the fresh sample to 2.8660 Å for the aged sample. This can be attributed to the migration of some Ni^{2+} ions from the 3a sites to the interlayer 3b sites.

This phenomenon was confirmed by the decrease of the lattice parameter c, representing the interlayer space thickness, from 14.167Å for the fresh sample to 14.188Å for the aged one. Such decrease is mainly due to the stronger electrostatic attraction between oxygen and Li^{+}/Ni^{2+} ions in the interlayer space. Therefore, we can conclude that the occupancy of Ni^{2+} ions on Li^{+} ions sites is higher for the aged sample.

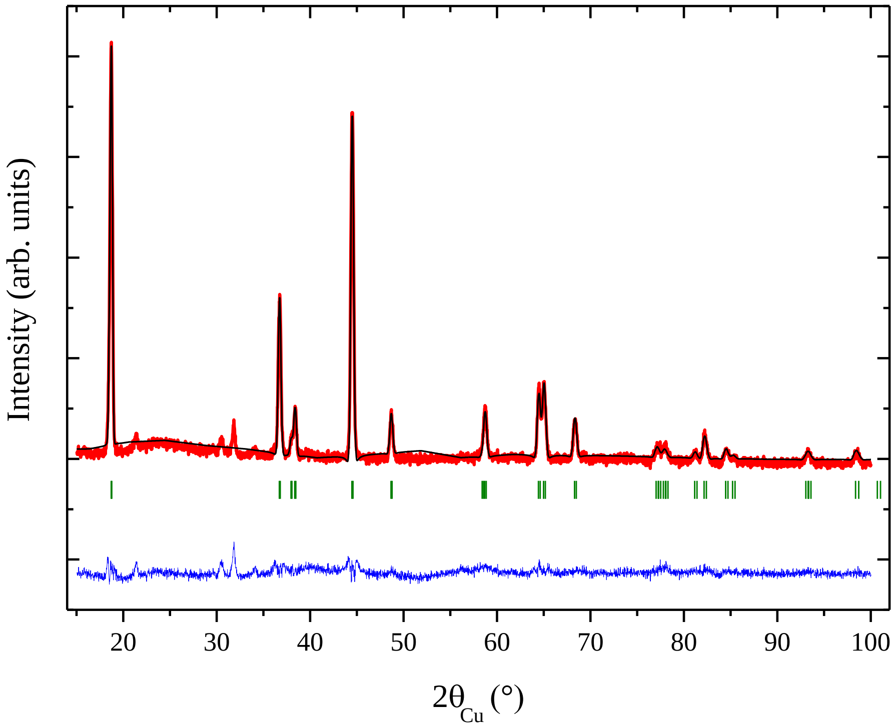

Fig. 30: Rietveld profile refinement results of the aged NMC electrode material: __ observed, __ calculated, __ difference, | Bragg positions

The morphological characterization was carried out by SEM (figure 31). For the fresh sample, the particles are smaller and their shapes are more defined while for the aged sample, the particle size increases and the shape is more fritted and less well-defined. Moreover, some fissures and cracks are present all over the particle surface of the aged sample.

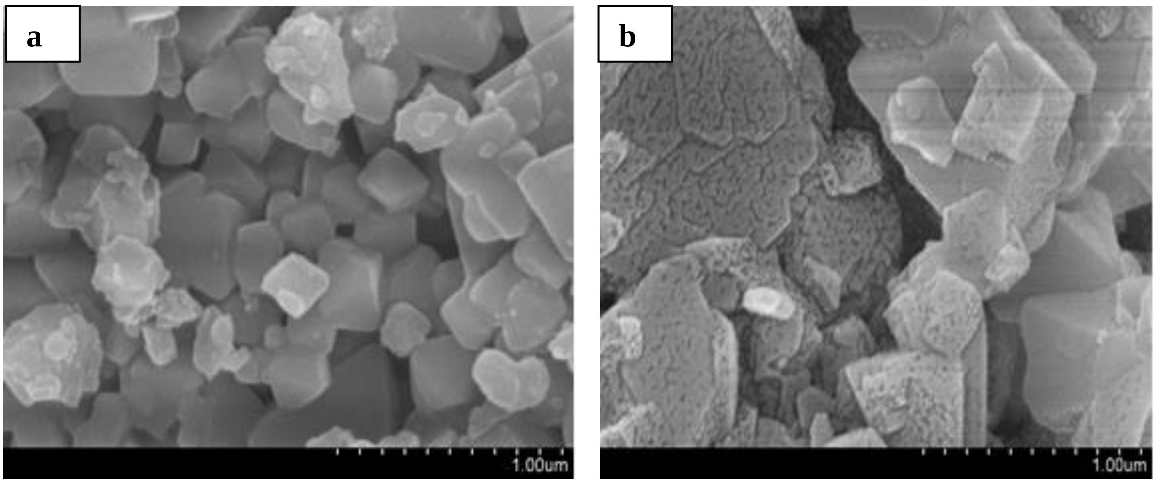

Fig. 31: SEM images of the fresh sample that was annealed immediately after synthesis (a) and the aged sample that was left in air for 6 months then was annealed (b)

The elemental analysis by EDX showed that the amount of oxygen is higher for the aged sample than for the fresh one (table 8). Likewise, the amounts of the carbon and nitrogen are much higher for the aged sample than for the fresh one. We can therefore understand that for an aged material, it is more difficult to extract oxygen, carbon and nitrogen oxides of the material through annealing.

Table 8: EDX element analysis of the fresh and aged samples

Element	**Wt. % (fresh sample)**	**Wt. % (aged sample)**
C	4.4 ± 0.6	7.9 ± 1.2
N	1.0 ± 0.2	7.4 ± 2.1
O	27.8 ± 1.4	31.6 ± 1.6
Mn	13.5 ± 1.6	11.5 ± 1.3
Co	13.7 ± 2.3	10.2 ± 2.1
Ni	39.8 ± 4.1	31.3 ± 3.7

In order to investigate the influence of the time between synthesis and annealing on the material's thermal properties, DTA-TG tests were performed (figure 32). The mass losses for both materials are mainly due to water, oxygen, carbon and nitrogen oxides release. The mass loss for the aged material is higher than for the fresh one. On the other hand, DTA curves show for both materials the presence of an exothermic peak related to the release of oxygen and carbon oxides, this peak is more pronounced for the aged material. This is probably due to the decomposition of Li_2CO_3 that is present in the case of aged NMC (3:1:1).

DTA-TG results confirm the EDX results that showed a higher amount of oxygen, carbon and nitrogen still present in the aged sample even after annealing. On the other hand, DTA curves present an endothermic peak for both materials; it is indicating the temperature from which we obtain the crystallized phase. This peak is almost the same for both materials.

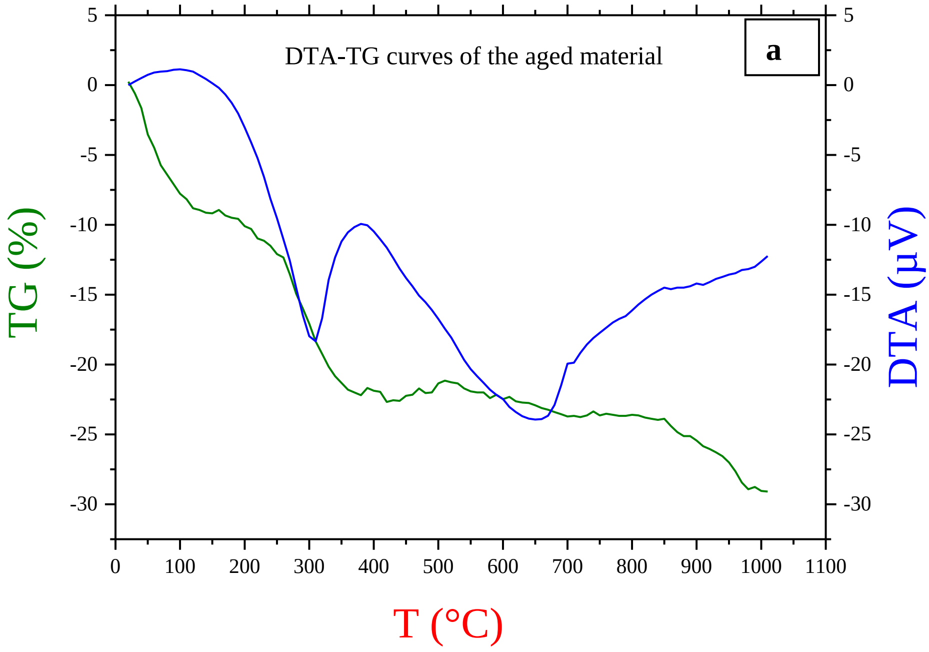

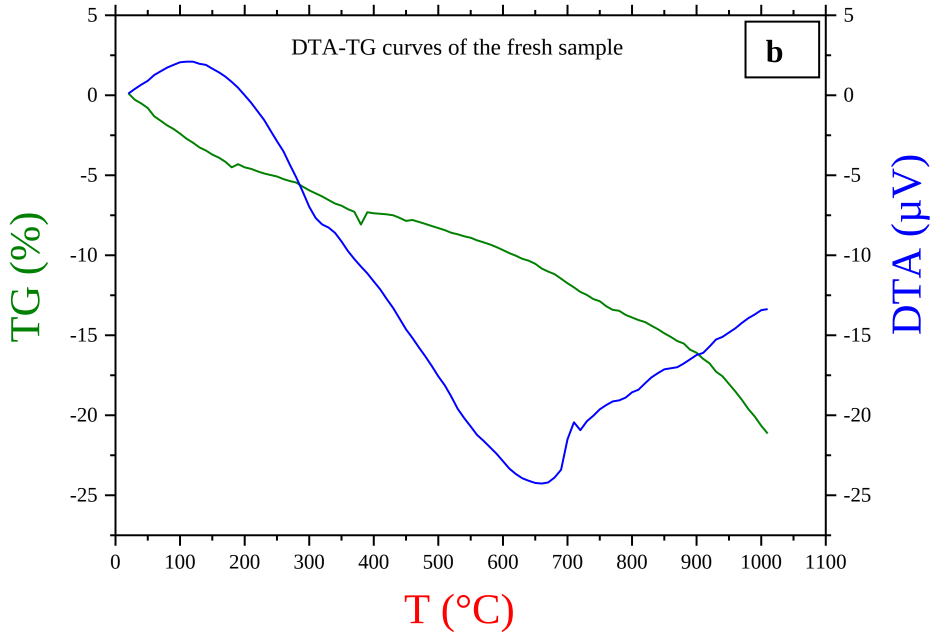

Fig. 32: DTA-TG curves of the aged sample that was left in air for 6 months then was annealed (a) and the fresh one that was annealed immediately after synthesis (b) DTA-TG tests were carried out simultaneously in the temperature range between 20 and 1020°C with a scan rate of 5°C/min

Cyclic voltammetry was performed for cells at room temperature with metallic lithium as counter and reference electrodes at a scan rate of 0.5 mV/s.

For the fresh sample, the first cycle anodic peak is related to the extraction of Li ions from the lattice, it occurs at 4.20 V, and the main cathodic peak is at 3.68 V and is related to the insertion of Li. The positions of oxidation and reduction peaks are very stable from one cycle to another, which indicates good reversibility of the charge–discharge reaction. However, the relative peak-intensities and the area under the peaks decrease slightly with cycle number. This is due to capacity fading phenomenon.

Regarding the aged sample, the cyclic voltammograms reported in figure 33 are showing a totally different behavior illustrated by the absence of cathodic and anodic peaks that correspond to the extraction and the insertion of lithium. This can be explained by a very low exchange of lithium ions caused by the high cation mixing in the aged sample´s structure.

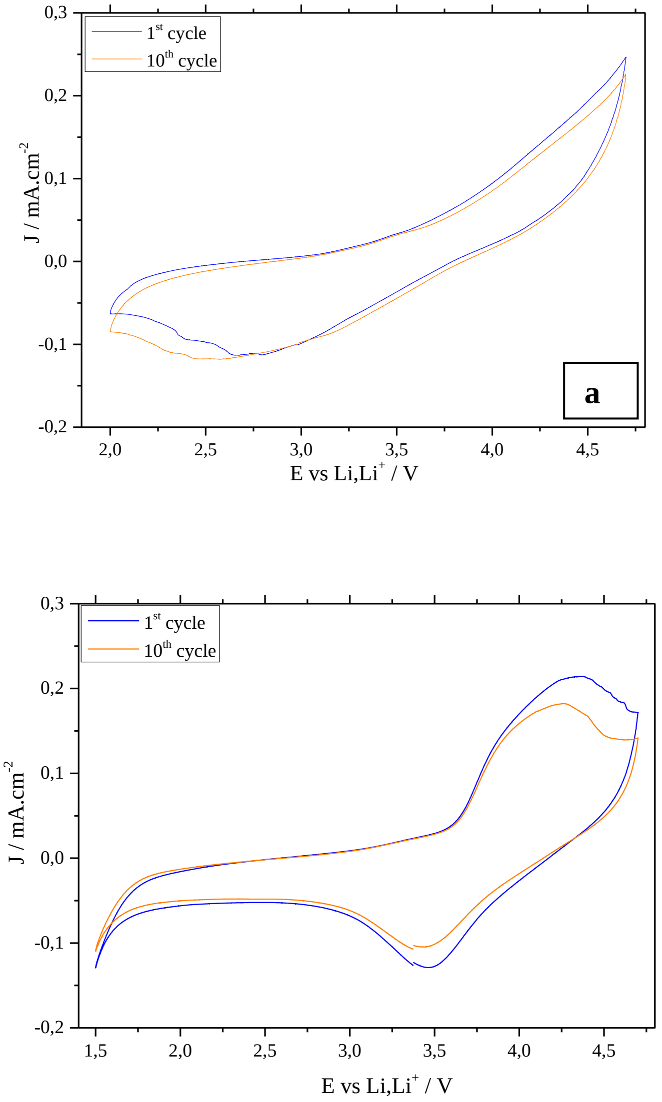

Fig. 33: Cyclic voltamorgamms of the aged (a) and fresh (b) samples vs. Li/Li+ at a scan rate of 0.5 mV/s. The fresh sample was annealed immediately after synthesis and the aged one was left in air for 6 months then was annealed

The electrochemical performance of the two NMC (3:1:1) samples was evaluated by galvanostatic cycling at slow rate C/20 (figure 34). For the fresh material, the similarity between the charge-discharge curves indicates a good reversibility of the Li^+ ion intercalation-deintercalation process. The reversible capacity obtained during the first cycle is of the order of 155 mAh g^{-1}. For the aged material, a similarity between the charge-discharge curves is also observed during the ten first cycles except the first cycle´s charge curve which is irreversible. However, the reversible capacity in the case of aged NMC (3:1:1) is very low (about 25 mAh g^{-1}). The differences in the particle size as well as morphology between the two samples can explain their electrochemical behavior. Indeed, the small size of the particles in the case of fresh NMC (3:1:1) sample allows a rapid diffusion of Li^+ ions and lead to an intense exchange of lithium ions and therefore to a larger reversible capacity. On the other hand, the increase of Ni^{2+} ions in the interlayer space, for the aged sample, results in cation mixing which hinders the efficient Li-ion transport and reduces significantly the reversible capacity.

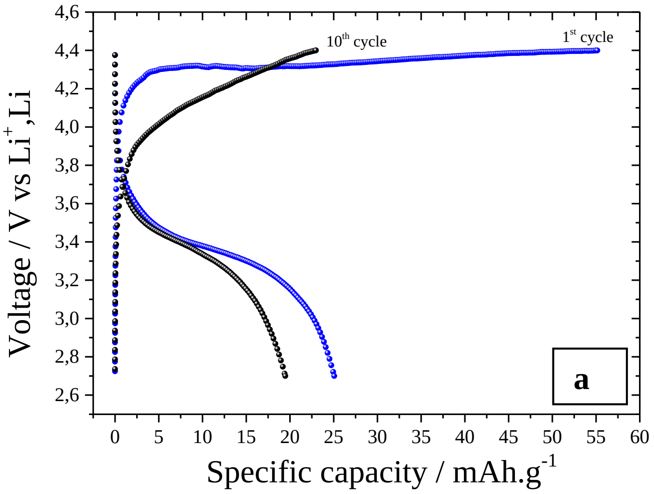

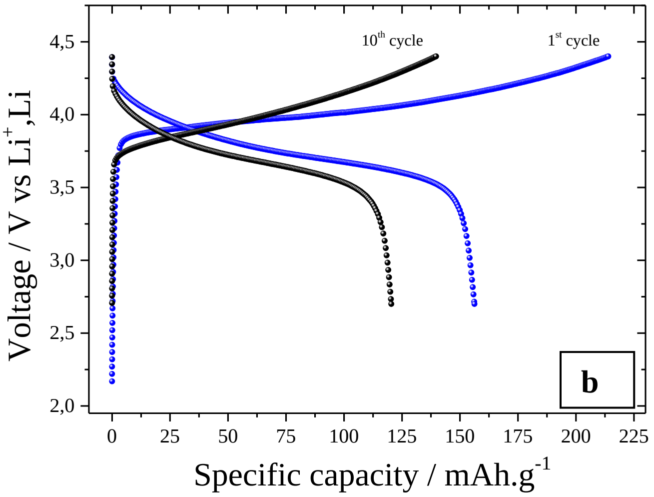

Fig. 34: Galvanostatic cycling at C/20 rate of the aged (a) and fresh (b) samples of the material $LiNi_{0.6}Mn_{0.2}Co_{0.2}O_2$

V. Characterization of the novel cathodes obtained by cationic substitution

1. Introduction

As it was evident through state of the art on NMC type materials and through the previous chapter, the synthesis conditions can have a great influence on the electrochemical performance of NMC type cathode materials.
According to the study that was conducted in chapter 3, we were able to fix for all of the following, the optimal conditions for the preparation of the investigated cathode materials throughout this work. Thereby, the phases were prepared by self-combustion synthesis method. They were annealed directly after synthesis in air at 900°C for one hour. The main phase was the nickel rich one with the composition (3: 1: 1)
In the following chapter, we chose to examine the influence of the cobalt substitution by aluminum and / or iron in an attempt to further optimize the starting material NMC (3:1:1). In the following, these materials are shortly called NMCA ($LiNi_{0.6}Mn_{0.2}Co_{0.15}Al_{0.05}O_2$), NMCF ($LiNi_{0.6}Mn_{0.2}Co_{0.15}Fe_{0.05}O_2$) and NMCAF ($LiNi_{0.6}Mn_{0.2}Co_{0.15}Al_{0.025} Fe_{0.025}O_2$).

2. Structural characterization

2.1. by XRD

X-ray diffraction diagrams of the four materials (fig. 35)show that all diffraction peaks can be indexed in the R-3m space group. According to the XRD data, the phase α-NaFeO2 type was obtained systematically pure for all of the aforementioned materials. Analysis of the continuous background has not detected any presence of the impurity Li_2CO_3.

The full width at half maximum (FWHM) values of the reflections (003) and (104) are reported in table 9. The smallest values of the FWHM of the reflections (003) and (104) were obtained for the double substituted phase NMCAF and they are respectively equal to 0.32° and 0.36°. This indicates better crystallinity obtained for the NMCAF material and suggests a homogeneous distribution of the cations in the structure. The FWHM of the (003) and (104) peaks are gradually increasing when moving from NMCF to NMCA and finally NMC. The latter presented the highest values: 0.43 for $FWHM_{(003)}$ and 0.42 for $FWHM_{(104)}$.

In contrast, the intensity ratio of the peaks (003)/(104) tends to decrease as the FWHM tends to increase. The broadening of the diffraction lines could indicate a reduction in crystallinity of the phases, whereas the evolution of the intensity ratio $I_{(003)}$ / $I_{(104)}$ may indicate an improvement in the structure. As reported in table 9, higher $I_{(003)}/I_{(104)}$ value was obtained for the double substituted material compared to the mono and non-substituted materials. This confirms the formation of more ordered lamellar phase for NMCAF material than for NMCF and NMCA and NMC.

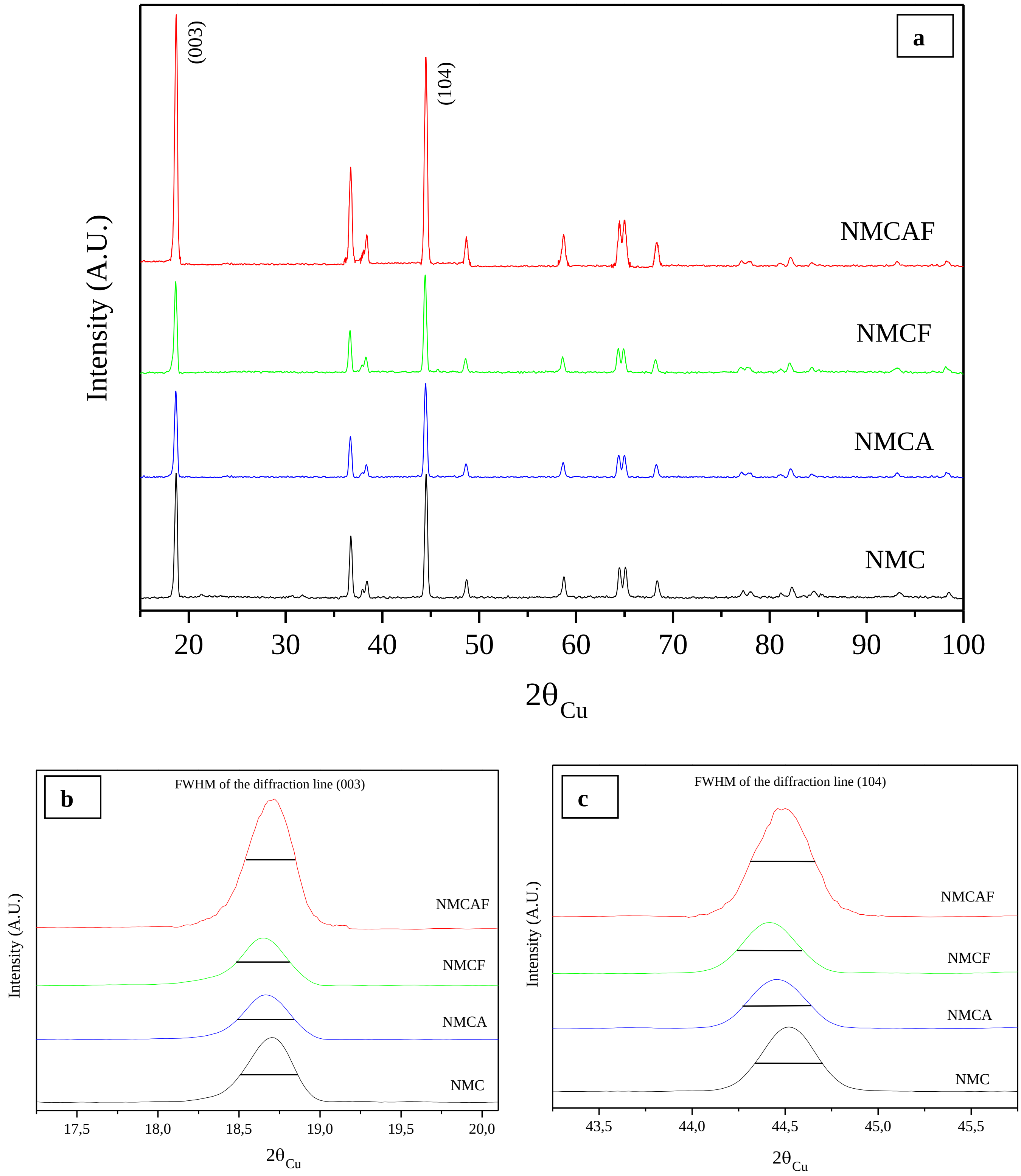

Fig. 35: Comparison between X-ray diffraction patterns of the four materials NMC, NMCA, NMCF and NMCAF (a) and the insets of their diffraction lines (003) (b) and (104) (c)

Table 9: Structural parameters of the four materials NMC, NMCA, NMCF and NMCAF obtained by XRD

Cathode materials	**FWHM$_{(003)}$**	**FWHM$_{(104)}$**	**$I_{(003)}/I_{(104)}$**
NMC	0.43°	0.42°	0.86°
NMCA	0.39°	0.41°	0.89°
NMCF	0.35°	0.40°	0.96°
NMCAF	0.32°	0.36°	1.19°

2.2. Structural refinement by Rietveld method

The X-ray diffraction patterns of the four materials studied in the previous section of this chapter were refined by Rietveld method using Fullprof software and considering the presence of a single phase α- $NaFeO_2$ type. For refinement, we have considered the presence of additional lithium ions on the 3a sites of the transition metals and a possible exchange between the lithium ions of the 3b sites and the divalent nickel ions of the 3a sites.

The cation distribution in $LiMO_2$ lamellar type structures is mainly due to the size difference between Li^+ and M^{n+} cations. Therefore, taking into account the size of the different cations only (r(Li^+) = 0.76Å, r(Ni^{2+}) = 0.69Å, r(Mn^{4+}) = 0.53Å, r(Co^{3+}) = 0.54Å, r(Al^{3+}) = 0.53Å, r(Fe^{3+}) = 0.64Å, r(Ni^{3+}) = 0.56Å), we assumed that aluminum and iron ions are preferentially expected to occupy the 3a sites of the transition metals.

Table 10 presents the cation distribution determined by Rietveld refinement for the four materials.

As an example, for the NMCAF material, XRD refinement by Rietveld has led to the following cationic distribution:

$\mathbf{(Li_{0.97}Ni_{0.03})_{3b}(Li^{overlithiation}_{0.01}Li_{0.03}Ni^{II}_{0.55}Ni^{III}_{0.02}Mn_{0.21}Co_{0.15}Al_{0.025}Fe_{0.025})_{3a}(O_2)_{6c}}$.

Table 10: Cation distribution determined by Rietveld refinement method of the XRD diagrams of the four materials NMC, NMCA, NMCF and NMCAF

Cathode materials	**3b sites (interlayer space)**		**3a sites (MO2 layers)**						
	Li^+	**Ni^{2+}**	**Li^+**	**Ni^{2+}**	**Ni^{3+}**	**Mn^{4+}**	**Co^{3+}**	**Al^{3+}**	**Fe^{3+}**
NMC	0.92	0.06	0.09	0.52	0.03	0.21	0.20	-	-
NMCA	0.95	0.04	0.06	0.54	0.02	0.20	0.15	0.050	-
NMCF	0.96	0.04	0.05	0.54	0.02	0.20	0.14	-	0.051
NMCAF	0.97	0.03	0.04	0.55	0.02	0.21	0.15	0.025	0.025

On the other hand, a good agreement was obtained between the experimental and calculated patterns and the difference (I_{obs}-I_{calc}) was well minimized for all of the four materials NMC, NMCA, NMCF and NMCAF.

Moreover, we can see from table 11 that there is a slight expansion of the lattice parameters a and c for the Fe substituted materials due to the larger radius of the Fe^{3+} ions (64.5 pm) compared to that of Co^{3+} ions (54.5 pm).

In contrast, the very similar ionic radii of Al^{3+} (53.5 pm) and Co^{3+} (54.5 pm) resulted in a negligible decrease of the lattice parameter a_{hex} with aluminum substitution. This result is in good agreement with literature [311, 312].

Besides, if we compare the occupancy of the Ni ions on the 3b crystallographic sites of the lattice, we notice that the smallest amount was obtained for the double substituted material suggesting less cation mixing in the structure, and then we could expect better cycling performance (Ch. V.5.2) due to the better lithium diffusion.

Table 11: Structural parameters determined by Rietveld refinement method of the XRD diagrams of the four materials NMC, NMCA, NMCF and NMCAF

Crystal data	**NMC**	**NMCA**	**NMCF**	**NMCAF**
a	2.861 Å	2.859 Å	2,869 Å	2,868 Å
c	14,167 Å	14,162 Å	14,215 Å	14,211 Å
V	100,56 $Å^3$	100,53 $Å^3$	101,34 $Å^3$	101,22 $Å^3$
Occupancy of Ni^{2+} on Li^+ sites	13 %	9 %	8 %	5%

3. Morphological characterization

3.1. by SEM

The primary particles of NMC, NMCA, NMCF and NMCAF have a relatively homogeneous size distribution (Fig. 36). The non-substituted material NMC presents larger primary particles (~ 450 nm average diameter) than those of the substituted materials.

Regarding the aluminum substituted material, the particle size ranges between 350 nm and 500 nm. This size reduction of the primary particles was also observed by Hu et al. [312]. Besides, by comparing SEM micrographs obtained for the two iron substituted materials NMCF and NMCAF and the pristine non-substituted material NMC, it is noticeable that for the Fe substituted compounds the spherical shape of the particles is more uniform and their sizes are smaller ranging between ~ 280 nm and 500 nm. Similar results have been reported in the literature by Li et al. [36]. Substituted materials especially with iron also exhibit rather airy and less compact powders, unlike substituted NMC material for which the agglomerates appear more sintered.

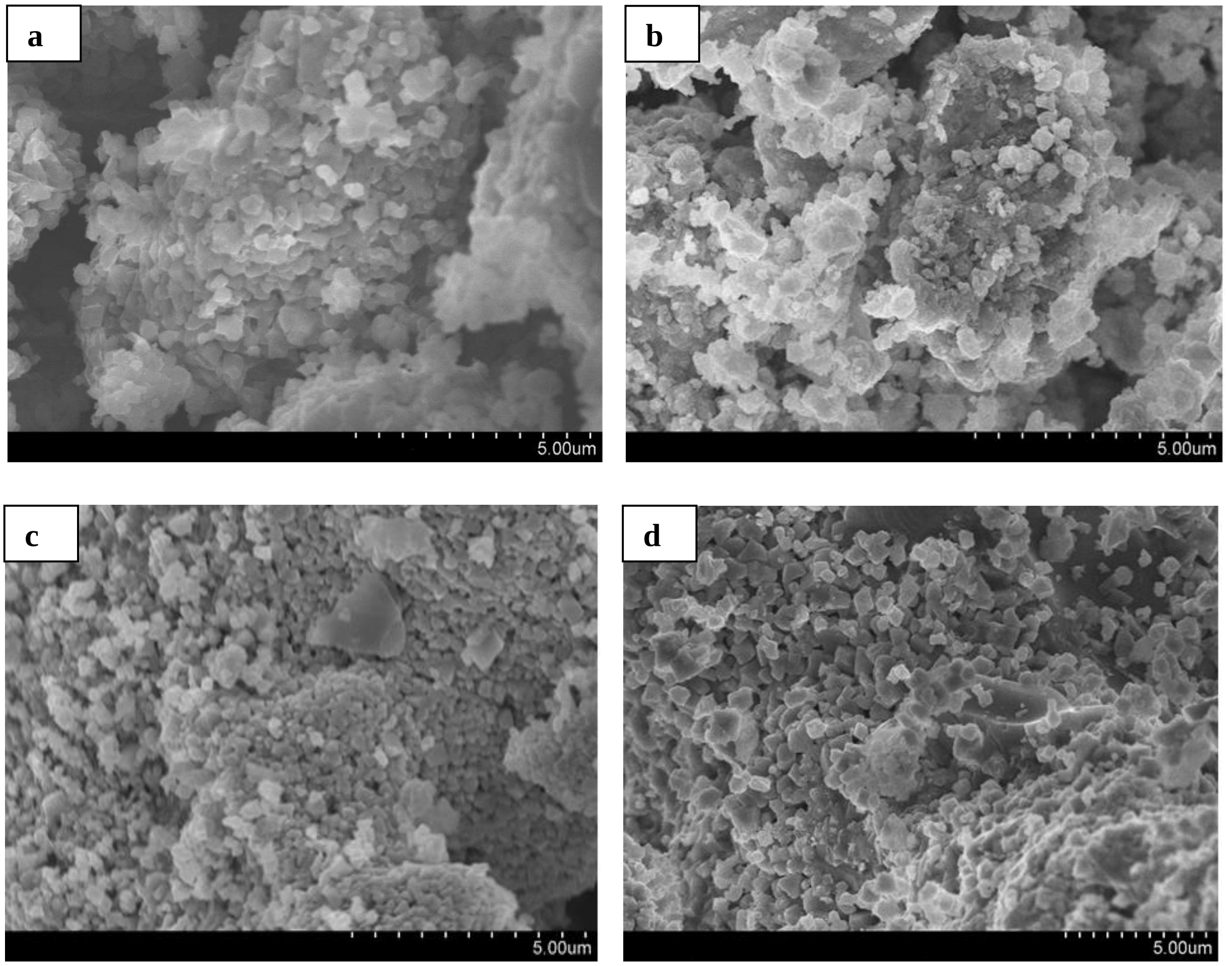

Fig. 36: SEM images of the four materials NMC (a), NMCA (b), NMCF (c) and NMCAF (d)

3.2. Specific surface measurement by BET

Table 12 reports the values of specific surface measured by BET method (Ch. III.2.2) for the four samples NMC, NMCA, NMCF and NMCAF. The highest specific surface has been obtained for the double substituted material NMCAF, while the lowest one was achieved for the pristine non-substituted NMC material. BET results confirmed to be in good agreement with the SEM analysis.

Table 12: Comparison of specific surface measured by the BET. method for the four phases NMC, NMCA, NMCF and NMCAF

Cathode materials	**$S_{B.E.T.}$ (m^2/g)**
NMC	4.02 ± 0.03
NMCA	4.08 ± 0.13
NMCF	4.18 ± 0.19
NMCAF	4.21 ± 0.08

The noticeable differences in the particle size between the four materials as well as in the specific surfaces can provide insight on their electrochemical behavior. Indeed, the small particle size observed for the double substituted material NMCAF will allow a rapid diffusion of lithium ions and therefore will lead to a significant amount of exchanged lithium ions and a greater reversible capacity, whereas the large particles observed for the pristine NMC material seem likely to prevent their impregnation by the electrolyte and may thus provide weaker electrochemical performance.

4. Thermal characterization by DTA-TG

DTA-TGA tests were carried out in the temperature range T = [20°C; 1020°C] with a heating temperature rate equal to 5°C/min for the four as-prepared cathode materials NMC, NMCA, NMCF and NMCAF (figure 37).

TGA curves show that the mass loss for the four compounds is produced during all the thermal treatment, which is mainly due to water, oxygen, carbon and nitrogen oxides release. The mass loss is smaller for the two iron substituted materials NMCF and NMCAF.

On the other hand, DTA curves show for the three materials the presence of an exothermic peak related mainly to the release of oxygen. An endothermic peak is also present for the four materials and indicates the crystallization temperature. This peak is at the same value (~ 725°C) for the four materials.

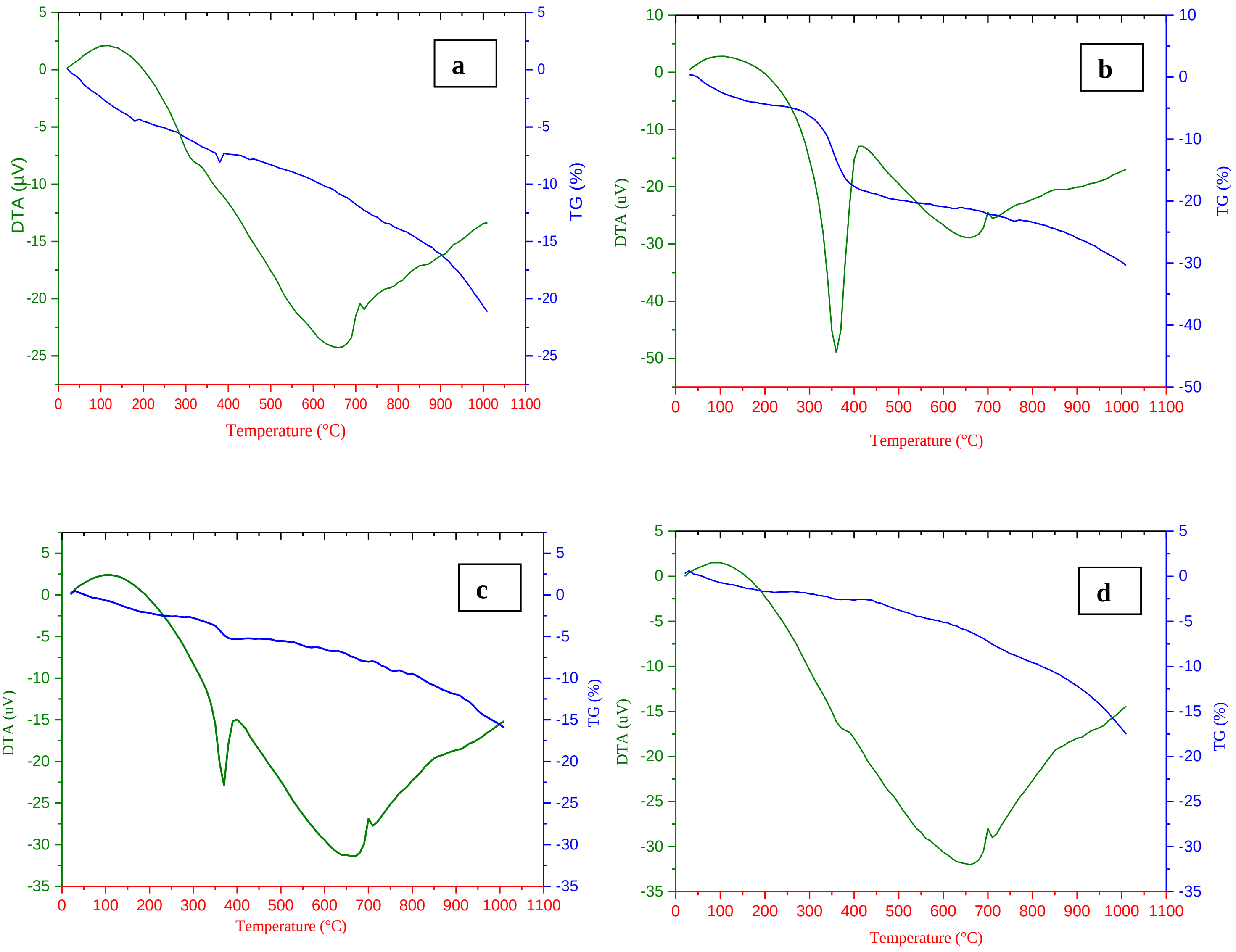

Fig. 37: DTA and TGA curves of NMC (a), NMCA (b), NMCF (c) and NMCAF (d) performed in air from room temperature to 1020 °C with a heating temperature rate of 5 °C / min

5. Electrochemical performance

5.1. Cyclic voltammetry

The cyclic voltammograms were recorded for cells at room temperature with metallic lithium as the counter and reference electrodes at a slow scan rate 0.1 mV/s. The voltammetric behavior of the metal substituted and non-substituted materials display approximately identical features (Fig. 38).

For NMCA, the first cycle anodic peak corresponding to the extraction of Li ions from the lattice occurs at 4.20 V vs. Li/Li$^+$, whereas the main cathodic peak (insertion of Li) is at 3.68 V vs. Li/Li$^+$. The difference between anodic and cathodic peak voltages remains almost constant, which indicates good reversibility of the charge–discharge reaction. The relative peak intensities and the area under the peaks slightly decrease with cycling. This indicates a capacity fading for the aluminum substituted material throughout cycling.

An identical behavior was observed for the iron substituted material NMCF regarding the main anodic and cathodic peak values. A good reversibility of the charge–discharge process is also noticeable. Regarding the double substituted material NMCAF, the extraction of Li ions from the lattice occurs already at 3.60 V vs. Li/Li$^+$, and the insertion of Li ions is taking place at about 3.35 V vs. Li/Li$^+$. NMCAF cathode material also presents a good reversibility of the charge–discharge reaction and with less capacity fading.

The oxidation and reduction peaks positions remain at constant potential with the cycle number for all the four materials. This indicates their good stability during voltammetric cycling.

The potential range that was used for the four materials lies between 1.5 V and 4.7 V. Even though this potential window is greater than that required for this type of materials, it remains suitable for the used electrolyte (Ch. III.4) since its stability window is located in this range. The aim through operating at such wider potential window was to specify the potential range that enables avoiding any side redox reaction of the active species in the material and any activation of the electrochemically inactive ions such as cobalt and iron ions especially when the potential is higher than 4.4 V. In the following, the potential window that was used is the one highlighted in figures 38 (a), (b), (c) and (d), ranging between 2.7 V and 4.4 V.

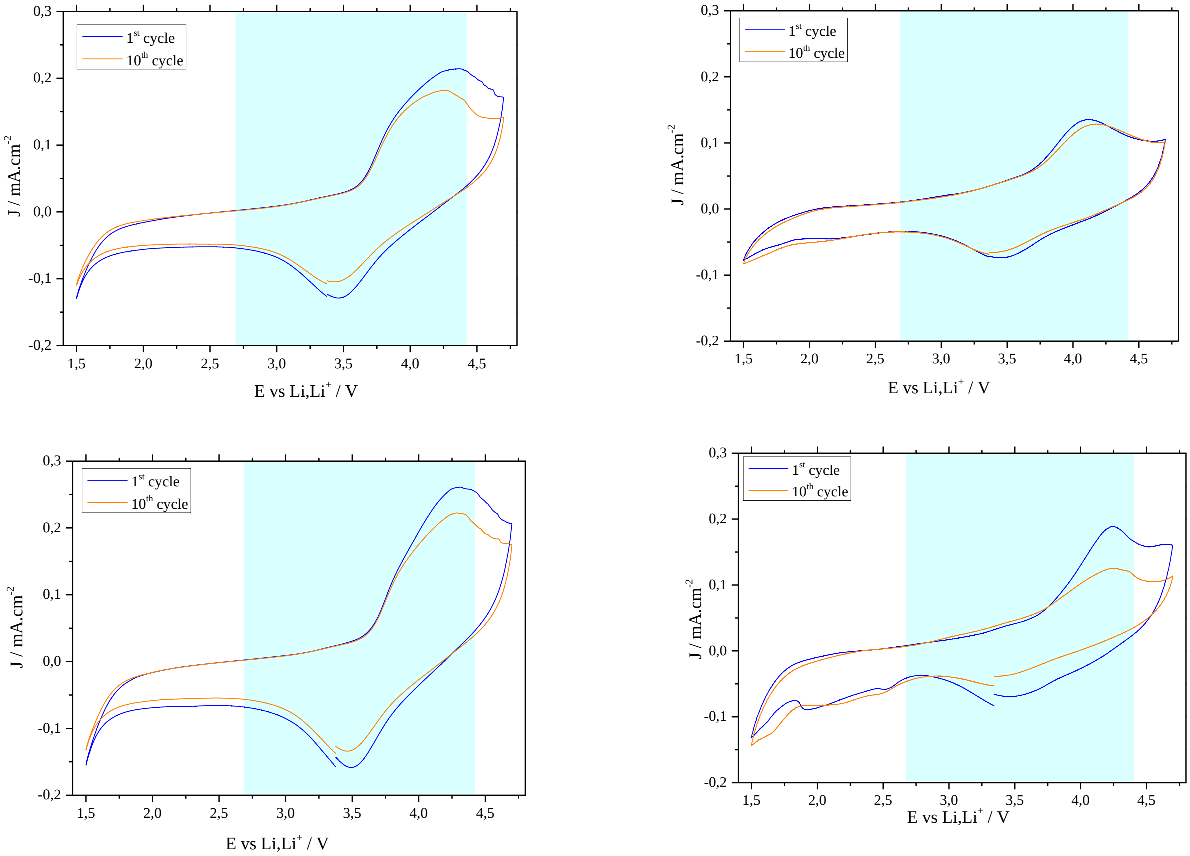

Fig. 38: Cyclic voltammetry curves I = f(V) of the four materials NMC (a), NMCA (b), NMCF (c) and NMCAF (d) of the 1st and 10th cycles at 0.1 mV/s scan rate

5.2. Galvanostatic cycling at different C rates

The electrochemical behavior of the four electrodes NMC, NMCA, NMCF and NMCAF was studied at room temperature by galvanostatic cycling applying different C rates: C/20, C/5 and 1C.
Figure 39 shows the variation of the potential with the specific capacity at slow rate C/20. A continuous and similar evolution of the potential with the time can be perceived for all four materials. The shape of the charge-discharge curves shows then a good reversibility of the intercalation-deintercalation process. Therefore, a partial substitution of the cobalt by an amount of aluminum and / or iron limited to 1/20 in the layered oxide is accompanied by an improvement in the reversible capacity compared to the non-substituted material. NMC (3:1:1) in addition to a remarkable reduction in the irreversible capacity. This can be explained by the presence of less Ni^{2+} ions in the interlayer space for the substituted materials especially NMCAF.

From Figure 39, one can easily note that the initial discharge capacity for the double substituted electrode is of the order of 190 mAh/g, higher than those of the mono substituted electrodes with Fe (165 mAh/g) or Al (162 mAh/g) and the non-substituted NMC electrode (156 mAh/g). However, small changes in plateau potentials are observed after the metal substitution. The voltage plateau at ca. 3.75 V for the four studied NMC type materials can be attributed to Ni^{2+}/Ni^{4+} reaction.

The plateau potential variations for the studied materials can be related to the drop of the chemical potential in case of Al substituted materials and to a polarization effect for the Fe substituted materials. The effect of voltage change is in a good correlation with the change of the structural parameters after the substitution, since a very small amount of substitution caused a big difference in terms of cation mixing.

The evolution of the discharge capacity as a function of the cycle number obtained at faster rates C/5 and 1C for the four materials over the first 50 cycles is shown in Figure 40. The cycling stability was also improved for the substituted materials especially NMCAF in the used cycling conditions. Table 13 is a summary of the most significant values obtained for the four materials. Indeed, at the C/5 rate for instance, the non-substituted material exhibited a continuous decrease in its reversible capacity with a loss of about 26% after 50 cycles, whereas the double substituted material, for example, lost less than 15% of its reversible capacity at the end of the test. Better stability of the capacity during cycling is obtained for the NMCAF material followed by NMCF and NMCA with capacity retention of the order of 85.7%, 75.8% and 75.1% respectively, after 50 cycles.

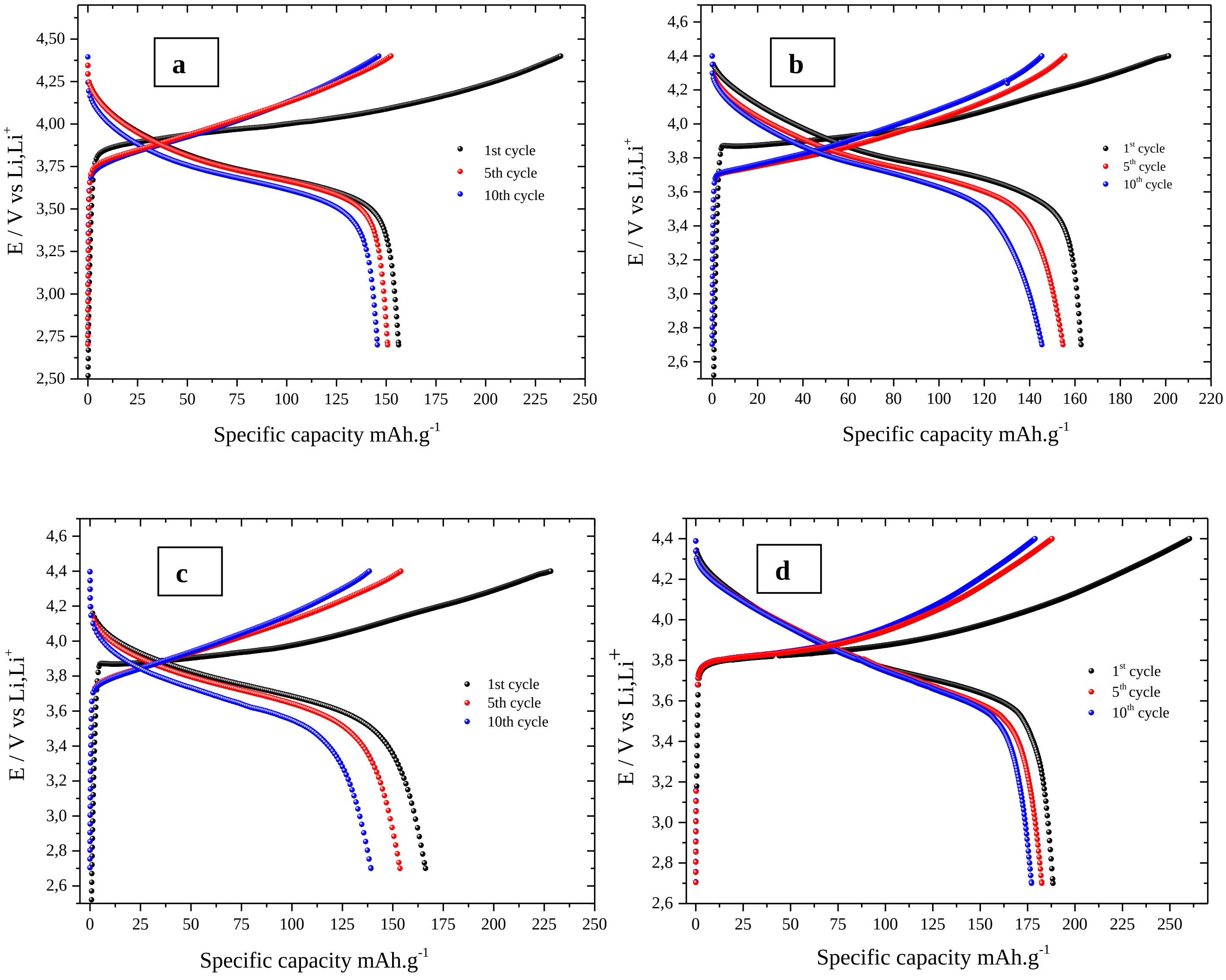

Fig. 39: Charge/discharge curves of the battery Li//EC:DMC//cathode material: NMC (a), NMCA (b), NMCF (c) and NMCAF (d) during the 10 first cycles under C/20 rate

.

Table 13: Electrochemical parameters obtained for the four materials NMC, NMCA, NMCF and NMCAF at C/20, C/5 and 1C rates

Samples	**Irreversible capacity (C/20 rate)**	**Rev. capacity 1st cycle (C/20 rate)**	**Rev. capacity 10th cycle (C/20 rate)**	**Capacity retention after 10 cycles (C/20 rate)**	**Capacity retention after 50 cycles (C/5 rate)**	**Capacity retention after 50 cycles (1C rate)**
NMC	81 mAh/g	156 mAh/g	138 mAh/g	88.4 %	74.7 %	73.5 %
NMCA	60 mAh/g	162 mAh/g	144 mAh/g	88.8 %	75.1 %	78.8 %
NMCF	62 mAh/g	165 mAh/g	147 mAh/g	89.1 %	75.8 %	71.7 %
NMCAF	70 mAh/g	190 mAh/g	176 mAh/g	92.6 %	85.7 %	78.5 %

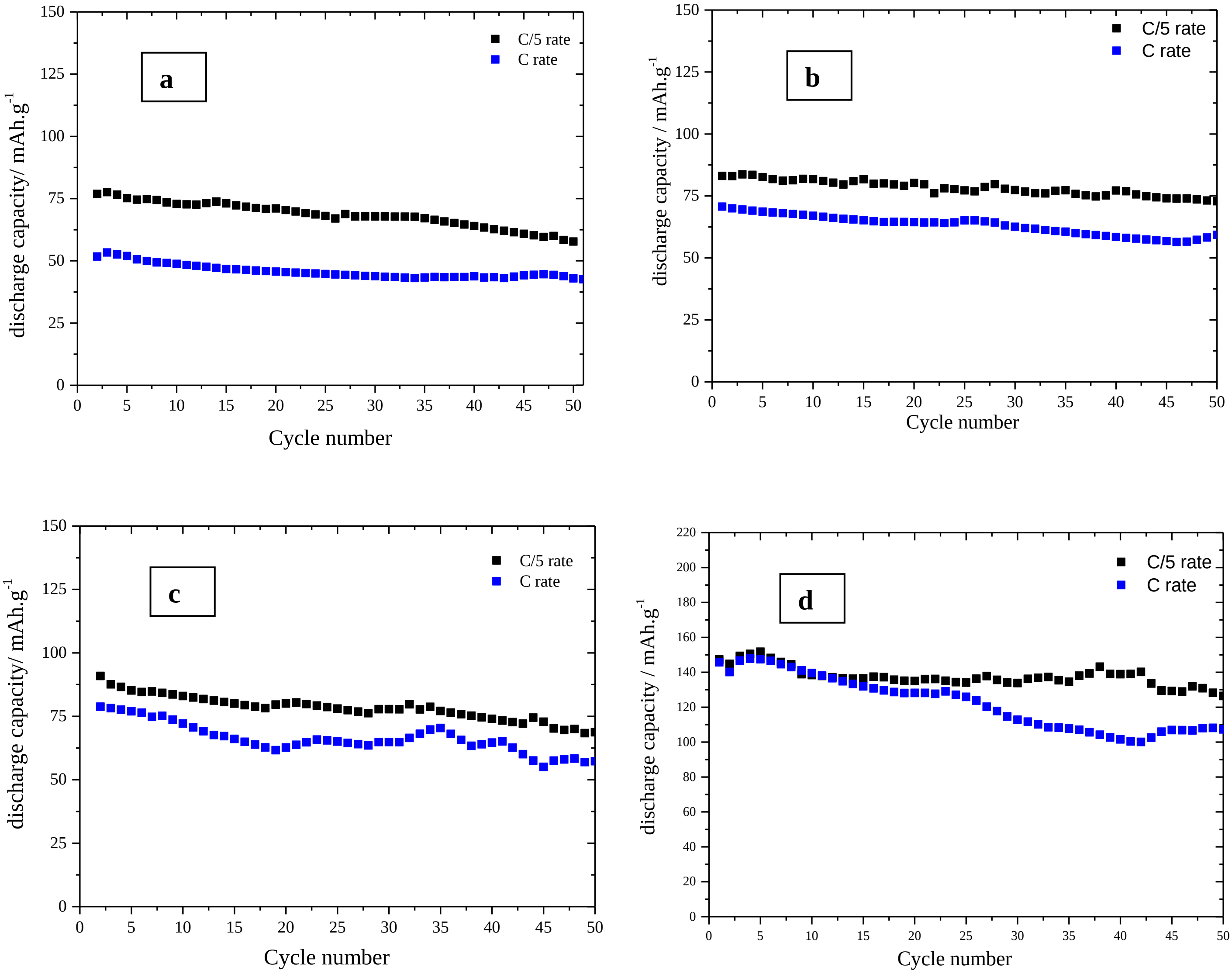

Fig. 40: Discharge capacity evolution with the cycle number of the materials NMC (a), NMCA (b), NMCF (c) and NMCAF (d) during the 50 first cycles under C/5 and 1C rates

.

VI. Synthesis and characterization of the double substituted cathode material $LiNi_{0.6}Mn_{0.2}Co_{0.15}Al_{0.025}Fe_{0.025}O_2$

1. Introduction

As shown in the previous chapter, metal substitution increases the order in the structure inducing a considerable structural stabilization, less cation mixing and strong electrochemical performance improvement by providing possibility for easier and more efficient Li intercalation.

According to the preliminary studies discussed in the previous chapter, the double substituted material NMCAF presented higher reversible capacities and better capacity retention compared to the pristine NMC(3:1:1) and to the mono-substituted materials (Ch. V.5.2). However, the link between its improved electrochemical performance and its structural propertieshas not been established in detail. In order to make this connection, extensive structural and electrochemical studies were carried out and correlated.

On the other hand, given the great concern attributed to safety aspects of active electrode materials for LIBs [314-317], the investigation of the temperature effect on the structural stability is of great importance since the thermal stability of the cathode materials is crucial for the safety.

Thereby, it was necessary to investigate the thermal and structural properties of the chemically de-intercalated phases of both NMCAF and NMC (3:1:1).

2. Synthesis by self-combustion

The preparation of the NMC (3:1:1) and NMCAF cathode materials was made by self-combustion synthesis method (Ch. VI.2.2).

Afterwards, to obtain better distribution of the particles and improved homogeneity, the synthesized phases were grinded by ball milling. An amount of 30g of active material was required. The milling speed was about 600 rounds/min for a period of time equal to 6 minutes consisting of two minutes milling followed by one minute rest to avoid the heating effect caused by the high milling speed. This procedure is repeated 3 times and each time the milling is in the opposite direction of the previous.

The difference between the NMC (3:1:1) material, for instance, before and after ball milling can be seen in Fig. 41. It is clear that no more aggregates exist after ball milling and the particles are more individual.

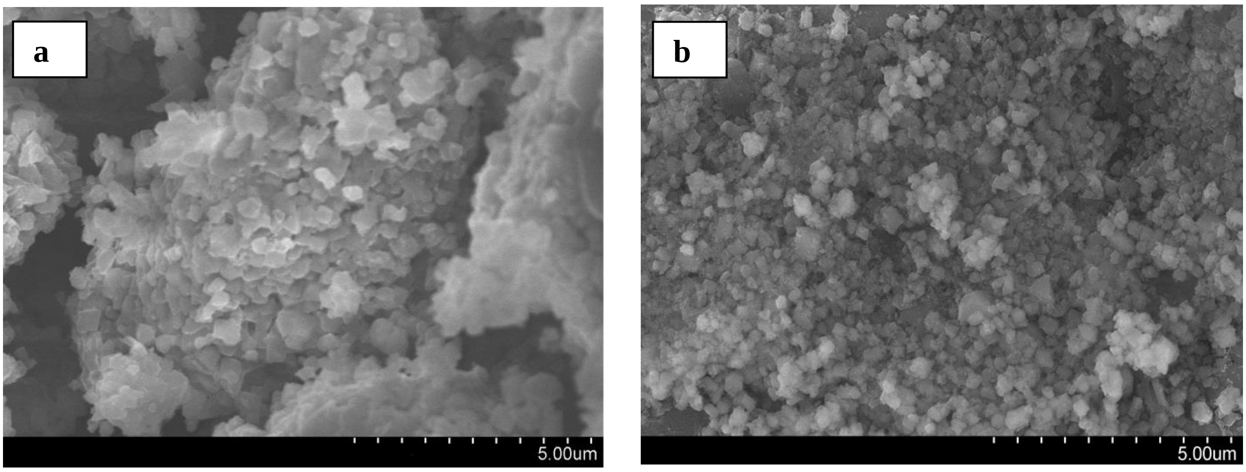

Fig. 41: SEM images of the NMC (3:1:1) material before ball milling (a) and after ball milling (b); The ball milling speed was about 600 rounds/min for a total milling time of 6 minutes

.

3. Structural characterization by XRD

In order to determine precisely the structural parameters of the studied phases, structural refinement by Rietveld method using Fullprof software has been performed.

First, the two samples NMC (3:1:1) and NMCAF are considered to crystallize in the ideal α-$NaFeO_2$ like structure. In this structure, and as has been confirmed in chapter 4, lithium and the transition metals occupy respectively the 3b (0, 0, ½) and 3a (0, 0, 0) crystallographic sites of the R-3m space group while oxygen occupies the 6c (0, 0, $z_{ox.}$) sites.

The occupancy of lithium, oxygen and transition metal cations was initially fixed to the experimental values. The zero offset, the lattice parameters, the scale factor, the parameters of the pseudo-Voigt type profile function and the isotropic atomic displacement parameters of the different atoms were refined.
The refined occupancy values showed no big difference compared to the experimental ones (the deviation is less than 8%), which indicates that we succeeded in synthesizing a stoichiometric phase.
The value obtained for the isotropic atomic displacement parameter related to the 3b lithium sites (B_{iso} (Li)) is positive (tables 14 and 15), indicating that no lithium excess was detected and almost all of the lithium is located in the interlayer space which shows the validity of the considered structural model.

A good agreement between the experimental and calculated XRD patterns was obtained as illustrated in Fig. 42 which gives a comparison between the observed and calculated diagrams of both NMC (3:1:1) and NMCAF materials. Indeed, a good minimization of the difference (I_{obs}. - $I_{calc.}$) and low values of the reliability factors of the order of (R_{wp} = 12.9 % and R_B = 4.7%) for the NMC (3:1:1) material and (R_{wp} = .8.1 % and R_B = 3.9 %) for NMCAF material were obtained. This suggests the good quality of refinement and further confirms the validity of the considered structural model.

Table 14: The main parameters deduced from the XRD data refinement as well as the cationic distribution of the material NMC (3:1:1)

$LiNi_{0.6}Mn_{0.2}Co_{0.2}O_2$

Space group: R-3m	n (Co) = 0.2 ; n(Mn)=0.2
$a_{hex.}$ = 2.861 Å	$n(Ni)_{3a} + n(Ni)_{3b} = 0.6$
$c_{hex.}$ = 14.167 Å	$n(Ni)_{3b} + n(Li)_{3b} = 1$

Atom	**Site**	**Wyckoff positions**			**Occupancy**	**B_{iso}(Å^2)**
Li (1)	3a	0	0	0.00	0.08	1.83
Ni (1)	3a	0	0	0.00	0.52	1.83
Li (2)	3b	0	0	0.50	0.92	1.61
Ni (2)	3b	0	0	0.50	0.08	1.61
Co	3a	0	0	0.00	0.20	1.83
Mn	3a	0	0	0.00	0.20	1.83
O	6c	0	0	0.26	2.00	0.63

Experimental conditions

Temperature	~ 298° K
2θ range	15° ≤ 2θ ≤ 100°
2θ step	0.02°
Zero point	0.008
Number of the refined parameters	16

Half-width parameters: U = 0.094; V = -0.031; W = 0.112

Reliability factors: R_{wp}= 12.9 % et R_B = 4.7 %

Table 15: The main parameters deduced from the XRD data refinement as well as the cationic distribution of the material NMCAF

$LiNi_{0.6}Mn_{0.2}Co_{0.15}Al_{0.025}Fe_{0.025}O_2$

Space group: R-3m	n (Co) = 0.2 ; n(Mn)=0.2
$a_{hex.}$ = 2.868 Å	n $(Ni)_{3a}$+ n $(Ni)_{3b}$ = 0.6
$c_{hex.}$ = 14.211 Å	n $(Ni)_{3b}$+ n $(Li)_{3b}$ = 1
	n (Al) = 0.025 ; n(Fe)=0.025

Atom	**Site**	**Wyckoff positions**			**Occupancy**	**B_{iso}(Å^2)**
Li (1)	3a	0	0	0.00	0.030	1.82
Ni (1)	3a	0	0	0.00	0.570	1.82
Li (2)	3b	0	0	0.50	0.970	1.59
Ni (2)	3b	0	0	0.50	0.030	1.59
Co	3a	0	0	0.00	0.150	1.82
Mn	3a	0	0	0.00	0.200	1.82
Al	3a	0	0	0.00	0.025	1.82
Fe	3a	0	0	0.00	0.025	1.82
O	6c	0	0	0.26	2.000	0.57

Experimental conditions

Temperature	~ 298° K
2θ range	15° ≤ 2θ ≤ 100°
2θ step	0.02°
Zero point	0.013
Number of the refined parameters	16

Half-width parameters: U = 0.073; V = -0.011; W = 0.117

Reliability factors: R_{wp}= 8.1 % et R_B = 3.9 %

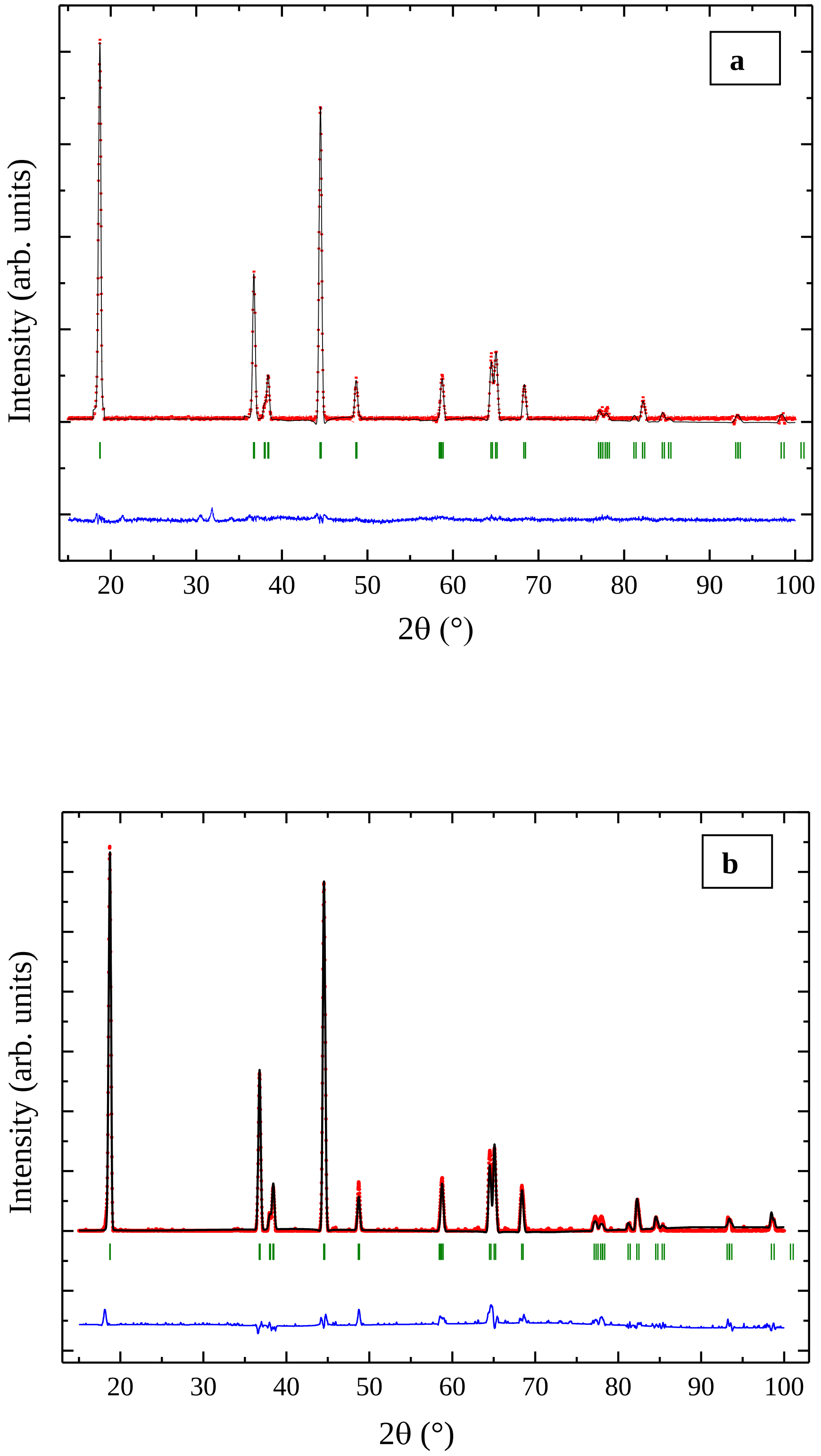

Fig. 42: Rietveld profile refinement results of the NMC (3:1:1) (a) and NMCAF (b) electrode materials: __ observed, __ calculated, __ difference, | Bragg positions

4. Physico-chemical characterization

4.1. Electron paramagnetic resonance

Three electrode materials NMC (3:1:1), NMCAF and a commercial NMC (1:1:1) were investigated by EPR spectroscopy in the temperature range 77°K-295° K. Figs 43 and 44 display the experimental EPR spectra of the three materials recorded respectively at 77°K and 295°K in addition to their corresponding best fits.

The Lorentzian line approach [296] was adopted to achieve a best fit of the experimental spectra [318,319] and gave rise to a single EPR line for the commercial NMC (1:1:1) and two separate EPR lines for the in-lab synthesized NMC (3:1:1) and NMCAF (Fig. 44). The broad line denoted as R_1 has been assigned to paramagnetic Mn^{4+} and the narrower line denoted as R_2 has been attributed to the presence of paramagnetic Ni^{2+} defects [320]. The EPR spectroscopic parameter ΔH_i (line width) is presented as function of the temperature (Fig. 45) where i= 1; 2 are respectively related to R_1 and R_2.

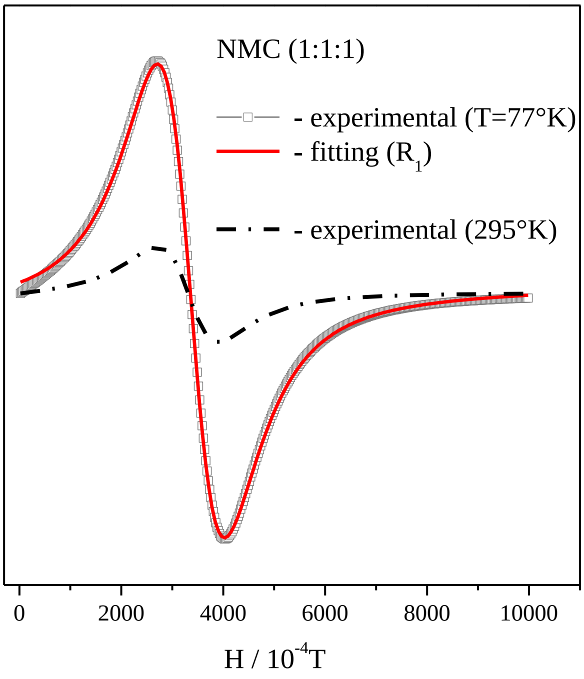

Fig. 43: Experimental EPR spectra of commercial NMC (1:1:1), recorded at 77°K and 295°K. Fitting of the experimental spectra was carried out by a Lorentzian line approach. Fitted and experimental curves are shown

.

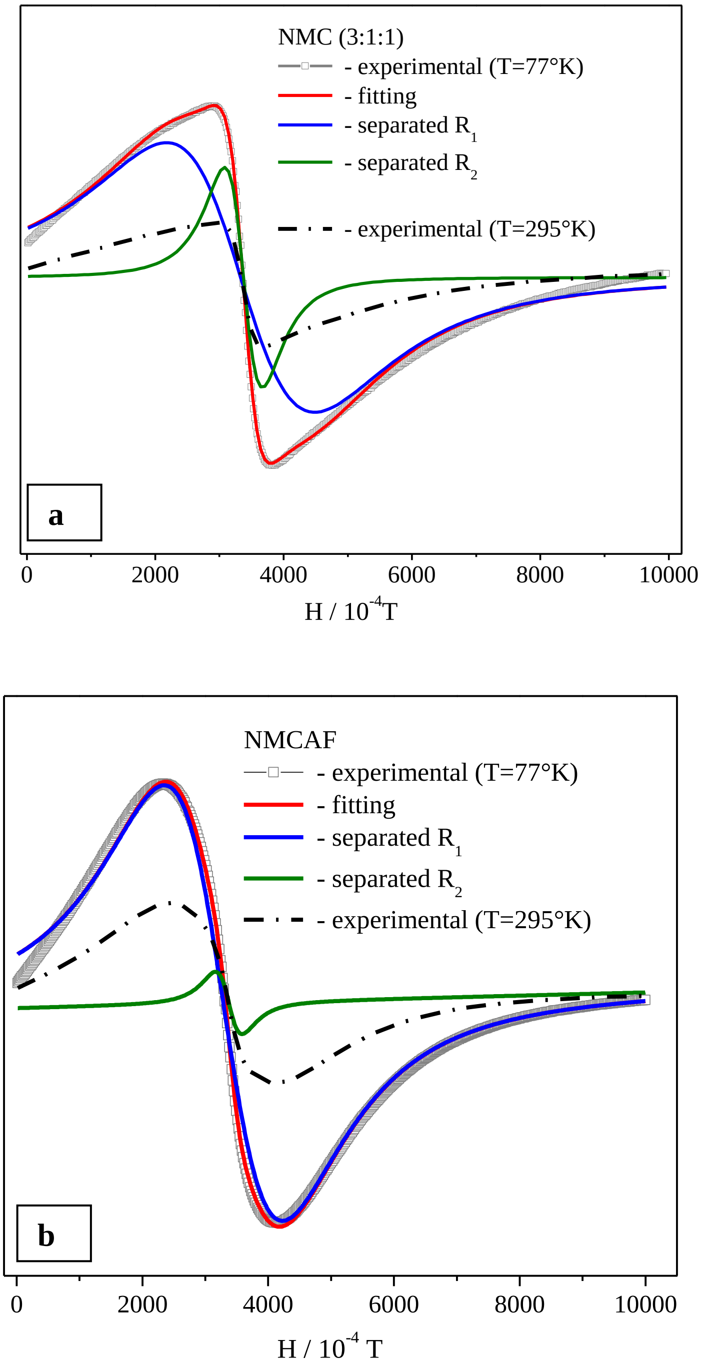

Fig. 44: Experimental EPR spectra of the NMC (3:1:1) (a) and NMCAF (b) materials, recorded at 77°K and 295°K. Fitting of the experimental spectra was carried out by a Lorentzian line approach. The fitted and separated after fitting curves are shown for each material

.

It can be seen that the increase of the temperature resulted in a decrease of ΔH_i. Therefore, the temperature dependence of ΔH_i for the studied materials is in good correlation with the reported data in the literature about NMC materials [320,321].

Recent studies have reported that the EPR line width is strongly related to the material stoichiometry, this can be reflected by the narrowing of the EPR line width ΔH_i when the Ni/Mn ratio diminishes [318]. This effect was likewise observed for the studied materials in the present work since we obtained for NMC (1:1:1), that has a Ni/Mn ratio approximately equal to 1, a value for ΔH_i ~1200 G, while for NMC (3:1:1) with Ni/Mn ~3 we obtained ΔH_i ~2000 G , which agrees well with the EPR results reported in the literature [318]. According to the EPR method, a broadening of the EPR line can be mainly due to a dipole-dipole interaction or / and some exchange interaction between the transition metal ions located in the layered structure especially for materials with high concentration of the paramagnetic centers. It is noteworthy that such interactions in our case are occurring not only for the Mn^{4+} - Mn^{4+} couple, but also for the Mn^{4+} - Ni^{2+} and Ni^{2+} - Ni^{2+} couples.

It can be seen from Fig. 44 that Al and Fe substitution has clearly affected the EPR spectrum of the material. In this case, the results related to the function $\Delta H_i \sim f\ (Ni^{2+})$ reported in the reference [321] are not valid as the NMC (3:1:1) and NMCAF materials have the same Ni stoichiometry. The substantial decrease of the R_2 line width for NMCAF can be related to a decrease of Ni^{2+} defect density. This suggests that the cationic substitution of the active NMC material induced a redistribution of the Ni ions within the structure, which can be a reason behind the decreased cation mixing in NMCAF detected as well by means of Rietveld refinement of the XRD data.

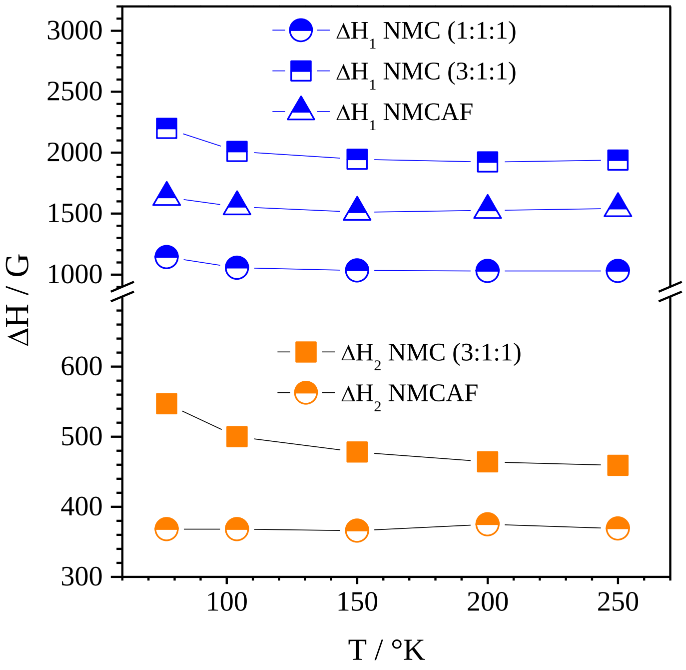

Fig. 45: ΔH as a function of temperature for the commercial NMC (1:1:1) and the NMC (3:1:1) and NMCAF materials prepared in this work, where i= 1; 2 are respectively related to R_1 (assigned to paramagnetic Mn^{4+}) and R_2 (attributed to the presence of paramagnetic Ni^{2+} defects)

One important property to be investigated is the paramagnetic-ferromagnetic phase transition occurring at Tc (Curie point) which is a characteristic temperature for a given type of material. The paramagnetic-ferromagnetic phase transition can be extracted from the analysis of the function $\Delta H_i \sim f(T)$.

Characteristically, when the temperature diminishes, a quick enhancement of ΔH_i can be observed beginning at Tc. For the three studied materials NMC (3:1:1), NMC (1:1:1) (fig. 46) and NMCAF (fig. 45), it can be seen from ΔH_i temperature evolution that Tc keeps a constant value around 125°K, being close to that reported for example in reference [321]. Accordingly, it can be presumed that neither the stoichiometry change nor the cationic substitution has impact on the paramagnetic-ferromagnetic phase transition of the studied on materials.

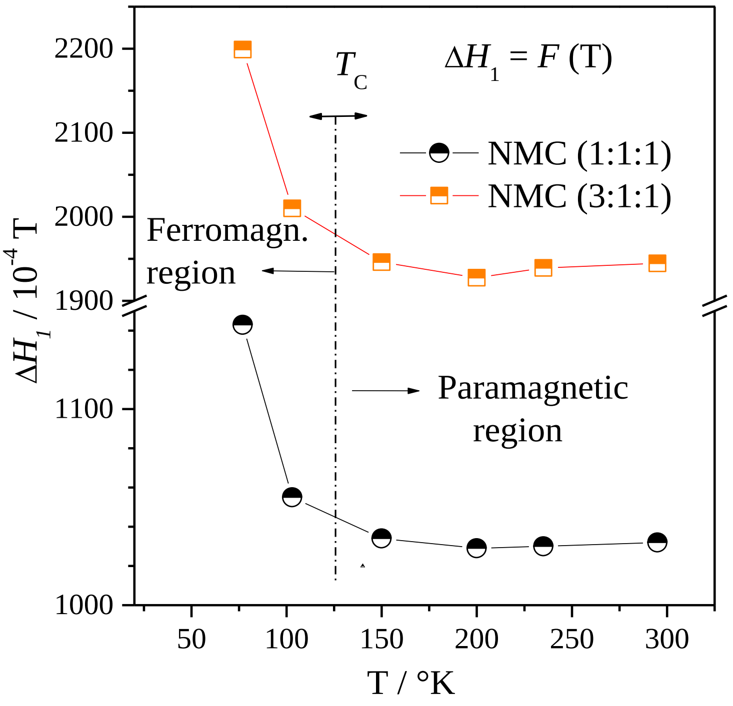

Fig. 46: Representation of the paramagnetic-ferromagnetic phase transition for the in-lab prepared NMC (3:1:1) and the commercial NMC (1:1:1)

5. Electrochemical performance in cycling

5.1. Galvanostatic cycling at constant slow rate C/20

For this electrochemical study, cycling was carried out at the constant slow rate C/20 in the potential range 2.7 - 4.4 V.

To properly compare the potential of lithiation and delithiation taking into account the state of charge for the two active materials NMC (3:1:1) and NMCAF, the galvanostatic curves as a function of the normalized capacity are presented (Fig. 47). In this way, the potential differences can be displayed at any lithiation degree.

One can see that the plateau potential related to the Li^+ insertion increased for the substituted material, whereas it decreased during Li^+ de-insertion in almost the complete charge-discharge interval. In fact, this result suggests that after the cationic substitution, both processes are stimulated because less energy is needed to exchange a certain amount of Li^+. Throughout cycling, the higher potential difference was about 200 mV, related to 25% lithium insertion. Therefore, it is noteworthy that this change was induced by a very low substitution rate (5% in total). The significant modification of the potentials after the cationic substitution is in good agreement with the change of the structural parameters according to the Rietveld refinement data (table 11). Although the lattice parameters have slightly changed with the low substitution rate, the Ni^{2+} occupancy in the 3b sites has significantly decreased to over 60%. This suggests that the cationic substitution offers the possibility of intercalating lithium ions more easily and efficiently by decreasing the degree of cation mixing and increasing the order in the structure. This effect can be the explanation behind the shifts of the insertion/ de-insertion potential plateau.

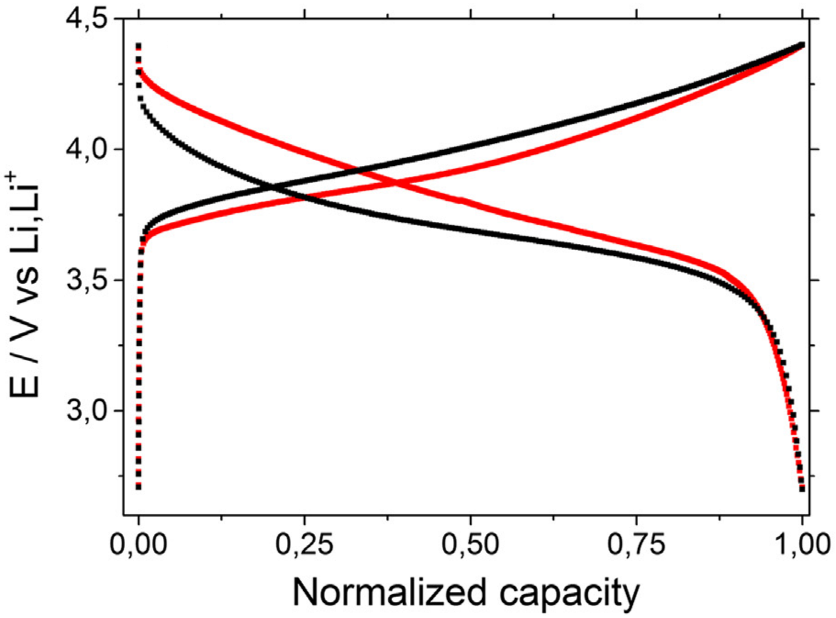

Fig. 47: Comparison of voltage profiles vs. normalized capacity obtained from galvanostatic cycling at C/20 rate of NMC (3:1:1) (black) and NMCAF (red) positive electrode materials at the 10th cycle

.

In addition, from electrochemical and thermodynamic perspective at the equilibrium state, the cell potential at open circuit (E_{OCP} vs. Li, Li^+) depends on the difference between the standard potentials of the two electrodes which is a function of the chemical potentials of the active materials. Thereby, the difference in terms of E_{OCP} can be a way to estimate the variation of the electrochemical potential after the cationic substitution, without intervention of any polarization effect. Our results demonstrate that the initial E_{OCP} of the NMC (3:1:1) material (E_{OCP} (NMC (3:1:1)) = 2.8 V) is higher than that of NMCAF (E_{OCP} (NMCAF) = 2.0 V) which means that NMCAF can be oxidized more easily than NMC (3:1:1).

As we have demonstrated that the structure of the substituted material has been reorganized, it is very likely that the advantageous transformation in the local Ni^{2+} environment has a dominant effect in improving the electrochemical performance.

5.1.1. Study of the derived curve - dx / | dV | = f (V)

In order to facilitate the interpretation of the different slope changes in the potential-composition curve V = f (x), the curves dx/dV (obtained by derivation of the potential-composition curve) were calculated for the two materials NMC (3:1:1) and NMCAF (Fig. 48). Moreover, the curve dx/dV = f (V) is proportional to I = f (V) recorded during cyclic voltammetry. To meet the conventions for the sign of the current, the incremental capacity is taken equal to - dx/| dV |.

The shapes of the intensiostatic curves that represent the evolution of the potential as a function of the lithium composition (V = f (x)) and the derived (-dx/|dV| = f (V)) curves are closely linked. The potential plateau of the intensiostatic curve is reflected in a narrow peak on the derivative curve. An inflection point in the V = f (x)) curve results in a small peak on the derivative curve.

To obtain a good quality derived curve, galvanostatic cycling is preferred to be performed at the slow rate C/20 to remain as close as possible to the thermodynamic equilibrium.
The derived curves in both Fig. 48 present single relatively broad peaks corresponding to the oxidation peak of Ni^{2+} to Ni^{4+} via Ni^{3+} ions during lithium deintercalation (charge). However, no sharp peak was observed, suggesting the absence of first order phase transition during the charge-discharge process.

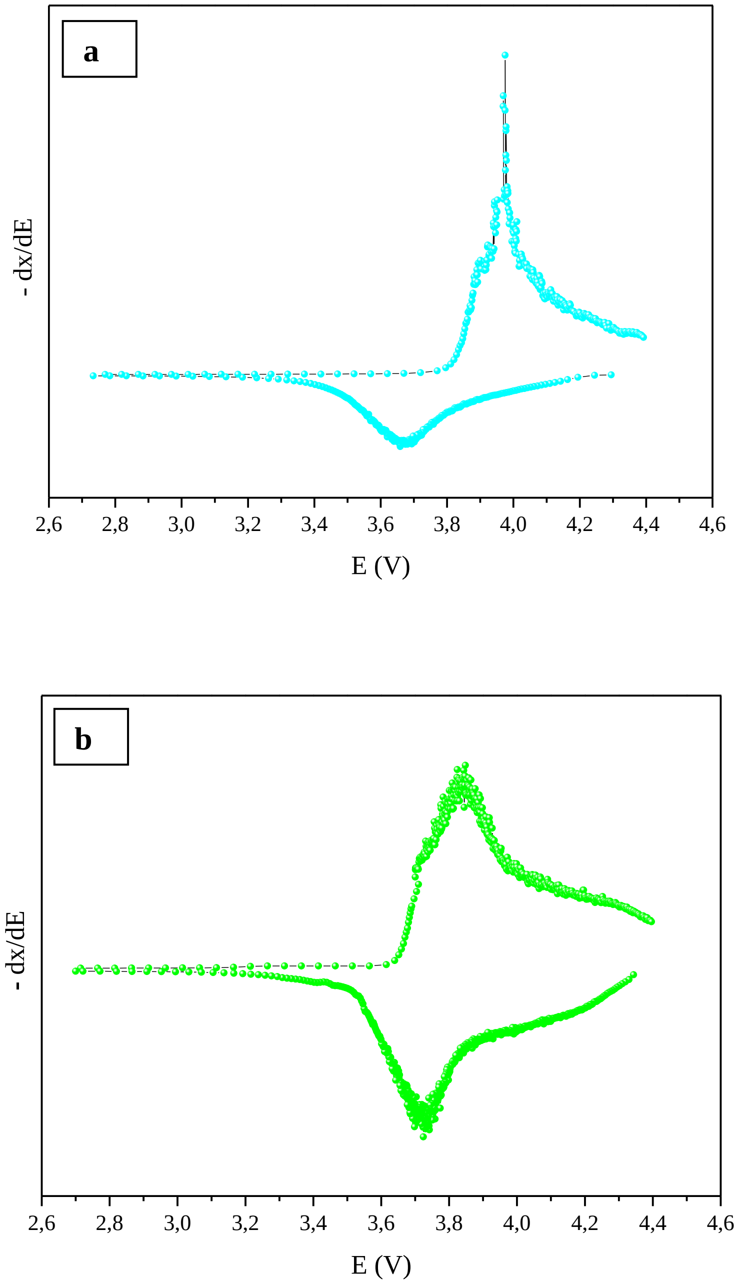

Fig. 48: Variation of the incremental capacity - dx / |dV| as a function of potential for NMC (3:1:1) (a) and NMCAF (b). This function was deduced by deriving the 1st charge / discharge cycle performed in the potential range 2.7 - 4.4 V under C/20 rate

.

5.2. Cyclic voltammetry at various scan rates

Fig. 49 shows cyclic voltammetry curves of NMC (3:1:1) and NMCAF electrodes measured at three different scan rates (0.05, 0.1 and 0.5 mV·s^{-1}). All CV curves show for both materials pairs of cathodic/anodic peaks in the potential ranges 3.60 – 3.75 V and 3.88 – 4.10 V respectively, which corresponds to the lithium ions intercalation/de-intercalation potentials that are characteristics of cathode materials of NMC type.

We also observe that the positions of oxidation and reduction peaks are more stable from one cycle to another for NMCAF which indicates better reversibility of the charge–discharge process for this material even with the scan rate variation.

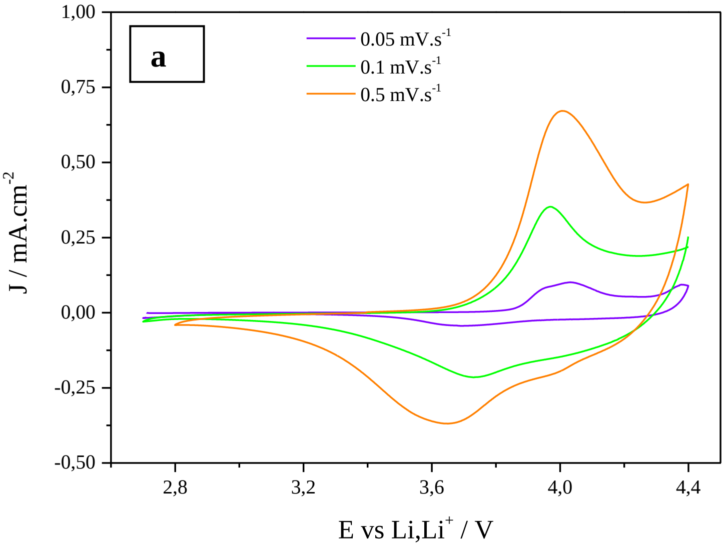

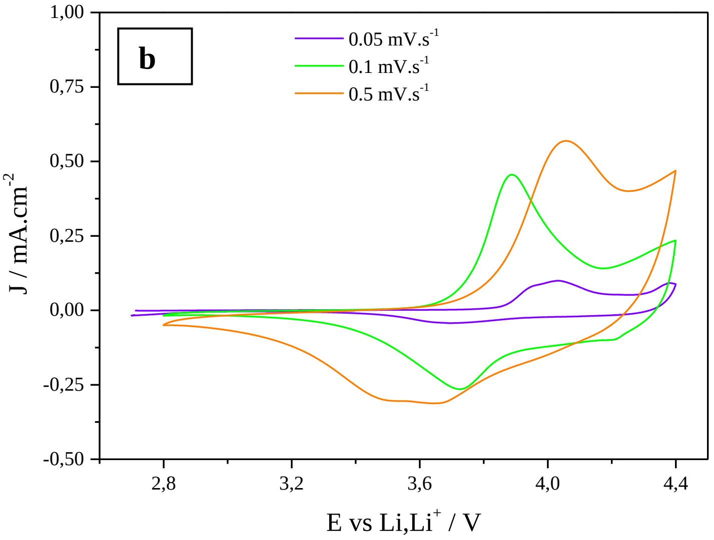

Fig. 49: Cyclic voltammograms of the two cathode materials NMCAF (a) and NMC (3:1:1) (b) in the 2.7V - 4.4V potential range at various scan rates

.

The anodic and cathodic current densities for both NMC (3:1:1) and NMCAF increased considerably with increasing scan rates. Only two broad peaks are observed in each loop for NMC (3:1:1). For NMCAF the two peaks are sharp and more distinguishable.

Thereby, it is noteworthy through the qualitative analysis of the cyclic voltammograms that NMCAF has a kinetic advantage over NMC (3:1:1).

The potential separation between the cathodic and anodic peaks increased with the scan rate, but the ratio of the anodic to the cathodic peak current remains stable (~ -1.8), an indication that there was no side reaction during the intercalation/de-intercalation process [328,329].

Fig. 50 shows the evolution of the current densities of the charge and discharge peaks I_p with the scan rate v for the two materials in a double logarithmic scale.

This relationship can be presented by the following equation [330]:

$$I_p = I_c + I_d = C_1 v + C_2 v^{1/2} \qquad (5.1)$$

where I_p is the peak current density; v is the scan rate; C_1v and $C_2v^{1/2}$ are respectively the current contributions from the surface pseudo-capacitive effect (I_c) and the bulk lithium insertion process (I_d).

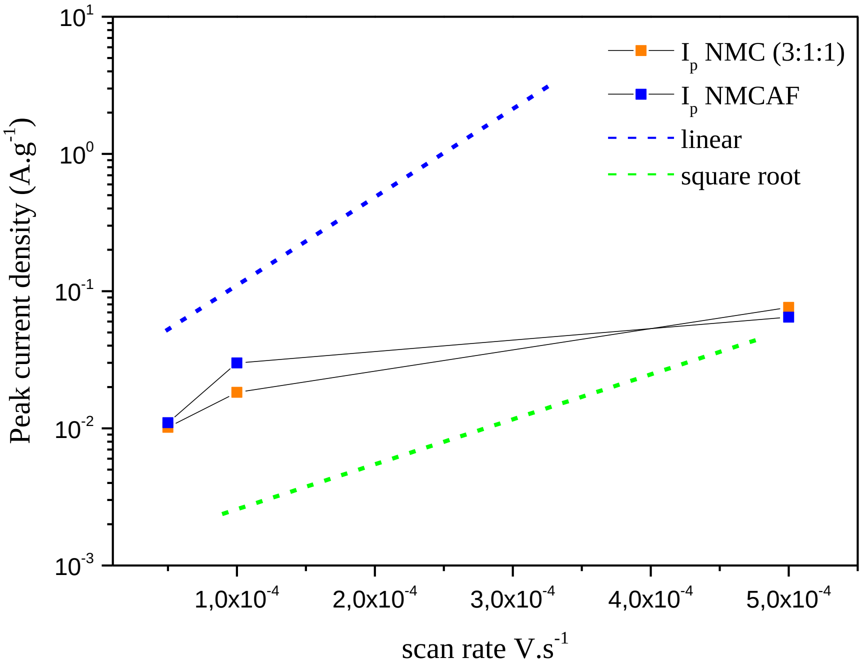

Fig. 50: Evolution of the peak discharge current Ip of NMCAF and NMC (3:1:1) with the scan rate. The blue dashed line represents the linear function $Ip \propto v$ referring to the surface pseudo-capacitive lithium storage process; the green dashed line represents the square root function $Ip \propto v^{1/2}$ referring to the bulk lithium insertion process

The representation of I_p as a function of v for the two materials resulted in a curve that is much closer to the square root than the linear curve, likewise shown in Fig. 50 for comparison. This indicates that the Li^+ diffusion process was the most important key factor for the electrode kinetics.

For further quantitative analysis, the equation (5.1) can be rewritten as follows:

$$I_p / v^{1/2} = C_1 v^{1/2} + C_2 \qquad (5.2)$$

When plotting $I_p/ v^{1/2}$ as a function of $v^{1/2}$ (Fig. 51), a straight curve was obtained for the two studied materials. C_1 and C_2 can then be determined respectively from the curve slope and the interception between the y-axis and the curve.

For instance, the best fit of the $I_p/v^{1/2}=f(v^{1/2})$ for NMCAF provided the following values: $C_1=0.089$ ($Ag^{-1}V^{-1}s$) and $C_2=1.17E^{-4}$ ($Ag^{-1}V^{-1/2}s^{1/2}$).

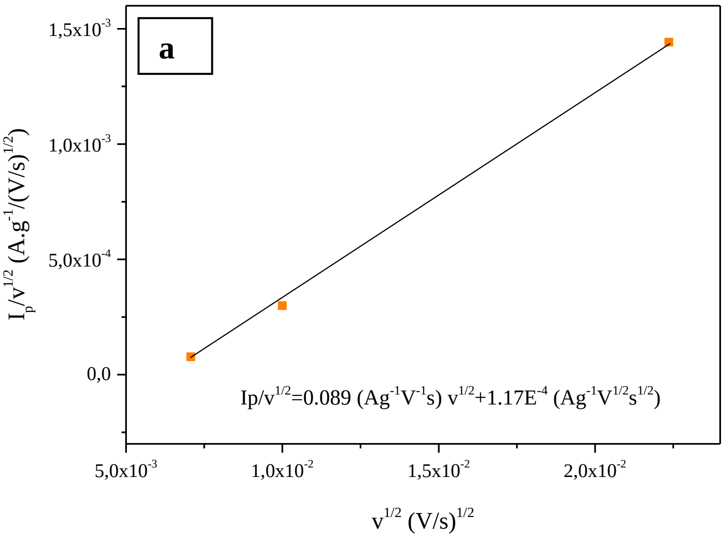

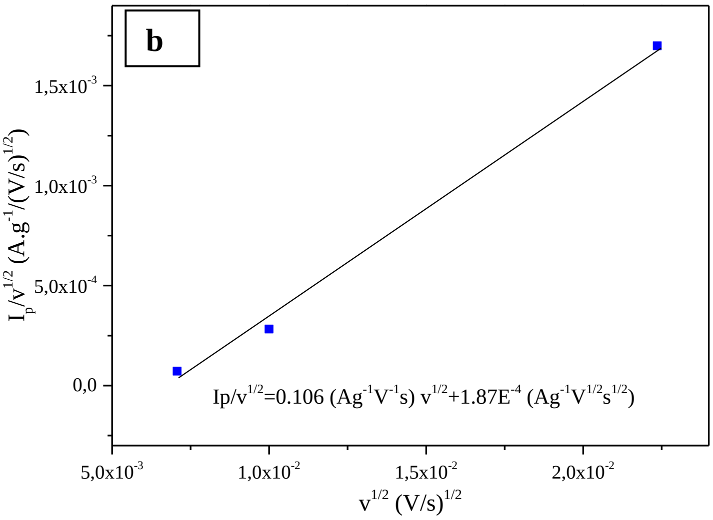

Fig. 51: Evolution of $I_p/v^{1/2}$ as a function of $v^{1/2}$ for NMCAF (a) and NMC (3:1:1) (b) in order to extract the C_1 and C_2 parameters that correspond to the slope and the y-axis intercept point of the curves

.

Afterwards, once C_1 and C_2 values are known, the two different current contributions can be quantified. It is then possible to evaluate I_c and I_d evolution with the scan rates according to equation (5.1) (Fig. 52).

At the three scan rates, I_d is much smaller than I_c for the two cathode materials NMC (3:1:1) and NMCAF suggesting then that the lithium insertion is the dominating storage process for both materials.

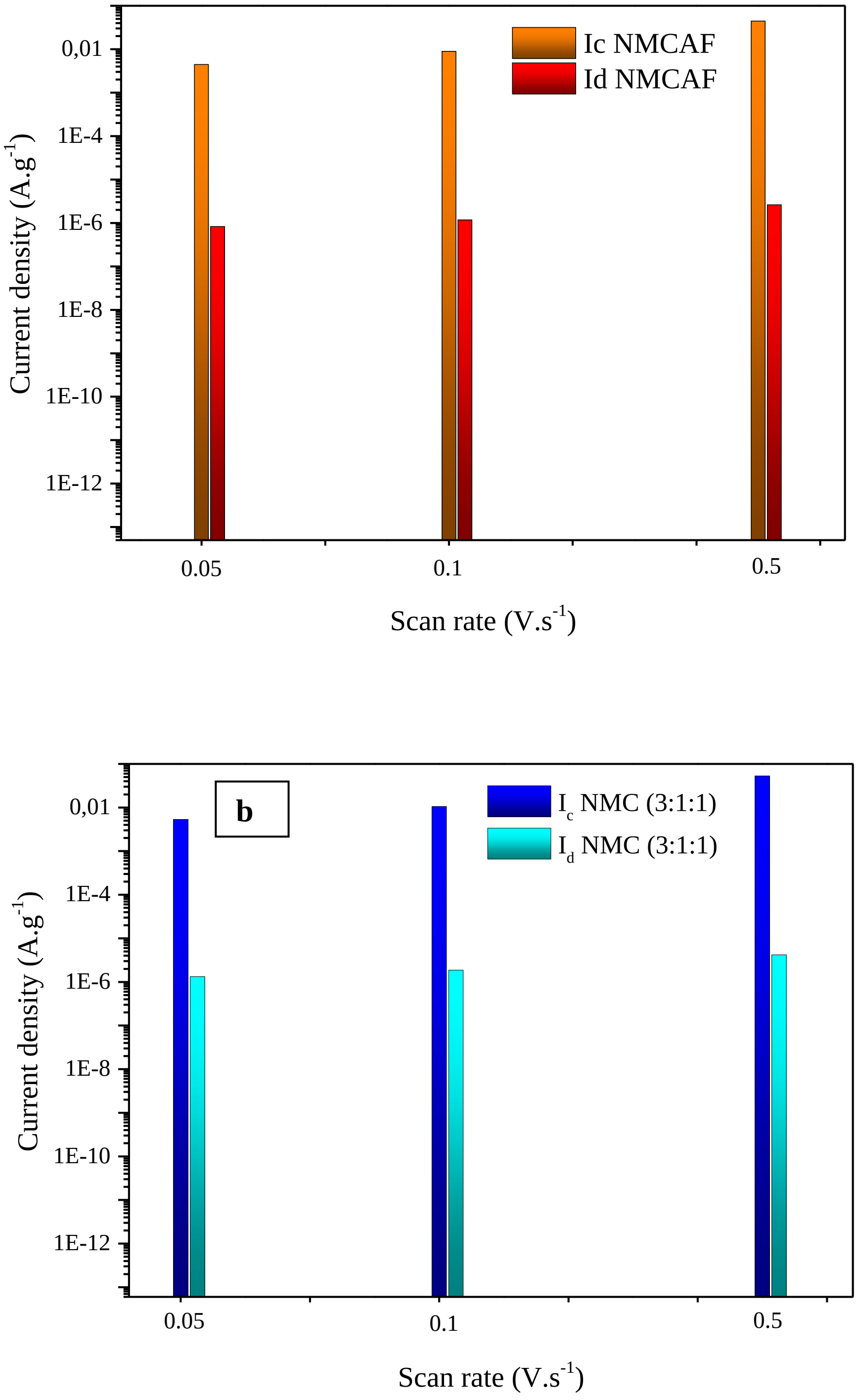

Fig. 52: Calculated surface pseudocapacitive I_c and bulk insertion discharge currents I_d for NMCAF (a) and NMC (3:1:1) (b)

.

5.3. Electrochemical impedance spectroscopy

In order to quantify the Li^+ kinetics for the NMC (3:1:1) and NMCAF cathodes, EIS was employed to determine the diffusion coefficient of the lithium ions, D_{Li+}. The Nyquist plots of the two materials recorded before and after cyclic voltammetry in the frequency range from 100kHz to 100mHz are shown in Fig. 53.

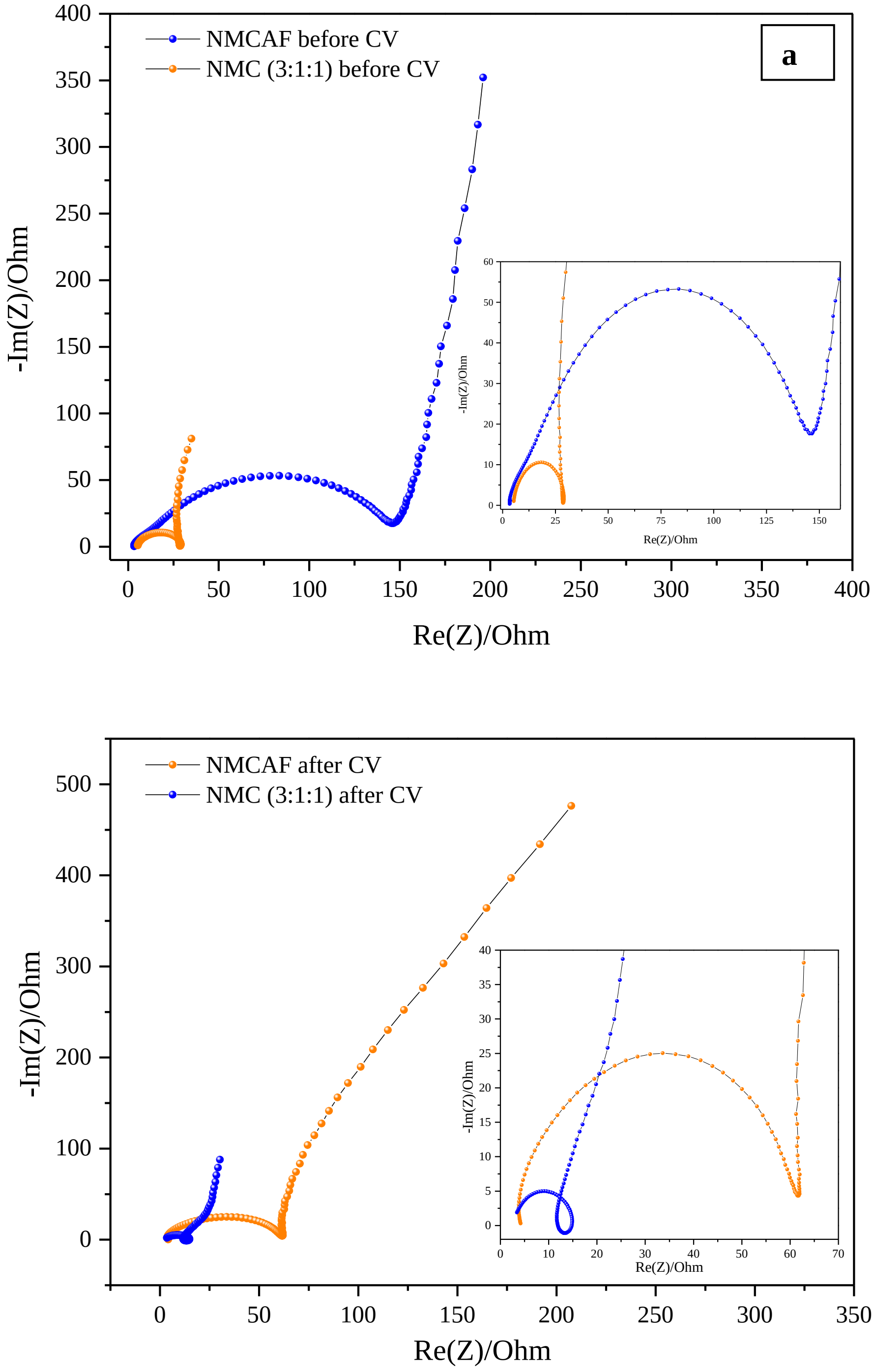

Fig. 53: Nyquist impedance spectra of NMCAF and NMC (3:1:1) before CV (a) and after CV (b) versus Li/Li^+ and an inset of the impedance at high frequencies presented on the right side

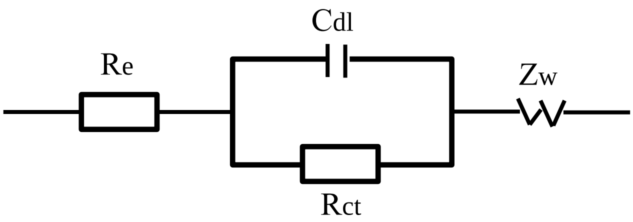

Fig. 54: Equivalent circuit used for fitting the EIS spectra of the NMC(3:1:1) and NMCAF

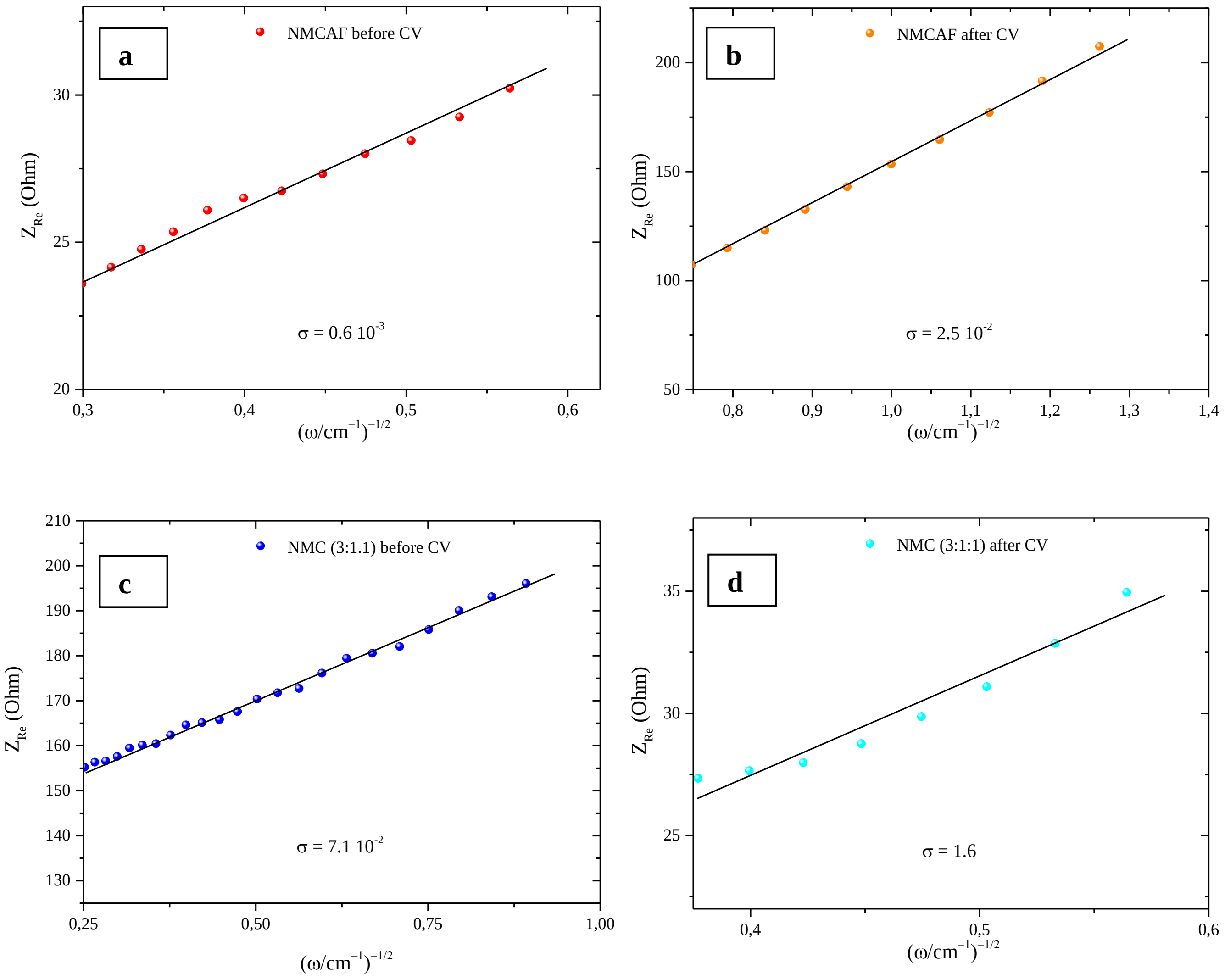

Fig. 55: Evolution of Z_{Re} as a function of the inverse square root of the angular frequency ω for NMCAF before (a) and after CV (b) and NMC (3:1:1) before (c) and after CV (d) in order to extract the Warburg factors σ that correspond to the slope of the curves

The Nyquist plots consist of semicircles closest in shape to an ellipse in the regions of high and intermediate frequency and a straight inclined line in the lower frequency range. The size and the shape of the semicircle are linked to the charge transfer resistance R_{ct} at the cathode-electrolyte interface. In addition to R_{ct}, more parameters are needed to define the total impedance such as: R_e (the electrolyte resistance), C_{dl} (the double-layer capacitance) and Z_w (the Warburg impedance reflecting the lithium ions diffusion in the electrode) as shown in the equivalent circuit presented in Fig. 54. Moreover, EIS can be used to quantify the diffusion of lithium ions for the two studied cathode materials. For this, the equation (5.3) is used to calculate the diffusion coefficient of the lithium ions:

$$D(Li^{+}) = \frac{1}{2}\left(\frac{R^2T^2}{n^4A^2F^4C^2\sigma^2}\right) \quad (5.3)\ [331]$$

Where R is the gas constant (8.314 J K−1 mol^{-1}), T is the absolute temperature (~ 298°K), A is the cathode/electrolyte interface area (~ 1.13 cm^2), n is the number of electrons per molecule (here, n =1), F is the Faraday constant (~96 485 s A / mol), C is the concentration of lithium ions (~ 1 mol/cm^3), and σ is the Warburg factor that is equal to the slope value of the function $Z_{re}=f(\omega^{-1/2})$ with $\omega=2\pi f$ (Fig. 55). The diffusion coefficient of the lithium ion calculated based on equation (5.3) and Fig. 55 are displayed in table 16.

Table 16: Diffusion coefficients of lithium ions for the two materials NMC (3:1:1) and NMCAF before and after CV.

D (Li+) **Cathodes**	**before CV**	**after CV**
NMCAF	$4.4\ 10^{-11}\ cm^2s^{-1}$	$1.1\ 10^{-12}\ cm^2s^{-1}$
NMC (3:1:1)	$3.9\ 10^{-13}\ cm^2s^{-1}$	$1.7\ 10^{-14}\ cm^2s^{-1}$

Therefore, D_{Li+} for the fresh double substituted material is calculated to be 4.4 10^{-11} cm^2s^{-1}, about two orders of magnitude higher than the fresh NMC (3:1:1) (3.9 10^{-13} cm^2s^{-1}). The higher value of the lithium diffusion coefficient obtained for NMCAF material shows the beneficial effect of the double substitution on the diffusion of lithium ions. Indeed, the fast diffusion of lithium ions leads to a significant amount of exchanged lithium ions and consequently to a greater reversible capacity

5.4. Rate capability

To characterize the response of the NMC (3:1:1) and NMCAF materials to different C rates, rate capability tests were carried out.

Initially the cells were cycled at C/20 rate to extract the maximum amount of lithium ions. This step is followed by five cycles at each C rate performed successively at C/10, C/5, C, 2C and 5C. Between each cycle, a relaxation time of 1 h was applied to stabilize the battery voltage.

This electrochemical test shows that the response of the double substituted material is significantly better compared to the pristine NMC (3:1:1) even at high rates up to 5C (Fig. 56). Indeed, the capacities of the NMCAF material are about 187, 167, 152, 143, 128 and 106 mAh g^{-1} at C/20, C/10, C/5, C, 2C and 5C, respectively; while pristine NMC (3:1:1) provides capacities of about 154, 129, 82, 52, 41 and 32 mAh g^{-1} at the corresponding rates.
Moreover, considerable capacity retention throughout cycling at the different applied C rates is observed for NMCAF, which is in good agreement with the results previously reported in Fig. 40.

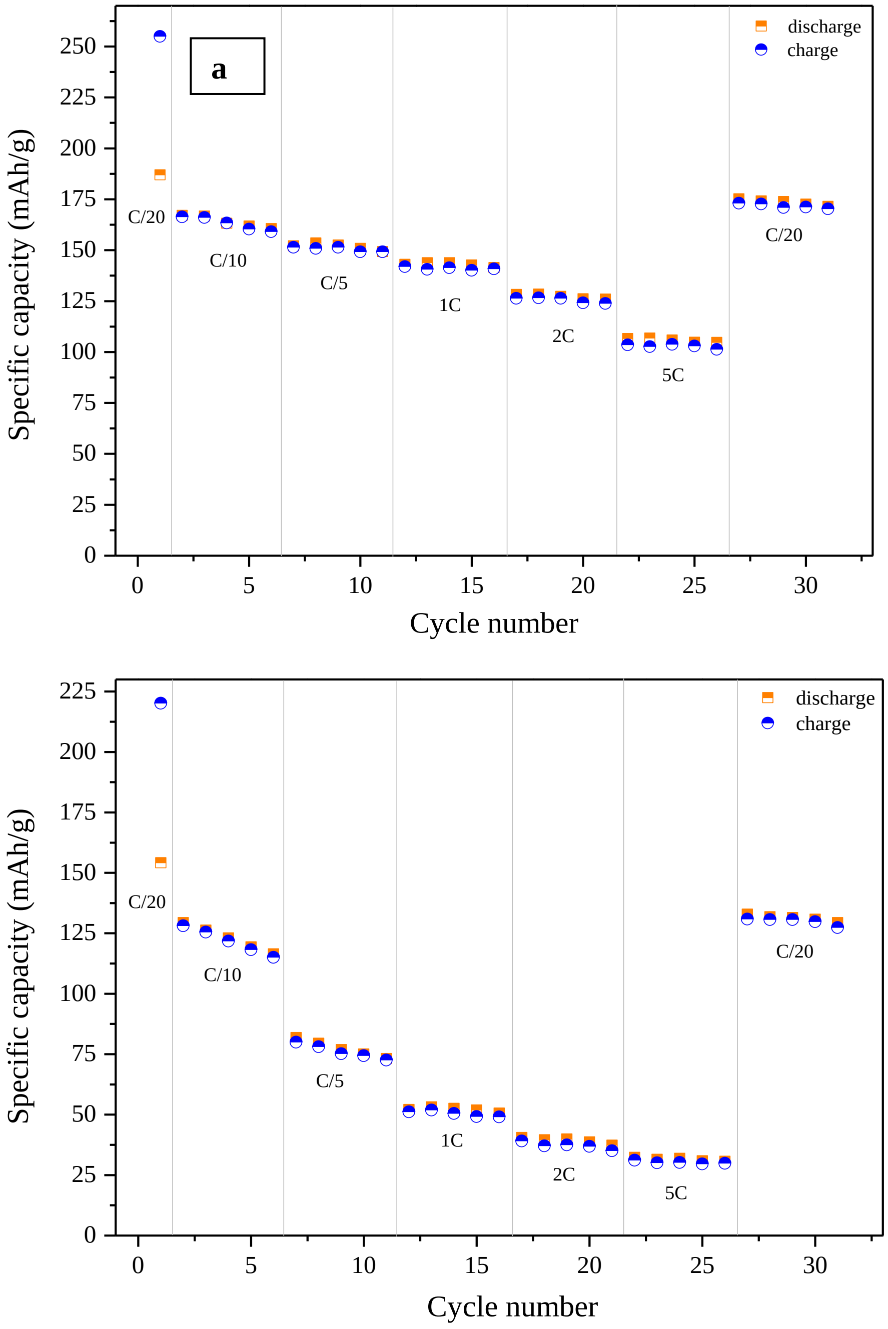

Fig. 56: Rate capability of NMCAF (a) and NMC (3:1:1) (b) tested between C/20 and 5C rates in the 2.7V - 4.4V potential range

5.5. Lithium diffusion coefficient study by GITT

In order to accurately follow the intercalation-deintercalation reaction of lithium ions and to determine the chemical diffusion coefficient of the doubly substituted material NMCAF, a GITT study was performed. During the measurement, a current of 0.2 mA was applied as pulses (τ) of 5 minutes each and alternated with relaxation periods of 1 hour during which the circuit is open. The system then relaxes spontaneously to its equilibrium potential. The procedure is continued until the system reaches the cut-off voltage.

The variation of the potential at equilibrium versus time is reported in Fig. 57. Indeed, the continuous evolution of the potential at thermodynamic equilibrium reveals that no structural phase transition of the first order is taking place during the electrochemical cycling.

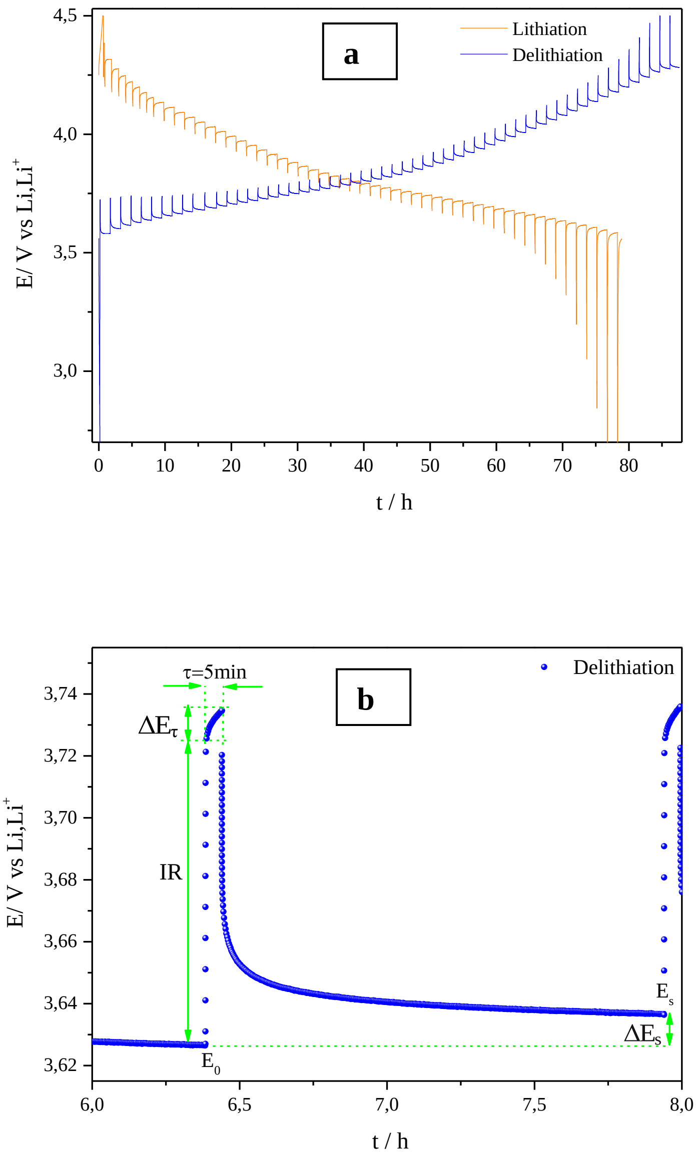

Fig. 57: Galvanostatic intermittent titration of the NMCAF material during charge (blue) and discharge (orange) (a) and a scheme of a single GITT step at around 3.63 V (b)

For illustration, one titration profile recorded at 3.63 V is presented in Fig. 57b with the related parameters.

The chemical diffusion is accepted to follow Fick´s second law of diffusion. With some simplifications, the equation for D_{Li}^{+} can be written as follows [332]:

$$D_{Li^+} = \frac{4}{\pi}\left(\frac{m_B V_M}{M_B S}\right)^2 \left(\frac{\Delta E_S}{\tau\left({}^{dE_\tau}/_{d\sqrt{\tau}}\right)}\right)^2 \quad (5.4)$$

where m_B, V_M and M_B are respectively the mass, the molar volume and the molecular weight, S is the surface area of the electrode, ΔE_s is the difference between the original voltage E_0 and the steady-state voltage E_s, τ is the pulse duration.

First, ΔE_s variation with the square root of τ is presented in Fig. 58 and shows a good linearization. The corresponding values to the curve slope and interception with the y axis are likewise reported.

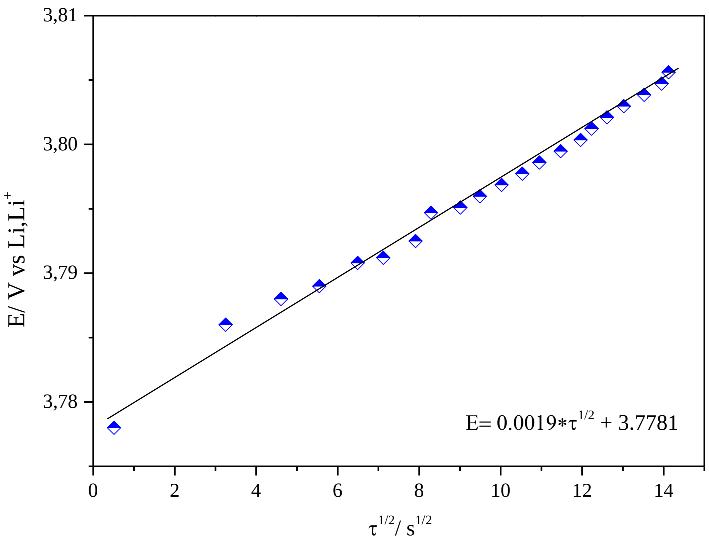

Fig. 58: Potential transient linearization during charge injection period in the coordinates $E=f(\tau^{1/2})$

Based on those results, the Li^+ chemical diffusion coefficients as a function of the cell voltage can be plotted as shown in Fig. 59. As one can see, the curve of the chemical diffusion coefficients takes a twisting shape and the values are in the range of 1.10^{-12} and 1.10^{-9} cm^2/s in the voltage range of 3.6–4.4 V, which is in good agreement with the values obtained by EIS and reported in table 16. The calculated values for D_{Li+} by the GITT method correlate well with literature data for similar compounds [333].

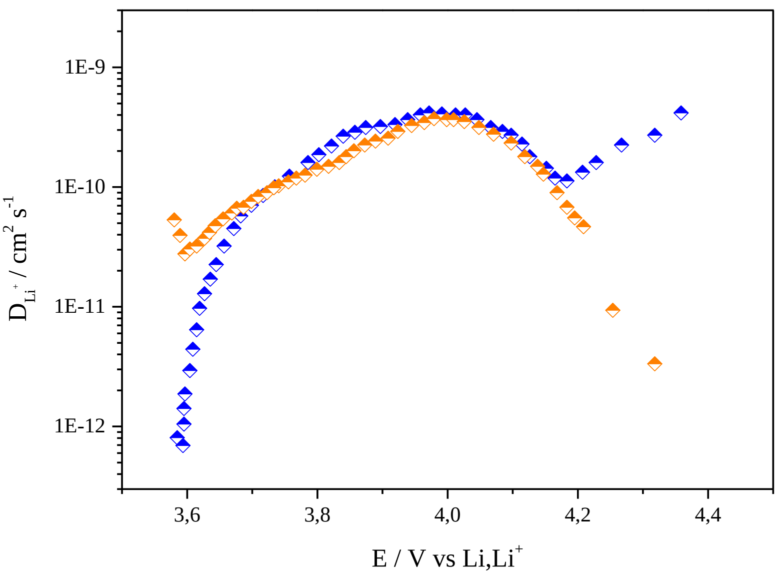

Fig. 59: Evolution of the apparent diffusion coefficient upon charge (blue) and discharge (orange) of the NMCAF material

.

6. Chemical deintercalation

6.1. Preparation of the samples

$Li_xNi_{0.6}Mn_{0.2}Co_{0.2}O_2$ and $Li_xNi_{0.6}Mn_{0.2}Co_{0.15}Al_{0.025}Fe_{0.025}O_2$ phases were chemically prepared by mixing a non-aqueous NO_2BF_4 / acetonitrile solution and the starting materials NMC (3:1:1) and NMCAF. Given the strong oxidizing character of NO_2BF_4, chemical de-intercalation was performed inside a glove box under argon atmosphere. In general, NO_2BF_4 may cause an irreversible de-intercalation; therefore, it should be diluted in acetonitrile up to 0.1 mol/l. About 300 mg of active material was used in suspension in the appropriate volume the NO_2BF_4 / acetonitrile solution under magnetic stirring for 24 hours. The de-intercalated lithium ratio can be determined experimentally according to the following reaction equation:

$$LiMO_2 + (1 - x)\ NO_2BF_4 \rightarrow Li_xMO_2 + (1 - x)\ NO_2 + (1 - x)\ LiBF_4 \qquad (5.5)$$

with M = $Ni_{0.6}Mn_{0.2}Co_{0.2}$ or $Ni_{0.6}Mn_{0.2}Co_{0.15}Al_{0.025}Fe_{0.025}$

Once the reaction is completed, the formed products are recovered by filtering. They are then rinsed several times with acetonitrile in order to remove all traces of $LiBF_4$. The de-intercalated materials are then ready when they have undergone a heat treatment at 80°C for 2 hours under vacuum.

6.2. Characterization of the deintercalated phases

6.2.1. XRD+Rietveld refinement

A comparison of the X-ray diffractorgamms of the de-intercalated phases (Figs 60 and 61) shows a slight shift of the diffraction lines, with lithium extraction, in the order of 0.01% for both materials. All the de-intercalated phases crystallize in the rhombohedral (R-3m) system and therefore have the same structure as the starting phase. No significant variation in the position of the diffraction lines and no appearance of new diffraction peaks are then observed. This means that the method of chemical deintercalation by NO_2BF_4 oxidant allows the extraction of the desired lithium amount by adjusting the starting stoichiometry without structural changes.

Nevertheless, it is noteworthy that for the lithium poor phases $Li_{0.1}Ni_{0.6}Mn_{0.2}Co_{0.2}O_2$ and $Li_{0.1}Ni_{0.6}Mn_{0.2}Co_{0.15}Al_{0.025}Fe_{0.025}O_2$, the X ray diffractogramms present larger diffraction lines indicating a loss of the material crystallinity.

According to Choi and Manthiram who confirmed that the disorder obtained in the structures of NMC is mainly due to a transformation of the O3-type (space group R-3m) into O1-type (space group P-3m1) [334], we can attribute the loss of crystallinity observed for NMC (3:1:1) and NMCAF at x(Li) ~ 0.1 to the presence of traces of the new phase called O1. Such a transformation was indicated in the XRD patterns of the de-intercalated phases by the appearance of a shoulder on the right hand side of the strong reflection around $2\theta = 19.44°$ for NMC and $2\theta = 19.08°$ for NMCAF.

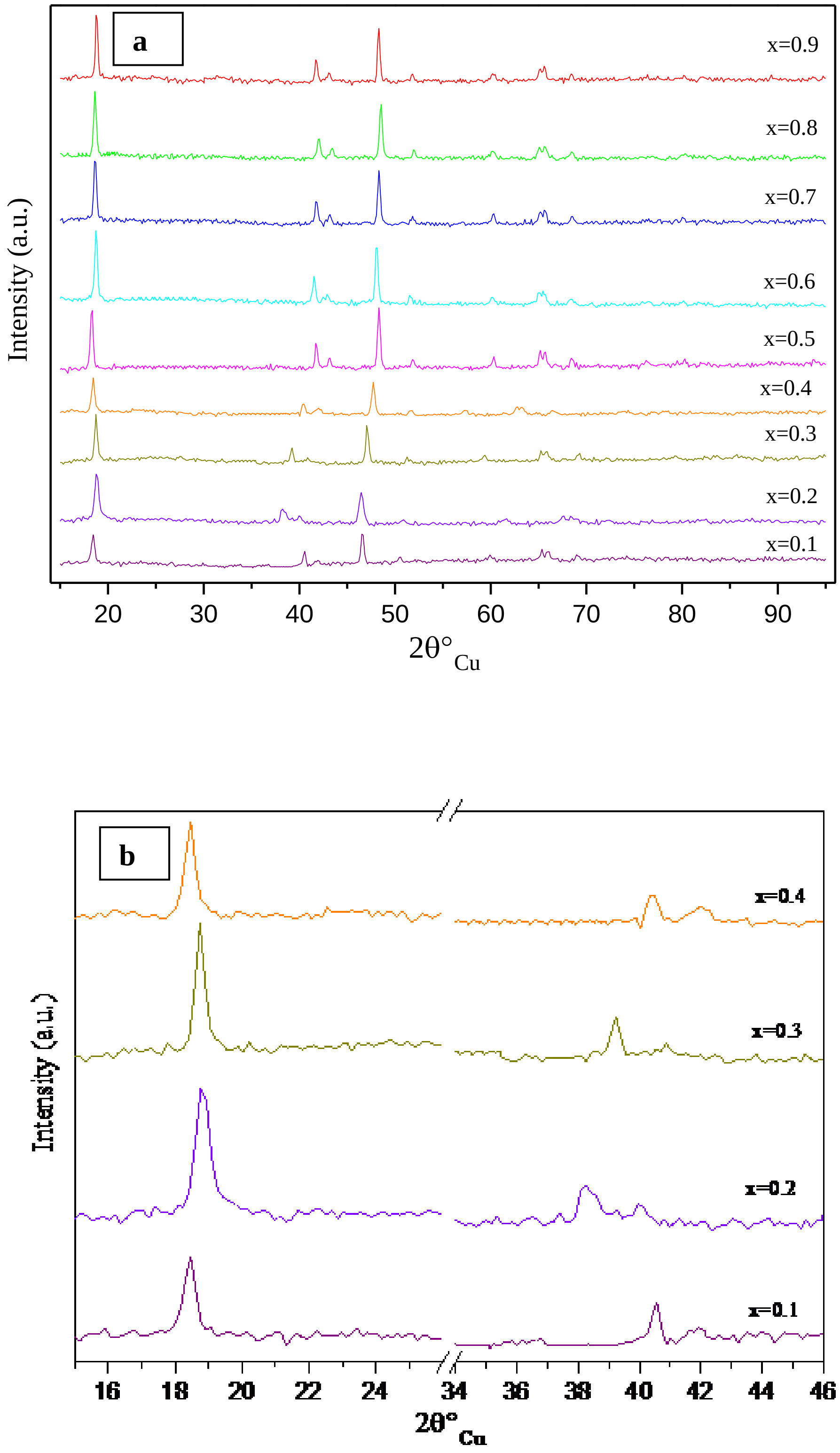

Fig. 60: XRD patterns of the $LixNi_{0.6}Mn_{0.2}Co_{0.15}Al_{0.025}Fe_{0.025}O_2$ phase ($0.1 \leq x \leq 0.9$) chemically de-intercalated by NO_2BF_4 in acetonitrile (a) an inset in the $2\theta_{Cu}$ range 15° - 46° of the same phase at ($0.1 \leq x \leq 0.4$) is presented in (b)

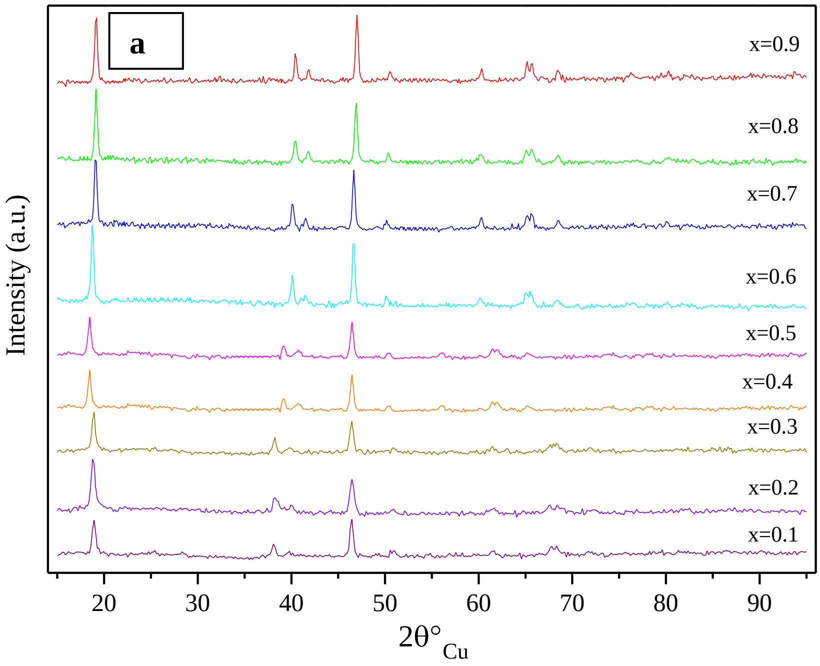

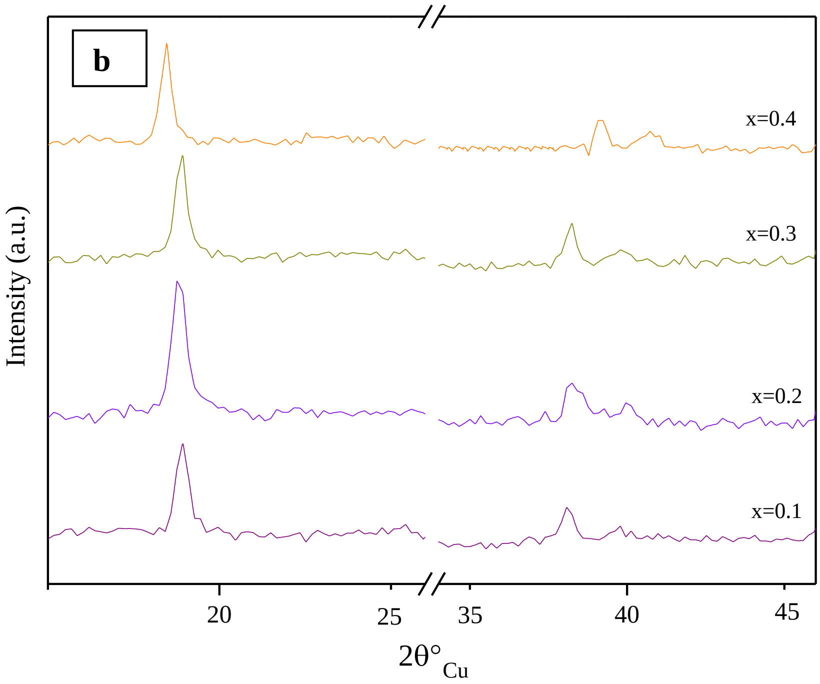

Fig. 61: XRD patterns of the $LixNi_{0.6}Mn_{0.2}Co_{0.2}O_2$ phase ($0.1 \leq x \leq 0.9$) chemically de-intercalated by NO_2BF_4 in acetonitrile (a) an inset in the $2\theta_{Cu}$ range 15° - 46° of the same phase at ($0.1 \leq x \leq 0.4$) is presented in (b)

The O1 stacking can be described by assuming that the octahedral sites of the interlayer space are sharing faces with MO_6 octahedra [335,336] (Fig. 62). For instance, the transformation of the O3- $Li_xNi_{0.6}Mn_{0.2}Co_{0.2}O_2$ phase into O1- $Li_xNi_{0.6}Mn_{0.2}Co_{0.2}O_2$ phase which is a thermodynamically unstable stacking is occurring at low lithium compositions ($x \sim 0.1$) but with very slow reaction kinetics.

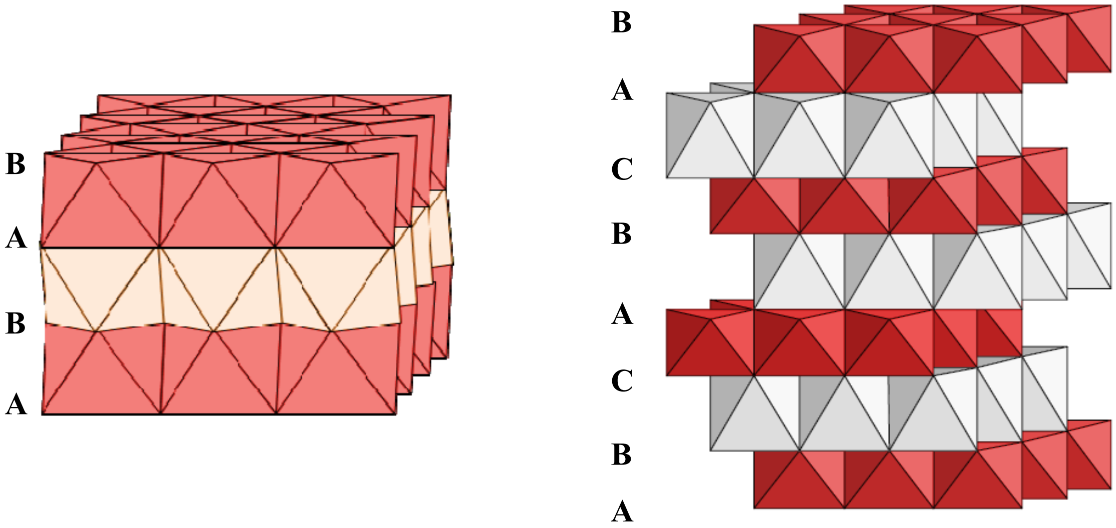

Fig. 62: Schematic representation of the O1 stacking (left) and the O3 stacking (right). A,B and C indicate the positions of the oxygen ions in the lattice [336,337]

.

In order to deduce in particular the percentage of each phase in the mixture, it was necessary to perform a structural refinement by Rietveld of the de-intercalated phases.

Initially, the structural refinement was conducted by considering the existence of a single dominant phase with hexagonal symmetry described in the R-3m space group. We noticed that the XRD profile was not simulated adequately, which was explained by the presence of traces of the O1 phase described in the P-3m1 space group.

To this end, a second step consisted of refining the structure supposing the presence of two phases O3 and O1. The refinement resulted then in a phase mixture O3-type/O1-type with the molar proportions (94:6) for NMC(3:1:1) and (97:3) for NMCAF, indicating that for both materials and especially for the double substituted one, a small amount of O3-$Li_xNi_{0.6}Mn_{0.2}Co_{0.15}Al_{0.025}Fe_{0.025}O_2$ turned into O1- $Li_xNi_{0.6}Mn_{0.2}Co_{0.15}Al_{0.025}Fe_{0.025}O_2$

Results from the literature showed that for Li_xNiO_2 and Li_xCoO_2, the samples maintain their initial O3 structure for $0.4 < x < 1$ and $0.35 < x < 1$ respectively [336]. This makes the two studied compounds especially NMCAF that was able to maintain O3 structure for a wider lithium amount of $x \sim 0.2$, a strong candidate in terms of stability throughout lithium de-intercalation process.

To better quantify the structural stability of NMC (3:1:1) and NMCAF materials, Rietveld refinement of the XRD data recorded for all the de-intercalated phases (0.1<x<0.9) was conducted. The lattice parameters a_{hex} and c_{hex} were therefore presented as a function of x(Li) (Fig. 63).

Up to the lithium composition x = 0.2, a_{hex} parameter which characterize the metal-metal distance decreases with lithium extraction due to the oxidation of Ni^{3+} ions Ni^{4+} ions of smaller size. The c_{hex} parameter increases initially due to the increase of the electrostatic repulsions between oxygen layers located on either side of the interlayer space, then c_{hex} decreases slightly for 0.5<x<0.2 then falls dramatically once the lithium composition becomes less than 0.2. The structure becomes sufficiently covalent so that the steric effects are predominant over the electrostatic effects [338].

For the NMC (3:1:1) material, starting from x<0.3, the significant broadening of the diffraction lines, particularly (003), suggests the presence of fluctuations in the cationic distribution (excess nickel ions and remaining lithium ions) in the interlayer space, leading to a heterogeneous distribution of interlayer distances in the structure. This value is lower for NMCAF material which exhibited already less cation mixing at the initial state x(Li)=1.0.

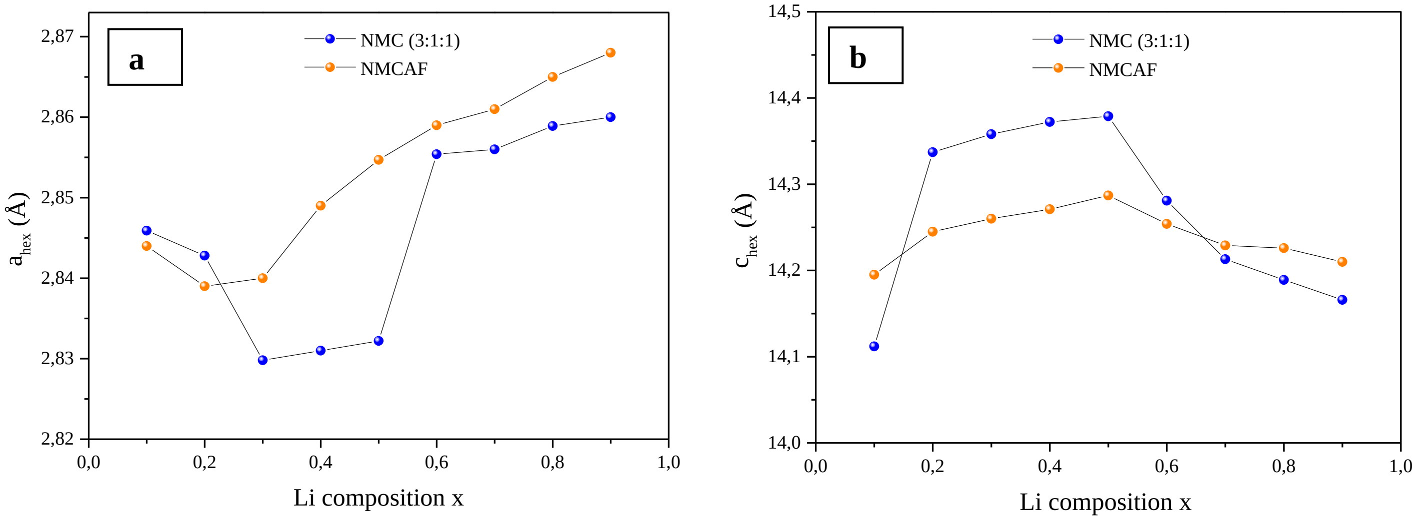

Fig. 63: Evolution of the lattice parameters a_{hex} (a) and c_{hex} (b) (deduced from XRD Rietveld refinement of the phases $LixNi_{0.6}Mn_{0.2}Co_{0.2}O_2$ and $LixNi_{0.6}Mn_{0.2}Co_{0.15}Al_{0.025}Fe_{0.025}O_2$ ($0.1 \leq x \leq 0.9$) as a function of lithium composition (x)

Despite a_{hex} and c_{hex} variations, the lattice volume varies slightly in the studied composition range (Fig. 64) (approximately 0.013% for NMC (3:1:1) and 0.010% for NMCAF). This result is very important from applications point of view and in terms of safety. Indeed, the good cycleability of the cell depends on the volume change of the material.

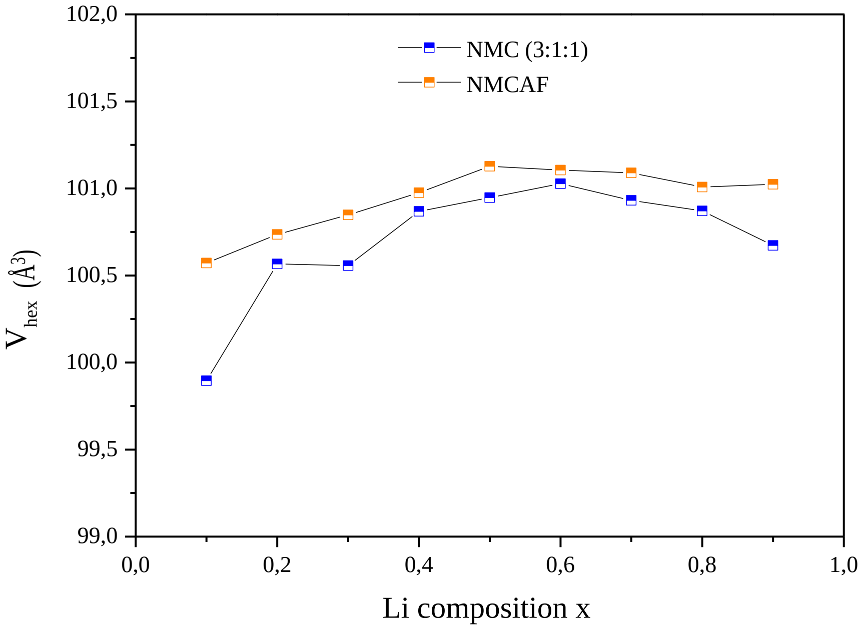

Fig. 64: Evolution of the lattice volume V_{hex} of the phases $Li_xNi_{0.6}Mn_{0.2}Co_{0.2}O_2$ and $Li_xNi_{0.6}Mn_{0.2}Co_{0.15}Al_{0.025}Fe_{0.025}O_2$ ($0.1 \leq x \leq 0.9$) as a function of lithium composition (x)

In the following, the thermal stability of the two compounds at the de-intercalated state will be studied in a way to assess the heating effect on the structural changes.

6.2.2. Safety study at the deintercalated state

6.2.2.1. Introduction

The thermal stability of cathode materials is a crucial factor in terms of of safety. Indeed, the electrochemical properties and performance of cathode materials for LIB are strongly related to the crystal structure of materials and their structural changes induced by the heating effect at the charge state.

Most of the reported works focused on studying the thermal stability of phases achieved by electrochemical de-intercalation. However, this method gives rise to phases with not only the active material but also the usual additives, mainly the conductive agent and the binder. This makes analysis of the active material relatively difficult. For this reason, in this work the phases were prepared by chemical de-intercalation to remove all contributions of the electrolyte and additives.

6.2.2.2. Study by DTA-TG

Thermogravimetric analysis (TGA) was used to study the thermal stability of de-intercalated phases by measuring and tracking the mass changes throughout a heat treatment in air from room temperature to 600°C with a heating rate of 10°C/min.

As shown by the weight loss curves in Fig. 65, the thermogravimetric curves for the two materials NMC (3:1:1) and NMCAF present almost similar behaviors. Continuous mass losses are observed between 100 and 600°C, corresponding most probably to oxygen release. Indeed, it has been proved that the thermal degradation phenomena are mainly due to the oxygen evolution and not to the structure degradation [227,339]. The danger posed by the oxygen release from the material in the charged state is that oxygen can react with the electrolyte and lead to exothermic reactions that can affect the cycleability and cause thermal runaway of the battery.

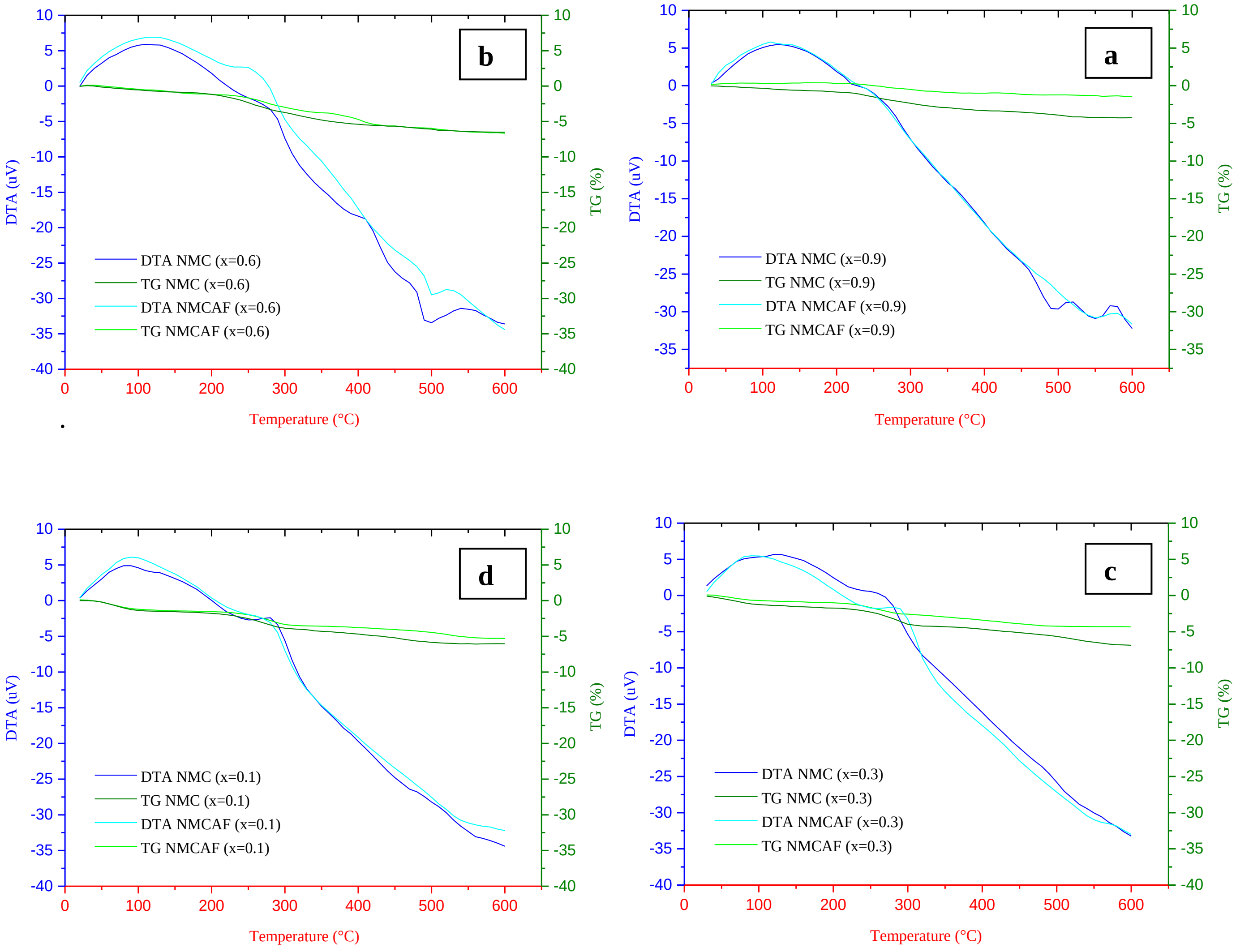

Fig. 65: Thermogravimetric analysis of the de-intercalated phases $Li_xNi_{0.6}Mn_{0.2}Co_{0.2}O_2$ and $Li_xNi_{0.6}Mn_{0.2}Co_{0.15}Al_{0.025}Fe_{0.025}O_2$ with x=0.9 (a) x=0.6 (b) x=0.3 (c) x=0.1 (d) carried out under air, from room temperature to 600 ° C

According to the TGA curves, a higher mass loss was observed for $Li_xNi_{0.6}Mn_{0.2}Co_{0.2}O_2$ phases than for $Li_xNi_{0.6}Mn_{0.2}Co_{0.15}Al_{0.025}Fe_{0.025}O_2$ which is probably due to the stabilizing effect of the double substitution with Al and Fe. Indeed, Al^{3+} and Fe^{3+} ions, that are electrochemically inactive in the selected potential range, played obviously a role in the stabilization of the structure and for damping the oxygen loss during the heat treatment, leading then to an improvement in the thermal stability of the doubly substituted phase.

6.2.2.3.X-ray diffraction analysis

Subsequently, we performed a study by XRD of the de-intercalated phases $Li_xNi_{0.6}Mn_{0.2}Co_{0.2}O_2$ and $Li_xNi_{0.6}Mn_{0.2}Co_{0.15}Al_{0.025}Fe_{0.025}O_2$ (with x = 0.1; 0.3; 0.6; 0.9), having undergone DTA-TG treatment up to 600 ° C.

- $Li_xNi_{0.6}Mn_{0.2}Co_{0.15}Al_{0.025}Fe_{0.025}O_2$

We clearly see from Fig. 66 that no change or appearance of additional diffraction peaks that characterize a spinel phase (S.G.: Fd3m) took place, confirming the structural stability of the de-intercalated NMCAF phases up to 600°C despite the weight loss of about 1.73%. All X-ray diffractograms of the de-intercalated phases can be indexed in the hexagonal system (S.G.: R-3m).

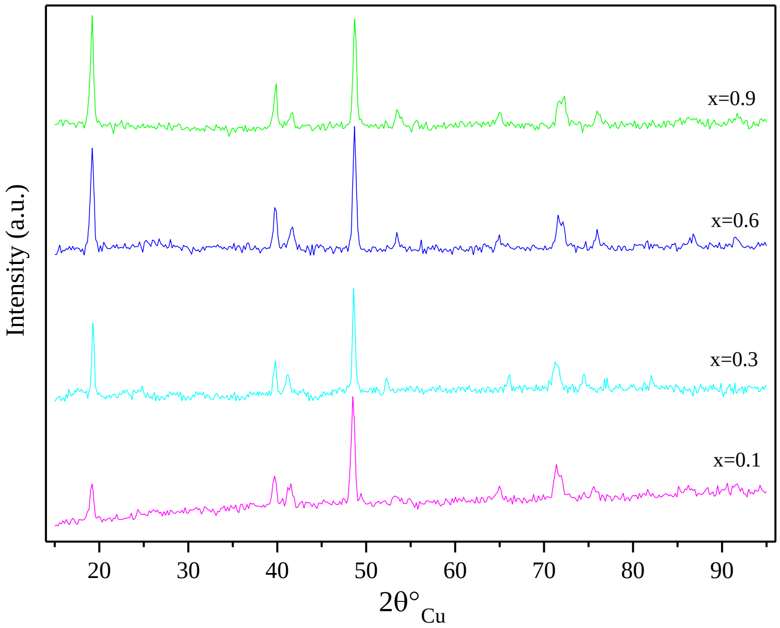

Fig. 66: XRD patterns of the $Li_xNi_{0.6}Mn_{0.2}Co_{0.15}Al_{0.025}Fe_{0.025}O_2$ phase (x=0.1; 0.3; 0.6; 0.9) chemically de-intercalated by NO_2BF_4 in acetonitrile and treated by DTA-TG from room temperature to 600°C in air The absence of any additives, such as PVDF or carbon black, that are necessary for preparing the electrodes, allowed us to record X-ray diffraction patterns of good quality and to determine then the lattice parameters by refining the structure.

The only difference that was observed by comparing the X-ray diffractograms is the continuous shift of the diffraction lines to higher diffraction angles. This suggests that a change in the lattice parameters occurred due to the temperature increase, which is most probably due to the loss of oxygen that is ensuring the cohesion of the lattice. The oxygen loss in the case of NMCAF de-intercalated phases is so low that no structural transition occurred.

Fig. 67 illustrates the variation of the lattice parameters ratio c_{hex}/a_{hex} as a function of the lithium composition. Whatever the amount of extracted lithium is, the c_{hex}/a_{hex} ratio remains above the critical value (~ 4.90) for which the structure becomes of a cubic symmetry [336]. This result confirms that NMCAF material keeps its initial structure α-$NaFeO_2$ (S.G.: R-3m) even at the de-intercalated state and at high temperatures up to 600°C.

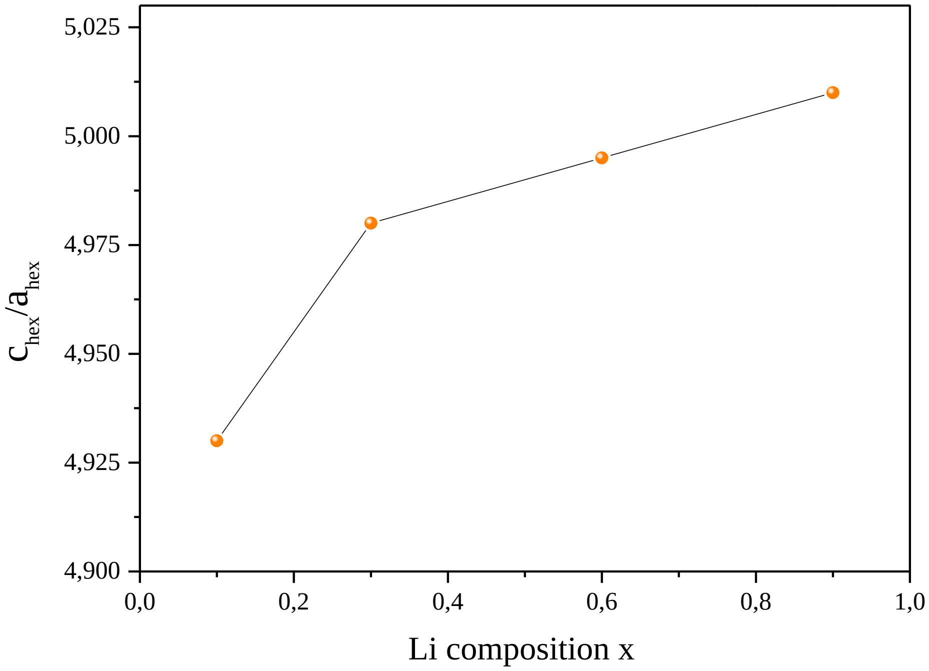

Fig. 67: Variation of the ratio c_{hex}/a_{hex} (deduced from XRD Rietveld refinement) of the phases $Li_xNi_{0.6}Mn_{0.2}Co_{0.15}Al_{0.025}Fe_{0.025}O_2$ (x=0.1; 0.3; 0.6; 0.9) chemically de-intercalated by NO_2BF_4 in acetonitrile and treated by DTA-TG from room temperature to 600°C in air

- $LixNi_{0.6}Mn_{0.2}Co_{0.2}O_2$

As shown in Fig. 68, one can see that the NMC (3:1:1) de-intercalated phases underwent structural changes at high temperature. In fact, there is no conservation of the original structure as we notice almost a disappearance of the peak (003) especially for low lithium composition. This suggests the loss of the structure crystallinity and the deviation from the R-3m space group of the starting material.

The thermal study by DTA-TG followed by ex-situ XRD allow us to show the positive effect of the double substitution with Al and Fe on the pristine NMC (3:1:1) material. Indeed, the substitution of 5% of cobalt contributed to inhibit the structural transitions and to significantly improve the thermal stability.

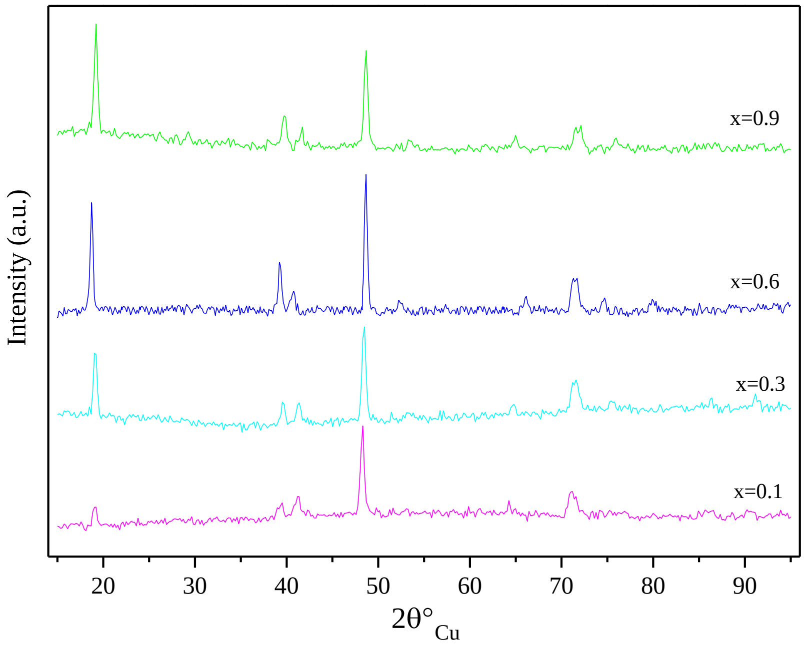

Fig. 68: XRD patterns of the $LixNi_{0.6}Mn_{0.2}Co_{0.2}O_2$ phase (x=0.1; 0.3; 0.6; 0.9) chemically de-intercalated by NO_2BF_4 in acetonitrile and treated by DTA-TG from room temperature to 600°C in air atmosphere

When substituting the pristine material with Al and Fe, the ordering of the transition metal cations is modified and prevents ionic and electronic rearrangements which normally happen during the material oxidation or when the de-intercalated phases are exposed to a temperature increase. Therefore, improved structural stability even at high temperatures up to 600°C is due to the presence of Al^{3+} and Fe^{3+} in addition to Mn^{4+} ions that are electrochemically inactive but have a great contribution to the stability of the de-intercalated phase during cycling and during temperature increase.

Summary and outlook

The layered transition metal oxides of NMC type are considered promising positive electrode materials for LIBs and alternatives to the conventional $LiCoO_2$ positive electrode.

The achieved work throughout this thesis had as main objective the optimization of NMC material both in terms of electrochemical performance and thermal stability via a cationic substitution.
As first step, the impact of different synthesis parameters on the purity, the morphology and the electrochemical performance of the studied materials was highlighted (Ch. IV). It turned out that in order to obtain pure and well crystallized compounds and to adjust the average particle size and size distribution, the following conditions are necessary:

- Preparation by self-combustion synthesis method using metal nitrates and sucrose considered as fuel.
- Annealing process, directly after synthesis, in air at a temperature of 900°C for one hour.
- Preference of the nickel rich phase with the composition $LiNi_{0.6}Mn_{0.2}Co_{0.2}O_2$: NMC (3:1:1).

Subsequently, substitution of cobalt by aluminum and / or iron was carried out in an attempt to further optimize the starting compound NMC (3.1.1) (Ch. V). The studied materials were NMCA ($LiNi_{0.6}Mn_{0.2}Co_{0.15}Al_{0.05}O_2$), NMCF ($LiNi_{0.6}Mn_{0.2}Co_{0.15}Fe_{0.05}O_2$) and NMCAF ($LiNi_{0.6}Mn_{0.2}Co_{0.15}Al_{0.025}Fe_{0.025}O_2$).

X-ray diffraction was carried out as first step and showed that all the obtained materials belong to α-$NaFeO_2$-type structure (space group R-3m) with hexagonal ordering. Rietveld refinement analysis of the XRD patterns revealed a very low Li^+ / Ni^{2+} exchange between the MO_6 sheets and the interlayer space (cationic mixing) for the double substituted material NMCAF (5%) compared to the mono-substituted materials NMCF (8%), NMCA (9%) and the non-substituted material (13%) suggesting a higher structural stabilization for the double substituted compound. Galvanostatic cycling indicates improved electrochemical performance, good cycling stability and higher reversible capacity preferentially for NMCAF (190 mAh g^{-1}), NMCF (165 mAh g^{-1}), NMCA (162 mAh g^{-1}) then NMC (156 mAh g^{-1}). Cycling at C/20 rate displayed capacity retentions after 10 cycles of about 93% for NMCAF, around 89% for NMCF and NMCA and 88% for NMC (3:1:1).

Then a more detailed comparison between NMC and NMCAF was compiled to better understand the phenomena behind the improvement of the electrochemical behavior of the double substituted cathode (Ch. VI).

In order to accurately follow the intercalation/de-intercalation reaction of lithium ions and to determine the chemical diffusion coefficient D_{Li+}, both GITT and EIS studies were performed and D_{Li+} for the double substituted material was calculated to be 4.4 10^{-11} cm^2 s^{-1}, about two orders of magnitude higher than that of the NMC (3:1:1) (3.9 10^{-13} cm^2 s^{-1}).

EPR spectroscopy showed that the double substitution with Al and Fe influenced significantly the EPR spectrum of the non-substituted NMC (3:1:1), especially the Ni^{2+} line, which was attributed to a redistribution of the Ni ions in the layered structure, and might be the reason for the reduced cation mixing in the NMCAF.

On the other hand, considering the great concern given to safety aspects of active electrode materials for LIBs, it was necessary to investigate the thermal and structural properties of the NMCAF and NMC (3:1:1) phases chemically de-intercalated by mixing a non-aqueous NO_2BF_4 / acetonitrile solution and the active materials. The absence of any additives, such as PVDF or carbon black, that are necessary for preparing the electrodes, allowed obtaining results related to the active materials only without contributions of the electrolyte and additives.

Structural analysis of the chemically de-intercalated phases showed that the lattice volume varied slightly especially for the double substituted material (approximately 0.010% for NMCAF and 0.013% for NMC (3:1:1)) which is very important from applications point of view and in terms of safety as the good cycleability of the cell depends on the volume change of the material.

Emphasis on the safety aspect of the two materials was put through a detailed study of their thermal stability during the lithium ions de-intercalation process. According to the TGA analysis, a higher mass loss was observed for $Li_xNi_{0.6}Mn_{0.2}Co_{0.2}O_2$ phases than for $Li_xNi_{0.6}Mn_{0.2}Co_{0.15}Al_{0.025}Fe_{0.025}O_2$ ($0.1<x<0.9$) which was assigned to the stabilizing effect of the double substitution with Al and Fe.

The thermal study by DTA-TG followed by ex-situ XRD enabled demonstrating the positive effect of the double substitution with Al and Fe on the pristine NMC (3:1:1) material. Indeed, the substitution of 5% of cobalt contributed to inhibit the structural transitions and to significantly improve the thermal stability.

Eventually this thesis remains a subject rich in perspectives. Indeed, it is possible to:

- Investigate novel NMC type materials obtained by simultaneous double cationic substitution of cobalt with other metals such as Mg, Cr, Be and/or Ga and assess their electrochemical performance,
- Use the second approach which is surface modification by coating with metal oxides such as ZrO_2, Al_2O_3, TiO_2, B_2O_3 or carbon to improve the structural stability and the electrochemical performance of the pristine cathode material for LIBs,
- Evaluate the electrochemical performance of batteries at higher temperature 60 °C for example and for longer periods of cycling that can reach 500 cycles.

-

List of Original Publications

[1] **W. El Mofid**, S. Ivanov, A. Konkin, A. Bund, "*A high performance layered transition metal oxide cathode material obtained by simultaneous aluminum and iron cationic substitution*", J. Power Sources 268 (**2014**) 414-422.

[2] **W. El Mofid**, S. Ivanov, A. Bund, "*A Novel Al and Fe Double Substituted NMC Positive Electrode Material for Lithium Ion Batteries*", 65th annual meeting of the international society of electrochemistry, Lausanne-Switzerland, 31 August - 5 September **2014** (Poster).

[3] H. Wulfmeier, D. Gao, D. Albrecht, H. Fritze, **W. El Mofid**, S. Ivanov, A. Bund, "*Thermodynamic Investigation of NMC-based Cathode Materials Performed by Thin-Film Calorimetry*", Materials Science Engineering conference (MSE 2014), Darmstadt-Germany, 23-25 September **2014** (Oral).

[4] **W. El Mofid**, S. Ivanov, A. Bund, "*The Effect of Al and Fe Substitution on the Structure and the Electrochemical Properties of NMC Type Positive Electrode Materials for Lithium Ion Batteries*", 226th meeting of the electrochemical society, Cancun-Mexico, 5-9 October **2014** (Oral).

[5] **W. El Mofid**, S. Ivanov, A. Bund, "*Effect of synthesis conditions and composition modification on the structural and electrochemical properties of layered transition metal oxide cathode materials*", 2nd International Renewable and Sustainable Energy Conference (IRSEC'14), Ouarzazate-Morocco, 17-19 October **2014** (Oral).

[6] **W. El Mofid**, A. Bund, "A Novel environmentally Benign Positive Electrode Material with Improved Energy Density for Lithium Ion Batteries", International Conference on Advanced Engineering Materials, NewDelhi- India, 07-08 February **2015** (Oral).

[7] **W. El Mofid**, S. Ivanov, A. Bund, D. Goers, S. Rentenberger, "Inhibition of Al/Cu Contact Corrosion in Lithium Ion Batteries", 227th meeting of the electrochemical society, Chicago-USA, 24-28 May **2015** (Oral).

[8] H. Wulfmeier, A.Omelcenko, D. Albrecht, D. Klimm, **W. El Mofid**, M. Strafela, S. Ulrich, A. Bund and H.Fritze, “Thermal Stability of Materials for Thin-Film Electrochemical Cells Investigated by Thin-Film Calorimetry”, Cambridge journals MRS advances 1 (**2016**) 1043-1049.

[9] **W. El Mofid**, S. Ivanov, A. Bund, “*Study of the Structural and Thermal Stabilities of Chemically Deintercalated Phases of NMC Type Positive Electrode Materials for Lithium Ion Batteries”,* 229th meeting of the electrochemical society Honolulu, Hawaii-USA, 2-7 October **2016** (Oral).

Bibliography

[1] A. De Guibert, L'actualité chimique 3 (1998) 15-17.

[2] M. B. Armand, Materials for advanced Batteries (1980) 145-161.

[3] A. K. Shukla, N. R. Avery and B. C. Muddle, “Future cars: The electric option”, Current Science, 77 (1999) 1141–1146.

[4] Challenge Bidendum, “Batteries and super-capacitors : Roadmap to market”, Tech. Rep., Michelin, 2007.

[5] B. G. Silbernagel, M. S. Whittingham, Mat. Res. Bull., 11 (1976) 29-36.

[6] M. S. Whittingham, Science, 192 (1976) 1126–1127.

[7] R. Yazami, Ph. Touzain, J. Power Sources 9 (1983) 365-371

[8] JEC Batt. Newsletter, 2 (1994) 31.

[9] M. Broussely, L'actualité chimique 25 (1994) 1-2.

[10] K. Mizushima, P. C. Jones, P. J. Wiseman and J. B. Goodenough, Mat. Res. Bull. 15 (1980) 783.

[11] C. Zhu, C. Yang, W. Yang, C. Hsieh, H. Ysai, Y. Chen, J. Alloys Compd. 496 (2010) 703–709.

[12] J. Shu, M. Shui, F. Huang, Y. Ren, Q. Wang, D. Xu, L. Hou, J. Phys. Chem. C 114 (2010) 3323–3328.

[13] J.N. Reimers, J.R. Dahn, LixCoO2, J. Electrochem. Soc. 139 (1992) 2091-2097.

[14] M.S. Whittingham, Chem. Rev. 104 (2004) 4271-4301.

[15] JR Dahn, EW Fuller, M. Obrovac, U. von Sacken, Solid State Ionics 69 (1994) 265-270.

[16] R. Stoyanova, E. Zhecheva, L. Zarkova, Solid State Ion. 73 (1994) 233-240.

[17] Masaya Takahashi, Shinichi Tobishima, Koji Takei, Yoji Sakurai, Solid State Ion. 148 (2002) 283–289.

[18] D. Zane, M. Carewska, S. Scaccia, F. Cardellini, and P. P. Prosini, Electrochim. Acta, 49 (2004) 4259–4271.

[19] P. P. Prosini, D. Zane, and M. Pasquali, Electrochim. Acta, 46 (2001) 3517–3523.

[20] S.-T.Myung, S. Komaba, N. Hirosaki, H. Yashiro, and N.Kumagai, Electrochim. Acta 49 (2004) 4213–4222.

[21] H.C. Shin, S.B. Park, H. Jang, K.Y. Chung, W.I.Cho, C.S. Kim, and B.W. Cho, Electrochim. Acta 53 (2008) 946–7951.

[22] Y.-H. Nien and J.-S. Chen, ECS Meeting Abstracts 702 (2007) 647.

[23] J. Li, R. Klöpsch, M.C. Stan, S. Nowak, M. Kunze, M. Winter, S. Passerini, J. Power Sources, 196 (2011) 4821–4825.

[24] Naoaki Yabuuchi, Tsutomu Ohzuku, J. Power Sources, 119–121 (2003) 171–174.

[25] K. M. Shaju, P. G. Bruce, Advanced materials, 18 (2006) 2330–2334.

[26] Yang-Kook Sun, Seung-Taek Myung, Byung-Chun Park, Jai Prakash, Ilias Belharouak, Khalil Amine, Nature Materials 8 (2009) 320-324.

[27] Ismael Saadoune, Mohamed Labrini, Mustapha Yahya, Abdelmajid Almaggoussi, Helmut Ehrenberg, Electrochim. Acta, 55 (2010) 5180-5185.

[28] M.-H. Lee, Y.-J. Kang, S.-T. Myung, Y.-K. Sun, 50 (2004) 939-948.

[29] Abdelfattah Mahmoud, Mayumi Yoshita, Ismael Saadoune, Joachim Broetz, Kenjiro Fujimoto, Shigeru Ito, 47 (2012) 1936-1941,

[30] T. Ohzuku, Y. Makimura, Chem. Lett. 30 (2001) 642-643.

[31] I. Belharouak, Y.K. Sun, J. Liu, K. Amine, J. Power Sources 123 (2003) 247-252.

[32] S. Patoux, M.M. Doeff, Electrochem. Commun. 6 (2004) 767-772.

[33] B.J. Hwang, Y.W. Tsai, D. Carlier, Chem. Mater. 15 (2003) 3676-3682.

[34] T. Ohzuku, Y. Makimura, Chem. Letters 7 (2001) 642-646.

[35] Y. Chen, G.X. Wang, K. Konstantinov, H.K. Liu, S.X. Dou, J. Power Sources 119–121 (2003) 184–188.

[36] X. Zhang, W. Jiang, A. Mauger, F. Gendron, C. Julien, J. Power Sources 195 (2010) 1292-1301.

[37] R. Sathiyamoorthi, P. Shakkthivel, S. Ramalakshmi, Yong-Gun Shul, J. Power Sources 171 (2007) 922-927.

[38] B.V.R. Chowdari, G.V. Subba Rao, S.Y. Chow, Solid State Ionics 140 (2001) 55-62.

[39] C. Pouillerie, L. Croguennec, C. Delmas, Solid State Ionics 132 (2000) 15-29.

[40] T. Ohzuku, A. Ueda, M. Kouguchi, J. Electrochem. Soc. 142 (1995) 4033-4039.

[41] M.Y. Song, R. Lee, I.H. Kwon, Solid State Ionics 156 (2003) 319-328.

[42] Y. Nishida, K. Nakane, T. Satoh, J. Power Sources 68 (1997) 561-564.

[43] C. Delmas, G. Prado, A. Rougier, E. Suard, L. Fournès, Solid State Ionics 135 (2000) 71-79.

[44] M. Yoshio, Y. Todorov, K. Yamato, H. Noguchi, J. Itoh, M. Okada, T. Mouri, J. Power Sources 74 (1998) 46-53.

[45] Haiqiang Liu, Ruiyuan Tian, Yi Jiang, Xinghua Tan, Jiankun Chen, Lina Zhang, Yanjun Guo, Hanfu Wang, Lianfeng Sun, Weiguo Chu, Electrochim Acta, 180 (2015) 138-146.

[46] Dao-Lai Fang, Jun-Chao Li, Xin Liu, Peng-Fei Huang, Tian-Ran Xu, Ming-Chuan Qian, Cui-Hong Zheng, Journal of Alloys and Compounds, 640 (2015) 82-89.

[47] G. Li, H. Ikuta, T. Uchida, M. Wakihara, J. Electrochem. Soc. 143 (1996) 178-182.

[48] S.H. Wu, H.J. Su, Mater. Chem. Phys. 78 (2002) 189-195.

[49] K.M. Shaju, G.V.S. Rao, B.V.R. Chowdari, Solid State Ionics 148 (2002) 343-350.

[50] H.J. Bang, V.S. Donepudi, J. Prakash, Electrochim. Acta 48 (2002) 443-451.

[51] B.H. Kim, Y.K. Choi, Y.H. Choa, Solid State Ionics 158 (2003) 281-285.

[52] M. Yoshio, Y. Xia, N. Kumada, S. Ma, J. Power Sources 101 (2001) 79-85.

[53] M. Hosoya, H. Ikuta, M. Wakihara, Solid State Ionics 111 (1998) 153-159.

[54] S. Komaba, K. Oikawa, S.T. Myung, N. Kumagai, T. Kamiyama, Solid State Ionics 149 (2002) 47-52.

[55] B.J. Hwang, R. Santhanam, D.G. Liu, Y.W. Tsai, J. Power Sources 102 (2001) 326-331.

[56] D. Song, H. Ikuta, T. Uchida, M. Wakihara, Solid State Ionics 117 (1999) 151-156.

[57] I.S. Jeong, J.U. Kim, H.B. Gu, J. Power Sources 102 (2001) 55-59.

[58] Li H, Chen G, Zhang B, Xu J, Solid State Commun 146 (2008) 115–120.

[59] Y.S. Meng, Y.W. Wu, B.-J. Hwang, Y. Li, G. Ceder, J. Electrochem. Soc. 151 (2004) A1134- A1140.

[60] Zhang B, Li L, Zheng J, J. Alloy. Compd. 520 (2012) 190-194.

[61] Idemoto Y, Kitamura N, Ueki K, Vogel SC, Uchimoto Y, J. Electrochem. Soc. 159 (2012) A673-A677.

[62] Luo W, Zhou F, Zhao X, Lu Z, Li X, Dahn JR, Chem. Mater. 22 (2009) 1164-1172.

[63] T. Ohzuku, A. Ueda, N. Nagayama, Y. Iwakoski, H. Komori, Electrochim. Acta 38 (1993) 1159-1167.

[64] Arun Kumar Varanasi & Arghya Bhowmik & Tanmay Sarkar & Umesh V. Waghmare & Mridula Dixit Bharadwaj, Ionics 20 (2014) 315–321.

[65] Lithium Statistics and Information U.S. Geological Survey (2015) 201401280924315001.

[66] Tarascon, J. M., Nature Chemistry 2 (2010) 510.

[67] US Geological Survey; ID 268789.

[68] JASKULA, B.W., Lithium, U.S. Geological Survey Minerals Yearbook (2008) 44.4-44.9.

[69] http://www.ccfa.fr/Le-marche-des-batteries-lithium,119269.

[70] Stefan Wimmelbücker, Batterieproduktion, 1. April 2014.

[71] Sächsische Zeitung, 15./16. November 2014, S.1.

[72] http://www.statista.com/statistics/235323/lithium-batteries-top-manufacturers.

[73] Roland Berger; ID 235316.

[74] Citibank; ID 309562.

[75] http://www.technavio.com/report/global-li-ion-battery-market-for-consumer-electronics-2015-2019.

[76] http://www.marketresearch.com/product/sample-8323376.pdf.

[77]http://www.avem.fr/actualite-etude-5-fabricants-se-partageront-70-du-marche-des-batteries-li-ion-a-l-horizon-2015.

[78] http://www.technavio.com/report/global-li-ion-battery-market-for-evs-2015-2019.

[79] Citibank; ID 309564.

[80] PwC; ID 304920.

[81] K. Xu, Chemical Reviews, 104 (2004) 4303.

[82] Ellis, B.L., Lee, K.T., and Nazar, L.F., Chem. Mater., 22 (2010) 691–714.

[83] Armand, M. et al., Nat. Mater., 8 (2009) 120–125.

[84] Nazri, G. and Pistoia, G., Lithium Batteries: Science and Technology, Springer, 2009.

[85] Tarascon, J.M. and M. Armand, Nature, 414 (2001) 359–367.

[86] Nishi, Y., J. Power Sources 100 (2001) 101–106.

[87] Scrosati, J. Electrochem. Soc. 139 (1992) 2776–2781.

[88] Tirado, J.L., Materials Science and Engineering Reports 40 (2003) 103–136.

[89] Broussely, M. and G. Archdale, J. Power Sources 136 (2004) 386–394.

[90] Winter, M., J.O. Besenhard, M.E. Spahr and P. Novák, Advanced Materials 10 (1998) 725–763.

[91] P. Poizot, S. Laruelle, S. Grugeon, L. Dupont , J. M. Tarascon, Nature 407 (2000) 496.

[92] P. Poizot, S. Laruelle, S. Grugeon, L. Dupont, J. M. Tarascon, J. Power Sources 235 (2001) 97-98.

[93] P. Poizot, S. Laruelle, S. Grugeon, L. Dupont, B. Beaudoin, J. M. Tarascon, C.R. Acad. Sci. 3 (2000) 681.

[94] Y. M. Kang, K. T. Kim, J. H. Kim, H .S. Kim, P. S. Lee, J. Y. Lee, H. K. Liu, S.X. Dou, J. Power Sources, 133 (2004) 252.

[95] P. C. Wang, H. P. Ding, T. Bark, C. H. Chen, Electrochim Acta, 52 (2007) 6650.

[96] H. J. Bang, S. Kim, J. Prakash, J. Power Sources, 45 (2001) 92.

[97] J. O. Besenhard, P. Komenda, A. Paxinos, E. Wudy, M. Josowicz, Solid State Ionics., 823 (1986) 18-19.

[98] W. J. Weydanz, M. Wohlfahrt-Mehrens, R. A. Huggins, J. Power Sources, 237 (1999) 81-82.

[99] D. Fauteux, R. Koksbang, Journal Applied Electrochemistry, 23 (1993) 1

[100] L.F. Nazar, O. Crosnier, Anodes and composite anode: an overview, in Lithium batteries, ed. Kluwer, New York (2004)

[101] L.Y. Beaulieu, K.W. Eberman, R.L. Turner, L.J. Krause, J.R. Dahn, Electrochemical and Solid State Letter, 4 (2001) A137.

[102] J.T. Vaughey, J. O'hara, M.M. Thackeray, Electrochemical and Solid State Letters, 3 (2000)13.

[103] J. Yang, Y. Takeda, N. Imanishi, T. Ichikawa, O. Yamamoto, Solid State Ionics., 135 (2000) 175.

[104] H. Li, X. Huang, L. Chen, Z. Wu, Y. Liang, Electrochem. Solid State Lett. 2 (1999) 547.

[105] H. Li, X.J. Huang, L.Q. Chen, Z.G. Wu, Y. Liang, Electrochemical Solid-State Letters. 2 (1999) 547.

[106] Z.X. Liao, F.Z. Ma, J.H. Hu, Electrochemistry Communications, 5 (2003) 657.

[107] H. Guo, H. Zhao, C. Yin et W. Qiu, J. Alloys Compd., 426 (2006) 277.

[108] T. Ohzuku, A. Ueda, and N. Yamamoto, J. Electrochem. Soc., 142 (1995) 1431.

[109] A. Van Thournout, L. Aldon, M. Womes, B. Ducourant, J. Olivier- Fourcade, C. Tessier, S. Levasseur, J. Power Sources, 174 (2007) 1270.

[110] Y. Liu, K. Horikawa, M. Fujiyoshi, T. Matsumura, N. Imanishi, Y. Takeda, Solid State Ionics., 172 (2004) 69.

[111] A. N. Jansen, A. J. Kahaian, K. D. Kepler, P. A. Nelson, K. Amine, D. W. Dees, D. R. Vissers, M. M. Thackeray, J. Power Sources, 902 (1999) 81-82.

[112] M. E. A. y. d. Dompablo, E. Moran, A. Varez, F. Garcia-Alvarado, Material Research Bulletin, 32 (1997) 993.

[113] D. Deng, M. G. Kim, J. Y. Lee, J. Cho, Energy Environment Sciety. 2 (2009), 818.

[114] David Young, Alan Ransil, Ruhul Amin, Zheng Li, Yet-Ming Chiang, Advanced energy materials 3 (2013) 1125–1129

[115] P. G. Bruce, B. Scrosati, J. M. Tarascon, Angew. Chemie, 47 (2008) 2930.

[116] I.A. Courtney, J.S. Tse, O. Mao, J. Hafner, J.R. Dahn, Physical Review, B, 58 (1998) 15583.

[117] J. Chouvin, J. Olivier-Fourcade, J.-C. Jumas, B. Simon, O. Godiveau, Chemical Physical Letters, 308 (1999) 413.

[118] I. A. Courtney, J. S. Tse, O. Mao, J. Hafner, J. R. Dahn, Physical Review. B, 58 (1998) 15583.

[119] M. Chamas, P-E. Lippens, J-C. Jumas, K. Boukerma, R. Dedryvère, D. Gonbeau, J. Hassoun, S. Panero, B. Scrosati, J. Power Sources, 196 (2011) 7011–7015.

[120] S. Naille, C.M. Ionica-Bousquet, F. Robert, F. Morato, P.-E. Lippens, J. Olivier-Fourcade, J. Power Sources, 174 (2007) 1091–1094.

[121] H. Guo, H. zhao, X. JIA, W. Qiu, R. Metals, 25 (2006) 369-373.

[122] A. Finke, P. Poizot, C. Guery, J. M. Tarascon, Journal Electrochemical Society, 152 (2005) A2364–A2368.

[123] M. Z. Xue, Z. W. Fu, Solid State Ionics, 177 (2006) 1501–1507.

[124] J. T Vaughey, M. M. Thackeray; D. Shin, C. J. Wolverton, Electrochemical Society, 156 (2009) A536–A540.

[125] M. Nishijima, Y. Takeda, N. Imanishi, O. Yamamoto, J. Solid State Chem., 113 (1994) 205.

[126] M. Nishijima, N. Tadokoro, Y. Takeda, N. Imanishi, O. Yamamoto, J. Electrochem. Soc., 141 (1994) 2966.

[127] M. Nishijima, T. Kagohashi, M. Imanishi, Y. Takeda, O. Yamamoto, S. Kondo, Solid State Ionics., 83 (1996) 107.

[128] T. Shodai, S. Okada, S. I. Tobishima, J. I. Yamaki, Solid State Ionics., 86-88 (1996) 785.

[129] M. Nishijima, T. Kagohashi, Y. Takeda, M. Imanishi, O. Yamamoto, J. Power Sources, 68 (1997) 510.

[130] D.C.S. Souza, V. Pralong, A.J. Jacobson, L.F. Nazar, Science, 296 (2002) 2012.

[131] V. Pralong, D.C.S. Souza, K.T. Leung, L.F. Nazar, Electrochem Commun., 4 (2002) 516.

[132] D.C. C. Saliva, O. Crosnier, G. Ouvrard, J. Greedan, A. S. Sefat, L. F. Nazar, Electrochem. Solid State Lett., 6 (2003) A162.

[133] O. Crosnier, C. Mounsey, P. Subramanya Herle, N. Taylor, L.F. Nazar, Chem. Mater., 15 (2003) 4890.

[134] M. V. V. M. Satya Kishore, U. V. Varadaraju, J. Power Sources, 156 (2006) 594.

[135] F. Gillot, M.P. Bichat, F. Favier, M. Morcrette, M.L. Doublet, L. Monconduit, Electrochim Acta, 49 (2004) 2325.

[136] D. Guyomard, C. Sigala, A. Le Gal La Salle, Y. Piffard, J. Power Sources, 68 (1997) 692.

[137] S. Denis, E. Beudrin, M. Touboul, J. M, Tarascon, J. Electrochem., 144 (1997) 4099.

[138] A. F. fuentes, L. Trevino, A. M. la Cruz, L. M. Torres-Martinez, J. Power Sources 81-82 (1999) 264.

[139] Y. Piffard, F. Leroux, D. Guyomard, J. L. Mansot, M. Tournoux, J. Power Sources, 68 (1997) 698.

[140] E. Peled, J. Electrochem. Soc. 126 (1979) 2047-2051.

[141] N. Munichandraiah, L. G. Scanlon, R. A. Marsh, J. Power Sources, 72 (1998) 203.

[142] D. Aurbach, E. Zinigrad, Y. Cohen et H. Teller, Solid State Ion., 148 (2002) 405.

[143] Y. Yamada, Y. Iriyama, T. Abe and Z. Ogumi, Langmuir, 21 (2009) 25.

[144] K. Xu, Chemical Reviews 104 (2004) 4303.

[145] M. Handa, M. Suzuki, J. Suzuki, H. Kanematsu, Y. Sasaki, Electrochemical and Solid-State Letters, 2 (1999) 60.

[146] M. Eberwein, A. Schmid, M. Schmidt, M. Zabel, T. Burgemeister, J. Barthel, W. Kunz, H.J. Gores, Journal of the Electrochemical Society 150 (2003) A994.

[147] M. Schmidt, U. Heider, A. Kuehner, R. Oesten, M. Jungnitz, N. Ignat'ev, P. Sartori, J. Power Sources 557 (2001) 97-98.

[148] J.S. Gnanaraj, M.D. Levi, Y. Gofer, D. Aurbach, M. Schmidt, Journal of the Electrochemical Society 150 (2003) A445.

[149] J.S. Gnanaraj, E. Zinigrad, L. Asraf, M. Sprecher, H.E. Gottlieb, W. Geissler, M. Schmidt and D. Aurbach, J. Electrochem. Soci., 150 (2003) A1533.

[150] J. Barthel, R. Buestrich, E. Carl, H.J. Gores, Journal of the Electrochemical Society 143 (1996) 3572.

[151] J. Barthel, A. Schmid, H.J. Gores, Journal of the Electrochemical Society 147 (2000) 21.

[152] W. Xu, C.A. Angell, Electrochemical and Solid-State Letters 4 (2001) E1.

[153] T.J. Barbarich, P.F. Driscoll, S. Izquierdo, L.N. Zakharov, C.D. Incarvito, A. L. Rheingold, Inorg. Chem. 43 (2004) 7764-7773.

[154] T.J. Barbarich, P.F. Driscoll, Electrochemical and Solid-State Letters 6 (2003) A113.

[155] S.S. Zhang, J Power Sources 162 (2006) 1379.

[156] R. Oesten, U. Heider, M. Schmidt, Solid State Ionics 148 (2002) 391.

[157] D. Aurbach, K. Gamolsky, B. Markovsky, Y. Gofer, M. Schmidt, U. Heider, Electrochimica Acta 47 (2002) 1423.

[158] O. Matsuoka, A. Hiwara, T. Omi, M. Toriida, T. Hayashi, C. Tanaka, Y. Saito, T. Ishida, H. Tan, S.S. Ono, S. Yamamoto, J. Power Sources 108 (2002) 128.

[159] S.S. Zhang, K. Xu, T.R. Jow, Electrochimica Acta 51 (2006) 1636.

[160] H. Buqa, A. Wursig, J. Vetter, M.E. Spahr, F. Krumeich, P. Novak, J. Power Sources 153 (2006) 385.

[161] M. Lu, H. Cheng, Y. Yang, Electrochimica Acta 53 (2008) 3539.

[162] L. El Ouatani, R. Dedryvere, C. Siret, P. Biensan, D. Gonbeau, Journal of the Electrochemical Society 156 (2009) A468.

[163] L. El Ouatani, R. Dedryvere, C. Siret, P. Biensan, S. Reynaud, P. Iratcabal, D. Gonbeau, Journal of the Electrochemical Society 156 (2009) A103.

[164] H. Ota, Y. Sakata, A. Inoue, S. Yamaguchi, Journal of the Electrochemical Society 151 (2004) A1659.

[165] M. Itagaki, S. Yotsuda, N. Kobari, K. Watanabe, S. Kinoshita, M. Ue, Electrochimica Acta 51 (2006) 1629.

[166] M. Armand, "Materials for Advanced Batteries", Eds. D. W. Murphy, J. Broadhead, B. C. H. Steele, Plenum Press, New-York, (1980) 145.

[167] S. Panero, B. Scrosati, 90 (2000) 13.

[168] Y.J. Wang, D. Kim, Electrochimica Acta 52 (2007) 3181.

[169] V. Gentili, S. Panero, P. Reale, B. Scrosati, J. Power Sources 170 (2007) 185.

[170] P. Raghavan, X.H. Zhao, J.K. Kim, J. Manuel, G.S. Chauhan, J.H. Ahn, C. Nah, Electrochimica Acta 54 (2008) 228.

[171] Z.H. Li, H.P. Zhang, P. Zhang, Y.P. Wu, X.D. Zhou, Journal of Power Sources 184 (2008) 562.

[172] J.K. Kim, G. Cheruvally, X. Li, J.H. Ahn, K.W. Kim, H.J. Ahn, J. Power Sources 178 (2008) 815.

[173] R.Y. Miao, B.W. Liu, Z.Z. Zhu, Y. Liu, J.L. Li, X.D. Wang, Q.F. Li, J. Power Sources 184 (2008) 420.

[174] Z. Ren, K.N. Sun, Y.Y. Liu, X.L. Zhou, N.Q. Zhang, X.D. Zhu, Solid State Ionics 180 (2009) 693.

[175] Y.H. Ding, W. Di, Y. Jiang, F. Xu, Z.L. Long, F.M. Ren, P. Zhang, Ionics 15 (2009) 731.

[176] Z.Y. Cui, Y.Y. Xu, L.P. Zhu, J.Y. Wang, B.K. Zhu, Ionics 15 (2009) 469.

[177] Z. Ren, Y.Y. Liu, K.N. Sun, X.L. Zhou, N.Q. Zhang, Electrochimica Acta 54 (2009) 1888.

[178] P. Raghavan, X. Zhao, C. Shin, D.H. Baek, J.W. Choi, J. Manuel, M.Y. Heo, J.H. Ahn, C. Nah, J. Power Sources 195 (2010) 6088.

[179] A.I. Gopalan, P. Santhosh, K.M. Manesh, J.H. Nho, S.H. Kim, C.G. Hwang, K.P. Lee, Journal of Membrane Science 325 (2008) 683.

[180] J.W. Fergus, Journal of Power Sources 195 (2010) 4554.

[181] Z. Ogumi, T. Abe, S. Nakamura, M. Inaba, Solid State Ionics 121 (1999) 289.

[182] S.A. Forsyth, J.M. Pringle, D.R. MacFarlane, Australian Journal of Chemistry 57 (2004) 113.

[183] D.R. MacFarlane, M. Forsyth, P.C. Howlett, J.M. Pringle, J. Sun, G. Annat, W. Neil, E.I. Izgorodina, Accounts of Chemical Research 40 (2007) 1165.

[184] P. Hapiot, C. Lagrost, Chemical Reviews 108 (2008) 2238.

[185] D.R. MacFarlane, P. Meakin, J. Sun, N. Amini, M. Forsyth, Journal of Physical Chemistry B 103 (1999) 4164.

[186] H.H. Zheng, J.H. Qin, Y. Zhao, T. Abe, Z. Ogumi, Solid State Ionics 176 (2005) 2219.

[187] Linden, D., Reddy, T. B. Handbook of Batteries (3rd ed.), McGraw Hill, New York, 2002.

[188] Besenhard, J. O. (Ed.). Handbook of Battery Materials, Wiley-VCH, Weimheim, 1999.

[189] Berndt, D. Maintenance Free Batteries (3rd ed.), Research Studies Press Ltd., Taunton, Somerset, England, 2003.

[190] Bode, H. Lead–Acid Batteries, John Wiley, New York, 1977.

[191] Falk, S. U., Salkind, A. J. Alkaline Storage Batteries, John Wiley, New York, 1969.

[192] Brodd R. J., Friend, H. M., Nardi, J. C. (Eds.). Lithium Ion Battery Technology, ITEJEC Press, Brunswick, OH, 1995.

[193] Wakihara, M., Yamamoto, O. (Eds.). Lithium Ion Batteries, Fundamentals and Performance, Wiley-VCH, New York, 1998.

[194] Yoshino A., Chemical Industry 146 (1995) 870.

[195] Schalkwijk, W. A. V. (Ed.). Advances in Lithium Ion Batteries, Kluwer Academic, New York, 2002.

[196] Kinoshita, K., Yeo, R., Survey on Separators for Electrochemical Systems, LBNL, Berkeley CA, January 1985.

[197] Zhang, S.S, J. Power Sources 164 (2007) 351.

[198] Arora, P. and Zhang, Z., Chem. Rev., 104 (2004) 4419–4462.

[199] Boehnstedt, W. In Handbook of Battery Materials, J.O. Besenhard (Ed.), VCH Wiley, Amsterdam and New York, 1999.

[200] Spotnitz, R. In Handbook of Battery Materials, J.O. Besenhard (Ed.), VCH Wiley, Amsterdam and New York, 1999.

[201] Shirai, H., Spotnitz, R. In Lithium Ion Secondary Battery—Materials and Applications, Kozawa Yoshio, Nikkan Kogyo Shin-bun Eds. (1996) 91.

[202] Shirai, H., Spotnitz, R., Atsushi, A. Chemical Industry, Tokyo, Japan (1997) 48-47.

[203] Hiroshi, T. In The Latest Technologies of the New Secondary Battery Materials, Zempachi Ogumi (Ed.), CMC, 99.

[204] Hiroshi, T. In Advanced Technologies for Polymer Battery, Noboru Oyama (Ed.), CMC, 165.

[205] Koichi, K. In Advanced Technologies for Polymer Battery, Noboru Oyama (Eds.), CMC, 174.

[206] Kiyoshi, K. In Lithium Secondary Battery Technology for the 21st Century, Kiyoshi Kanamura (Ed.), CMC, 116.

[207] Bierenbaum, H.S., Isaacson, R.B., Druin, M.L., Plovan, S.G. Industrial and Engineering Chemistry Product Research and Development 2 (1974) 13.

[208] Fleming, R., Taskier, H. Prog. Batt. Solar Cells 9 (1990) 58.

[209] Hoffman, D., Fisher, H., Langford, E., Diwiggins, C. Prog. Batt Solar Cells, JEC Press, Inc., Cleveland, OH, 9 (1990) 48.

[210] Callahan, R.W., Nguyen, K.V., McLean, J.G., Propost, J., Hoffman, D.K. Proceedings of the 10th International Seminar on Primary and Secondary Battery Technology and Application, Fort Lauderdale, Florida Educational Seminars (1993).

[211] Geiger, M., Callahan, R.W., Diwiggins, C.F., Fisher, H.M., Hoffman, D.K., Yu, W.C., Abraham, K.M., Jillson, M.H., Nguyen, T.H. The Eleventh International Seminar on Primary and Secondary Battery Technology and Application, Fort Lauderdale, FL, Florida Educational Seminars (1994).

[212] Spotnitz, R., Ferebee, M., Callahan, R.W., Nguyen, K., Yu, W.C., Geiger, M., Dwiggens, C., Fischer, H., Hoffman, D. Proceedings of the 12th International Seminar on Primary and Secondary battery Technology and Applications, Fort Lauderdale, FL, Florida Educational Seminars (1995).

[213] Yu, W.C., Callahan, R.W., Diwiggins, C.F., Fischer, H.M., Geiger, M.W., Schell, W.J., North America Membrane Society Conference, Breckenridge (1994).

[214] Hoffman, D.K., Abraham, K.M. Proceedings of the Fifth International Seminar on Lithium Battery Technology and Applications, Deerfield Beach, FL, Florida Educational Seminars (1991).

[215] USABC, “Development of low cost separators for lithium-ion batteries,” RFPI 2001.

[216] ASTM D5947–96, “Standard Test Methods for Physical Dimensions of Solid Plastics Specimens,” ASTM International.

[217] ASTM D2103, “Standard Specification for Polyethylene Film and Sheeting,” ASTM International.

[218] ASTM D726, “Standard Test Methods for Identification of Fibers in Textiles,”ASTM International.

[219] ASTM E128–99, “Standard test method for Maximum Pore Diameter and Permeability of Rigid Porous Filters for Laboratory Use,” ASTM International.

[220] ASTM D1204, “Standard Test methods for Linear Dimensional Changes of Non-rigid Thermoplastic Sheeting or Film at Elevated Temperatures,” ASTM International.

[221] M. S. Whittingham, Chemical Reviews 104 (2004) 4271-4301.

[222] T. Lee, K. Cho, J. Oh, D. Shin, J. Power Sources, 174 (2007) 394.

[223] O. Tsutomu and U. Atsushi, Journal of the Electrochemical Society, 141 (1994) 2972-2977.

[224] J. Zhou and P. H. L. Notten, J. Power Sources, 177 (2008) 553-560.

[225] R. Kanno, H. Kubo, Y. Kawamoto, T. Kamyamia, F. Izumi, Y. Takeda and M. Takano, Journal of Solid State Chemistry 110 (1994) 216.

[226] A. Rougier, P. Gravereau and C. Delmas, Journal of the Electrochemical Society, 143 (1996) 1168.

[227] J. R. Dahn, E. W. Fuller, M. Obrovac, U. Von Sacken, Solid State Ionics, 69 (1994) 265.

[228] T. Ohzuku, A. Ueda and M. Konguchi, Journal of the Electrochemical Society, 142 (1995) 4033.

[229] H. J. Orman and P. J. Wiseman, Acta Crystallographica Section C40 (1984) 12–14.

[230] C. Delmas, C. Fouassier and P. Hagenmüller, Physica B, 99 (1980) 81.

[231] Yang Shao-Horn, Laurence Croguennec, Claude Delmas, E. Chris Nelson and Michael A. O'Keefe, Nature Materials 2 (2003) 464–467.

[232] R. Kanno , Encyclopedia of Electrochemical Power Sources (2009) 297–306.

[233] J. B. Goodenough, D. G. Wickham, and W. J. Croft, Journal of Applied Physics, 29 (1958) 382–383.

[234] A. Rougier, P. Gravereau, and C. Delmas, Journal of The Electrochemical Society, 143 (1996) 1168–1175.

[235] E Zhecheva and R. Stoyanova, Solid State Ionics, 66 (1993) 143–149.

[236] I. Saadoune, M. Labrini, M. Yahya, A. Almaggoussi, H. Ehrenberg, Electrochimica Acta 55 (2010) 5180–5185.

[237] A. Mahmoud, M. Yoshita, I. Saadoune, J. Broetz, K. Fujimoto, S. Ito, Materials Research Bulletin 47 (2012) 1936–1941.

[238] Tze Qing Tan, Mohd Sobri Idris, Rozana Aina Maulat Osman, M.V. Reddy, B.V.R. Chowdari, Solid State Ionics 278 (2015) 43-48.

[239] Min Nie, Yun-Fei Xia, Zhen-Bo Wang, Fu-Da Yu, Yin Zhang, Jin Wu, Bing Wu, Ceramics International, 41 (2015) 15185-15192.

[240] Longwei Liang, Guorong Hu, Yanbing Cao, Ke Du, Zhongdong Peng, Journal of Alloys and Compounds, 635 (2015) 92-100.

[241] Huaquan Lu, Haitao Zhou, Ann Mari Svensson, Anita Fossdal, Edel Sheridan, Shigang Lu, Fride Vullum-Bruer, Solid State Ionics, 249 (2013) 105-111.

[242] P. Arora, R. White, and M. Doyle, Capacity fade mechanisms (1998)

[243] L. X. Yuan, Z. H. Wang, W. X. Zhang, X. L. Hu, J. T. Chen, Y. H. Huang and J. B. Goodenough, Energy Environ. Sci., 4 (2011) 269.

[244] Q. Liu, D. Mao, C. Chang and F. Huang, J. Power Sources, 173 (2007) 538-544.

[245] J. Molenda, M. Ziemnicki, J. Marzec, W. Zajac, M. Molenda and M. B. Ako, Journal of Power Sources, 173 (2007) 707-711.

[246] H. Shigemura, H. Sakaebe, H. Kageyama, H. Kobayashi, A. R. West, R. Kanno, S. Morimoto, S. Nasu and M. Tabuchi, Journal of the Electrochemical Society, 148 (2001) A730-A736.

[247] P. Arora, B. N. Popov and R. E. White, Journal of the Electrochemical Society, 145 (1998) 807-815.

[248] J. M. Amarilla, K. Petrov, F. PicÃ, G. Avdeev, J. M. Rojo and R. M. Rojas, J. Power Sources, 191(2009) 591-600.

[249] H. Huang, C. Wang, W. K. Zhang, Y. P. Gan and L. Kang, J. Power Sources, 184 (2008) 583-588.

[250] M. Aklalouch, R. M. Rojas, J. M. Rojo, I. Saadoune, J. M. Amarilla, Electrochimica Acta 54 (2009) 7542–7550

[251] S. Patoux, L. Sannier, H. Lignier, Y. Reynier, C. Bourbon, S. Jouanneau, F. Le Cras and S. Martinet, Electrochimica Acta, 53 (2008) 4137-4145.

[252] N. E. Sung, Y. K. Sun, S. K. Kim and M. S. Jang, Journal of the Electrochemical Society, 155 (2008) A845-A850.

[253] "Metal, Ceramic and Polymeric Composites for Various Uses", book edited by John Cuppoletti, Published: July 20, 2011.

[254] Jiajun Wanga and Xueliang Sun, Energy Environ. Sci. 5 (2012) 5163-5185.

[255] A. Yamada, S. C. Chung, K. Hinokuma, Journal of the Electrochemical Society, 148 (2001) A224.

[256] C. Delacourt, P. Poizot, S. Levasseur, C. Masquelier, Electrochemical and Solid State Letters, 9 (2006) A352-A355.

[257] G. Arnold, J. Garche, R. Hemmer, S. Strobele, C. Vogler, A. Wohlfahrt Mehrens, Journal of Power Sources, 119 (2003) 247-251.

[258] S. Franger, F. Le Cras, C. Bourbon, H. Rouault, J. Power Sources, 119 (2003) 252-257.

[259] N. Ravet, Y. Chouinard, J. F. Magnan, S. Besner, M. Gauthier, M. Armand, J Power Sources, 97 (2001) 503-507.

[260] S. L. Bewlay, K. Konstantinov, G. X. Wang, S. X. Dou, H. K. Liu, Materials Letters, 58 (2004) 1788-1791.

[261] H. Huang, S.-C. Yin, L. F. Nazar, Electrochemical and Solid-State Letters, 4 (2001) A170.

[262] A. Ait Salah, A. Mauger, K. Zaghib, J. B. Goodenough, N. Ravet, M. Gauthier, F. Gendron, C. M. Julien, Journal of the Electrochemical Society, 153 (2006) A1692-A1701.

[263] K. Dokko, S. Koizumi, K. Kanamura, Chemistry Letters, 35 (2006) 338-339.

[264] A.K. Padhi, K.S. Najundaswamy, J.B. Goodenough, J. Electrochem. Soc. 144 (1997) 1188.

[265] Li, G.; Azuma, H.; Tohda, M. J. Electrochem. Soc. 2002, 149 (6), A743–A747.

[266] Amine, A.; Yasuda, H.; Yamachi, Electrochem. Solid-State Lett. 3 (2000) 178.

[267] Yang, J.; Xu, J.J, J. Electrochem. Soc. 153 (2006) A716–A723.

[268] R. Marom, S. F. Amalraj, N. Leifer, D. Jacob and D. Aurbach, J. Mater. Chem., 21 (2011) 9938.

[269] N.-S. Choi, Z. Chen, S. A. Freunberger, X. Ji, Y.-K. Sun, K. Amine, G. Yushin, L. F. Nazar, J. Cho and P. G. Bruce, Angew. Chem, 51 (2012) 9994.

[270] G. Zhang and X. W. Lou, Angew. Chem, 53 (2014) 9041.

[271] J. B. Goodenough, Energy Environ. Sci, 7 (2014) 14.

[272] J. B. Goodenough, Acc. Chem. Res. 46 (2012) 1053.

[273] J. B. Goodenough and Y. Kim, Chem. Mater. 22 (2009) 587.

[274] A. Kraytsberg and Y. Ein-Eli, Adv. Energy Mater. 2 (2012) 922.

[275] M. V. Reddy, G. V. Subba Rao and B. V. R. Chowdari, Chem. Rev. 113 (2013) 5364.

[276] C. M. Julien and A. Mauger, Ionics 19 (2013) 951.

[277] J. Liu and X.-W. Liu, Adv. Mater. 24 (2012) 4097.

[278] Y. Zhao and L. L. Daemen, J. Am. Chem. Soc. 134 (2012) 15042.

[279] G. Zhang, H. B. Wu, H. E. Hoster and X. W. Lou, Energy Environ. Sci. 7 (2014) 302.

[280] http://www.targray.com/fr/li-ion-battery/cathode-materials/foils

[281] Shuwen Kang, Haiming Xie, Wei Zhai, Zi-feng Ma, Rongshun Wang and Weimin Zhang, Int. J. Electrochem. Sci., 10 (2015) 2324-2335.

[282] B. Son, M.-H. Ryou, J. Choi, T. Lee, H. K. Yu, J. H. Kim and Y. M. Lee, ACS Appl. Mater. Interfaces 6 (2013) 526.

[283] M.-H. Ryou, J. Kim, I. Lee, S. Kim, Y. K. Jeong, S. Hong, J. H. Ryu, T.-S. Kim, J.-K. Park, H. Lee and J. W. Choi, Adv. Mater. 25 (2013) 1571.

[284] L. Chen, X. Xie, J. Xie, K. Wang and J. Yang, J. Appl. Electrochem. 36 (2006) 1099.

[285] T. C. Hyams, J. Go and T. M. Devine, J. Electrochem. Soc. 154 (2007) C390.

[286] D. A. Shifler, P. J. Moran and J. Kruger, J. Electrochem. Soc. 141 (1994) 934.

[287] B. A. Shaw, G. D. Davis, T. L. Fritz, B. J. Rees and W. C. Moshier, J. Electrochem. Soc. 138 (1991) 3288.

[288] S.-T. Myung, K. Izumi, S. Komaba, Y.-K. Sun, H. Yashiro and N. Kumagai, Chem. Mater. 17 (2005) 3695.

[289] S.-T. Myung, K. Izumi, S. Komaba, H. Yashiro, H. J. Bang, Y.-K. Sun and N. Kumagai, J. Phys. Chem. C 111 (2007) 4061.

[290] L. J. Krause, W. Lamanna, J. Summerfield, M. Engle, G. Korba, R. Loch and R. Atanasoski, J. Power Sources 68 (1997) 320.

[291] S.-T. Myung, Y. Hitoshi and Y.-K. Sun, J. Mater. Chem. 21 (2011) 9891.

[292] http://supercondensateur.com/schema-batterie-li-ion-cobalt.

[293] P.A. Nelson, K.G. Gallagher, I. Bloom, and D.W. Dees, Modeling the Performance and Cost of Lithium-Ion Batteries for Electric-Drive Vehicles, SECOND EDITION, Argonne National Laboratory December (2012).

[294] J. Rodriguez-Carvajal, Laboratoire Léon Brillouin. llb.cea.fr, (2004).

[295] J. F. Berar and Lelann, J. App. Cryst., 24 (1991) 1.

[296] Mathilde Bourbin, Yann Le Du, Laurent Binet, Didier Gourier, Source Code for Biology and Medicine 8 (2013) 15.

[297] Brunauer Stephen, Emmett P. H., Teller Edward, Journal of the American Chemical Society 60 (1938) 309–319.

[298] Kuichen Wu, Fei Wang, Lulu Gao, Man-Rong Li, Lingli Xiao, Liutao Zhao, Sujuan Hu, Xiaojun Wang, Zhongling Xu, Qingguo Wu, Electrochimica Acta 75 (2012) 393–398.

[299] I. Saadoune, M. Dahbi, M. Wikberg, T. Gustafsson, P. Svedlindh, K. Edström, Solid State Ionics 178 (2008) 1668-1675.

[300] D. Caurant, N. Baffier, B. Garcia and J. P. Pereira-Ramos, Solid State Ionics, 91 (1996) 45-54.

[301] N. Tran, L. Croguennec, C. Labrugère, C. Jordy, P. Biensan and C. Delmas, J. Electrochem. Soc., 153 (2006) A261-A269.

[302] M. Dahbi, I. Saadoune, J-M. Amarilla, Electrochimica Acta 53 (2008) 5266–5271.

[303] I. Saadoune, M. Labrini, M. Yahya, A. Almaggoussi, H. Ehrenberg, Electrochimica Acta55 (2010) 5180–5185.

[304] Y. Bentaleb, I. Saadoune, K. Maher, L. Saadi, K. Fujimoto, S. Ito, Journal of PowerSources 195 (2010) 1510–1515.

[305] A. Abdel-Ghany, K. Zaghib, A. Mauger, M. Massot, F. Gendron, C.V. Ramana and C.M. Julien, ECS Transactions, 36 (2007) 129-136.

[306] K. Ben Kamel, N. Amdouni, A. Abdel-Ghany, K. Zaghib, A. Mauger, F. Gendron, C.M.Julien, Ionics 14 (2008) 89

[307] E. Shinova, R. Stoyanova , E. Zhecheva, G.F. Ortiz , P. Lavela , J.L.Tirado, Solid StateIonics 179 (2008) 2198–2208

[308] J. Liu, W. Qiu, L. Yu, H. Zhao, and T. Li, Journal of University of Science and Technology Beijing, 2 (2007) 173.

[309] Seo Hee Ju, Yun Chan Kang Ceramics International 35 (2009) 1205–1210

[310] T. Ohzuku, A. Ueda, M. Nagayama, J. Electrochem. Soc. 140 (1993) 1862.

[311] F. Zhou, X. Zhao, Z. Lu, J. Jiang, and J.R. Dahn, Electrochem. Communications, 10 (2008) 1168–1171.

[312] J. Wilcox, and M. Doeff, ECS Transactions, 11 (2008) 27–33.

[313] S.-K. Hu, T.-C. Chou, B.-J. Hwang, and G. Ceder, J. Power Sources, 160 (2006) 1287–1293.

[314] Dan Doughty, E. Peter Roth, The electrochemical society interface (2012) 37-44.

[314] E.P Roth, D.H Doughty, J. Power Sources 128 (2004) 308-318

[316] Diego Lisbona, Timothy Snee, Process Safety and Environmental Protection 89 (2011) 434-442.

[317] P.G. Balakrishnan, R. Ramesh, T. Prem Kumar, J. Power Sources 155 (2006) 401-414

[318] H. Sclar, D. Kovacheva, E. Zhecheva, R. Stoyanova, R. Lavi, G. Kimmel, J. Grinblat, O. Girshevitz, F. Amalraj, O. Haik, E. Zinugrad, B. Markovsky, D. Aurbach, J. Electrochem. Soc. 156 (2009) A939-A948.

[319] R. Stoyanova, A.-L. Barra, M. Yoncheva, E. Zhecheva, E. Shinova, P. Tzvetkova, S. Simova, Inorg. Chem. 49 (2010) 1032-1941.

[320] E. Zhecheva, R. Stoyanova, R. Alcantara, P. Lavela, J. Tirado, J. Power Sources 174 (2007) 519-523.

[321] A. Mauger, F. Gendron, C. Julien, J. Alloys Compd. 520 (2012) 42-51.

[322] M. Inaba, Y. Iriyama, Z. Ogumi, Y. Todzuka, and A. Tasaka, J. Raman Spectrosc.,28 (1997) 613.

[323] C. M. Julien, Mater. Sci. Eng. R-Rep., 40 (2003) 47.

[324] W. W. Huang and R. Frech, Solid State Ionics, 86–8 (1996) 395.

[325] L. El-Farh, M. Massot, M. Lemal, C. Julien, S. Chitra, P. Kalyani, T. Mohan, and R. Gangadharan, J. Electroceram., 3 (1999) 425.

[326] C. M. Julien and M. Massot, Mater. Sci. Eng., B, 100 (2003) 69.

[327] H. S. Park, S. J. Hwang, and J. H. Choy, J. Phys. Chem. B, 105 (2001) 4860.

[328] D.K. Gosser Jr., Cyclic Voltammetry, VCH Publishers, Inc., New York, 1994.

[329] D.Y.W. Yu, C. Fietzek, W. Weydanz, K. Donoue, T. Inoue, H. Kurokawa, S. Fujitani, J. Electrochem. Soc. 154 (2007) A253.

[330] K. Zhu, Q. Wang, J. H. Kim, A. A. Pesaran, A. J. Frank, J. Phys. Chem. C, 116 (2012) 11895.

[331] H. Liu , C. Li , H. P. Zhang, L. J. Fu, Y. P. Wu, H. Q. Wu, J. Power Sources, 159 (2006) 717.

[332] Dess E, Electrochim. Acta, 50 (2005) 2927.

[333] S. Yang, X. Wang, X. Yang, Y. Bai, Z. Liu, H. Shu, Q. Wie, Electrochim. Acta, 66 (2012) 88.

[334] J. Choi, and A. Manthiram, Solid State Ionics, 176 (2005) 2251.

[335] A. A. Bachin, Crystallography and crystal chemistry of materials with layered structures, Reidel Publishing Company, Dordrecht-Holland.

[336] « New Trends in Intercalation Compounds for Energy Storage » edited by C. Juilian, J.P. Pereira-Ramos and A. Momchilov, II Mathematics, Physics and Chemistry - vol. 61.

[337] C. Delmas, C. Fouassier and P. Hagenmuller, Physica, 99B (1980) 81.

[338] L. Croguennec, C. Pouillerie, A.N. Mansour and C. Delmas, J. Mater. Chem., 11 (2001) 131.

[339] M. Guilmard, L. Croguennec, D. Denux, C. Delmas, Chemistry of Materials, 15 (2003) 4476.